Università degli Studi di Torino
Scuola di Dottorato in Fisica
XXXIV ciclo

Performance of the 3D pixel tracker of the CMS Precision Proton Spectrometer and search for Anomalous Quartic Gauge Couplings in exclusive vector boson pair production with proton tagging

Andrea Bellora

Università degli Studi di Torino
Scuola di Dottorato in Fisica
XXXIV ciclo

Dottorato in Fisica

Performance of the 3D pixel tracker of the CMS Precision Proton Spectrometer and search for Anomalous Quartic Gauge Couplings in exclusive vector boson pair production with proton tagging

Andrea Bellora

Tutor: Ada Maria Solano
Co-tutor: Maria Margherita Obertino

Abstract

The Precision Proton Spectrometer (PPS) of the Compact Muon Solenoid (CMS) experiment at the Large Hadron Collider (LHC) is a near-beam magnetic spectrometer that measures protons surviving the collision in the CMS interaction point (IP). Because of the LHC magnetic fields, protons that lost part of their energy in the interaction are bent outside the beam envelope and can be detected. Located ~ 200 m away from the IP on both sides of CMS, the PPS stations provide a tracking and timing measurement of the outgoing protons, thus determining their kinematic properties.

This valuable information represents a unique extension of the physics capabilities of CMS, as it allows the entire final state of central exclusive production (CEP) events to be reconstructed. In fact, CEP consists in processes which produce a central state while the protons survive the interaction. The central state kinematics, reconstructed with the CMS detectors, can thus be matched with the ones inferred from the proton measurement and used to effectively identify CEP events.

The PPS has taken data during Run 2 (2016-2018), collecting more than 100 fb^{-1} of integrated luminosity. During operation the detector is subject to a high and non-uniform irradiation. To cope with this, the tracking detectors were equipped with 3D silicon pixel sensors, read out by the chips developed for the Phase I upgrade of the CMS central pixel tracker. Because of the non-uniform radiation damage in the readout chips, a thorough characterization of the tracking efficiency along the data-taking was carried out, followed by extensive studies of the PPS proton reconstruction performance.

The PPS will take data in Run 3 (2022-2025), with completely new detectors. The tracker will be equipped with a new type of 3D silicon pixel sensors and different readout. The detector has been characterised and integration tests have been performed in preparation of the data-taking. An innovative movement system has been designed and implemented, which will allow to spread the irradiation across the detectors, making it more uniform and effectively extending their lifetime. The detector has recently been installed and is currently under commissioning.

A search for anomalous quartic gauge couplings (AQGC) in exclusive vector boson pair production with proton tagging has been performed with Run 2 data. The decay channel in which both vector bosons decay into quarks, which are reconstructed as a single large-radius jet because of their Lorentz boost, has been studied. No excess with respect to the Standard Model predictions has been detected and limits on dimension-6 and dimension-8 AQGC effective field theory couplings have been set.

Contents

Introduction

This PhD thesis revolves around the Precision Proton Spectrometer (PPS) of the Compact Muon Solenoid (CMS) experiment at the CERN Large Hadron Collider (LHC). The subject of the thesis is the study of the Run 2 (2016-2018) PPS performance, the preparation of the new PPS tracker for Run 3 (2022-2025), and the search of Anomalous Quartic Gauge Couplings (AQGC) in the central exclusive production of vector boson pairs (WW/ZZ) with proton tagging in Run 2 data.

The PPS is a magnetic near-beam spectrometer that employs tracking and timing detectors to measure scattered protons that survive the interaction in the CMS collision point, losing a fraction of their energy. The protons typically escape the central detectors, proceeding inside the beam pipe, and are deviated by the LHC magnetic fields outside the beam envelope at $\sim$ 200 m, where the PPS detectors measure them on both sides of CMS. The PPS detectors are installed in mechanical structures called Roman Pots (RPs), which can be moved into the LHC beam pipe, approaching the beam as close as $\sim$ 1.3 mm.

The PPS detectors are exposed to a very challenging environment, where irradiation is particularly high, peaking at $\sim 10^{15}$ p/cm^2 in Run 2, and non-uniform. 3D silicon pixel sensors were selected for the PPS tracker, representing an optimal choice to cope with irradiation. However, the strong non-uniformity induced inefficiency in the readout chip, the radiation damage of which has been extensively studied and characterized.

The PPS provides a unique extension of the CMS physics capabilities, as it allows to observe the entire final state of a variety of processes called central exclusive production (CEP). In such events, the two protons

survive the interaction, while generating a central state which is measured by the CMS detectors.

PPS has successfully taken data during the LHC Run 2 and, at the time of writing this thesis, is almost ready for starting the Run 3 data-taking, which will last until 2025.

In the first period of my PhD, I studied the PPS performance during the Run 2 data-taking, starting from the efficiency of the tracking detectors and later focusing on the proton reconstruction efficiency. The tracker efficiency studies are the subject of a public CMS Detector Performance Summary [1]. The proton reconstruction studies contributed to a PPS publication, which is currently available as a Public Analysis Summary [2] and will be submitted for journal publication shortly, of which I am one of the editors.

In the following years, I worked on many aspects of the PPS tracker in preparation for Run 3. The new detector production was tested, and then I set up and performed at CERN the integration tests, necessary to ensure the detector functionality before installation.

Furthermore, I worked on the implementation of an innovative detector movement system. It consists of small-size motors that allow to move the tracking detectors within the RPs during down-time and thus spread the irradiation. This will limit the radiation damage and effectively extend the detector lifetime. In this context, I designed the control system necessary to operate the motors and its software, tested it and installed the required components in the LHC tunnel.

In view of Run 3, I developed a software framework for the execution of automated calibrations during the future data-taking. This will allow to automate detector calibrations and performance evaluation tasks, which took a great deal of person-power to perform on Run 2 data.

In parallel to my work on the PPS detector, I contributed to the CMS Run 2 data analysis searching for Anomalous Quartic Gauge Couplings (AQGC) in vector boson pair (WW/ZZ) exclusive production with proton tagging. This analysis exploits the PPS protons to probe physics beyond the Standard Model and represents an unprecedented measure-

ment with forward protons. The data analysis results are currently public as a Physics Analysis Summary [3] and will be submitted for journal publication soon.

The thesis is structured in the following schema:

- Chapter 1 discusses the PPS physics case, namely the study of Central Exclusive Production (CEP) processes. The analyses carried out on data collected in the CMS Run 2 using forward protons are summarized and the state-of-the-art concerning Anomalous Quartic Gauge Coupling constraints from WW and ZZ measurements is presented.

- Chapter 2 provides a general description of the CMS experiment and an introduction to the PPS sub-detector.

- Chapter 3 presents an in-depth description of the Run 2 PPS tracker and its performance during the entire data-taking period.

- Chapter 4 discusses the techniques used for reconstructing protons with the PPS detector and the proton reconstruction performance with the Run 2 data.

- Chapter 5 focuses on the Run 3 PPS tracker preparation. A detailed description of the differences with respect to its Run 2 counterpart is provided. The novel movement system design and implementation is presented. The testing procedures used to qualify the Run 3 detectors are illustrated, and the software framework developed for automated calibration executions during data-taking is described.

- Chapter 6 discusses the search of AQGC in central exclusive WW and ZZ production with proton tagging and presents the analysis results.

Chapter 1

Central exclusive production with forward protons

The collision of two protons typically results in the scattered protons dissociating after exchanging a quark or gluon. In a special category of events called Central Exclusive Production (CEP), however, protons remain intact after producing a central state X, escape central detectors, and travel along the beampipes together with unscattered protons.

These t-channel reactions of the type $pp \to p \oplus X \oplus p$, are characterized by large rapidity regions without primary particle production, the so-called rapidity gaps (denoted with the $\oplus$ symbol). In CMS data analyses, the rapidity gaps have been used to tag exclusive events by vetoing forward activity in calorimeters and requiring track gaps [4–7]. Moreover, pileup is detrimental for such selection techniques, as concurrent interactions can disrupt the rapidity gaps. In the end, quasi-exclusive contributions, in which either one or both protons dissociated in an undetected low mass system could never be completely ruled out.

Near-beam detectors placed along the beam lines represent a unique extension of the central detectors physics capabilities, as they allow to measure outgoing protons, thus fully reconstructing the CEP final state. Such detectors were used in multiple experiments over the past decades at ISR [8, 9], SPS [10], HERA [11, 12], TEVATRON [13, 14] and RHIC

[15]. The Precision Proton Spectrometer (PPS) of CMS [16] and the ATLAS Forward Proton detector [17] represent the new generation of near-beam detectors: they are capable of operating at high luminosity and have a center of mass energy reach significantly higher than previous experiments.

In CEP interactions, correlations between the mass (m_X) and rapidity (y_X) of the central system and the fractional momentum losses of the intact protons ($\xi = \Delta p/p$) arise, as a consequence of the four-momentum conservation:

$$m_X = \sqrt{s\xi_+\xi_-} \qquad y_X = \frac{1}{2}\log\left(\frac{\xi_+}{\xi_-}\right) \tag{1.1}$$

where the $+$ $(-)$ pedices denote the measurement performed on the positive (negative) side (arm) of the detector, defined by its coordinate system, and s is the squared center of mass energy of the pp collision.

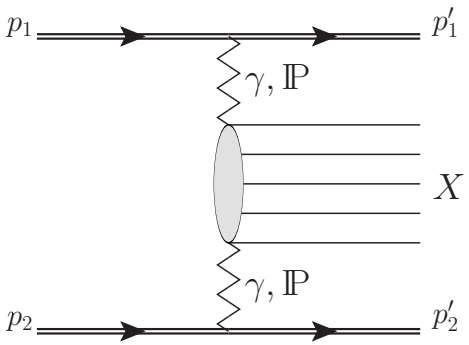

Figure 1.1: Schematic diagram for central exclusive production.

In order to preserve the proton integrity, the interaction with the central system must happen via a mediator that is neutral in flavour, charge and color. This is possible by exchanging either a photon (γ) or a pomeron ($\mathbb{P}$), that is a gluon pair in its leading order description (cf. Fig. 1.1). Exclusive events thus can be classified as QED-induced, when both protons emit a photon, or QCD-induced, when interaction happens only via pomerons.

As illustrated in Figure 1.2 for $X = b\bar{b}$ and $X = \gamma\gamma$, QCD-induced CEP dominates at low masses ($m_X \lesssim 100$ GeV), while high-mass states

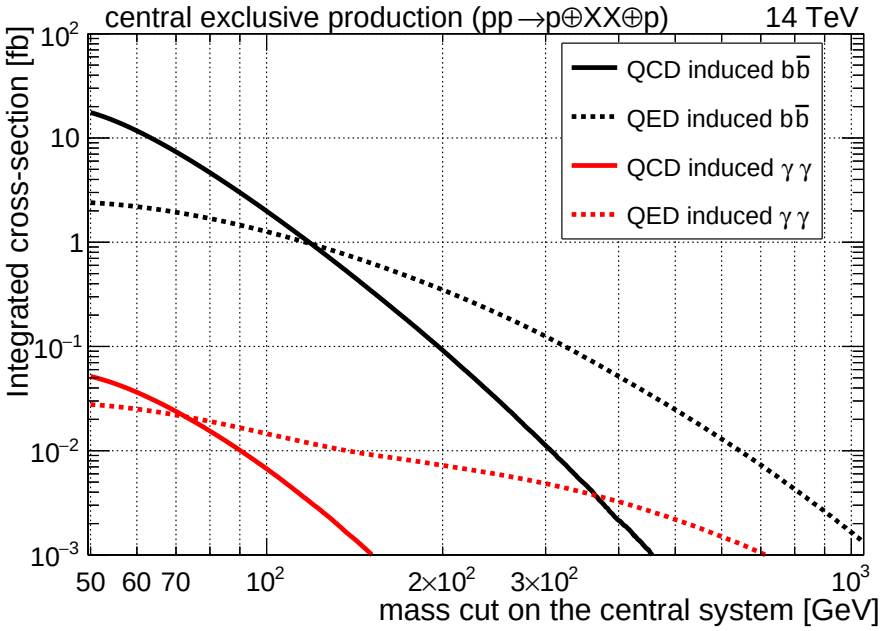

Figure 1.2: Integrated cross sections of different exclusive processes with intact protons at $\sqrt{s}$ =14 TeV, plotted as a function of the required minimum central system mass. Both photons or b-quarks are required to have a transverse momentum above 20 GeV [18].

are mainly generated via photons. In fact, in $\mathbb{P}\mathbb{P}$-initiated interactions (modelled by Khoze-Martin-Ryskin [19]), additional QCD radiation is more likely to fill up the rapidity gaps when higher-energy pomerons are emitted. Furthermore, soft rescattering processes of the interacting protons, which are responsible for the so-called rapidity gap survival probability, generate larger suppressions in QCD-induced CEP than in QED. The survival probability at $\sqrt{s} = 13$ TeV for $\mathbb{P}\mathbb{P}$-initiated CEP is in the order of few percent, while it is about 90% for $\gamma\gamma$-initiated CEP [18].

Processes initiated by a $\mathbb{P}$–γ are also possible in the SM and they are often referred to as *photoproduction*. In this case, the virtual photon emitted by one of the protons fluctuates into a $q\bar{q}$ pair that scatters off the other proton via $\mathbb{P}$ exchange. This results in the production of neutral vector mesons (ρ, ϕ, ω, J/ψ, $\psi(2S)$, Υ) and Z boson, with diagrams similar to Figure 1.3.

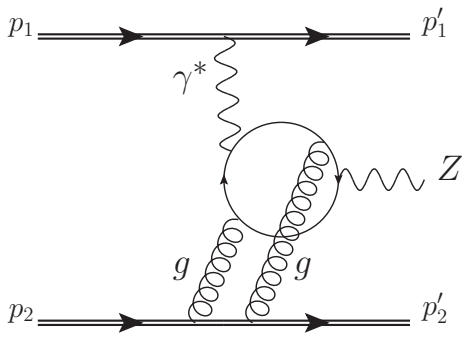

Figure 1.3: Diagram representing exclusive Z-boson photoproduction.

1.1 CMS data analyses with forward protons

The acceptance of the CMS PPS detector is defined by the LHC beam parameters (so-called beam optics), the positioning of detectors, and the setting of upstream beam elements (collimators). Details on the proton reconstruction and performance are provided in Chapter 4, however, approximate acceptance boundaries set proton ξ limits in the 0.02–0.15 range. For an LHC running scenario at $\sqrt{s} = 13$ TeV, as in Run 2, this is equivalent to a central system mass range from 260 GeV to 2.6 TeV. A complete description of the PPS apparatus is provided in Section 2.2.

This gives PPS the ability of testing Standard Model (SM) CEP processes with high central system masses. In addition, it can explore physics beyond the Standard Model (BSM) by searching enhancements in high mass tails. Furthermore, thanks to the full reconstruction of the final state with protons, PPS can scout for resonances in the missing mass spectrum.

Because of the low mass of the central system in photoproduction, this process is currently out of reach for PPS and might only be accessible with future upgrades (HL-LHC) [18].

In the following, a summary of the data analyses performed with forward protons reconstructed by PPS is presented.

1.1.1 Central semi(exclusive) production of high mass lepton pairs

The first analysis using PPS data targeted lepton pair production $pp \to p\ell^+\ell^- p^{(*)}$, with ℓ being an electron or muon [20], and either one or both proton remaining intact in the final state (Fig. 1.4).

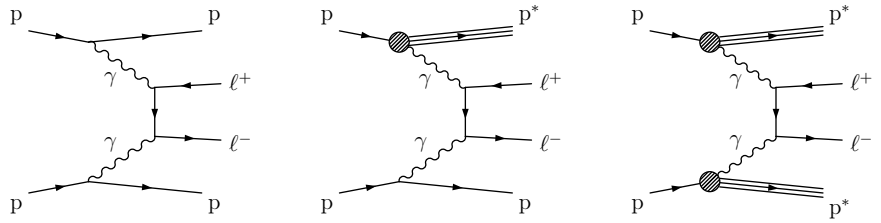

Figure 1.4: Production of lepton pairs by $\gamma\gamma$ fusion. The exclusive (left), single proton dissociation or semiexclusive (middle), and double proton dissociation (right) topologies are shown. The left and middle processes result in at least one intact final-state proton, and are considered signal in the analysis. The rightmost diagram is considered to be a background process [20].

The analysis focused on the first data collected in 2016, corresponding to an integrated luminosity of 9.4 fb^{-1}. It paved the way for successive PPS analyses, validating all aspects of reconstruction and calibration. In fact, lepton pair CEP is currently being used as an independent calibration handle for the PPS optics (Secton 4.1).

The event selection relied on vertex isolation and dilepton acoplanarity ($a = 1 - |\Delta\phi(\ell^+\ell^-)|/\pi$) to identify events with two different sign leptons emitted back-to-back in azimuth (ϕ). Furthermore, a dilepton mass requirement above 110 GeV was imposed.

Instead of using the relations presented in Equation 1.1 to match the centrally reconstructed mass and rapidity of the dilepton system with the one reconstructed with protons, the analysis exploited the following relation, which arises from the same four-momentum conservation constraint:

$$\xi_\pm(\ell^+\ell^-) = \frac{1}{\sqrt{s}}\left[p_T(\ell^+)e^{\pm\eta(\ell^+)} + p_T(\ell^-)e^{\pm\eta(\ell^-)}\right] \tag{1.2}$$

where the two solutions $\xi_\pm(\ell^+\ell^-)$ for $\pm\eta$ correspond to the protons moving

in the $\pm z$ direction. Even if this relation is exact only in CEP, it was shown to be valid also in the single-dissociation case.

Events were required to have $\xi_{\pm}(\ell^+\ell^-)$ within the PPS acceptance, and at least one proton detected by PPS. A matching requirement between the $\xi(p)$ measured with PPS and $\xi_{\pm}(\ell^+\ell^-)$ was imposed, with a tolerance equal to double the RMS of the $\xi(p) - \xi_{\pm}(\ell^+\ell^-)$ distribution.

Two background processes were considered: Drell-Yan and double-dissociation (events in which both protons disintegrate after the interaction, illustrated in the right diagram of Fig. 1.4). To satisfy the proton selection, background events need to be detected with simultaneous protons arising from pileup interactions or beam backgrounds.

The analysis identified 12 signal events in the $\mu^+\mu^-$ category, and 8 in the e^+e^-, illustrated in Figure 1.5. This represents a 5.1σ excess over the background-only hypothesis, when combining the two channels, consisting in the first observation of proton-tagged $\gamma\gamma$ collisions at the electroweak scale.

1.1.2 Central exclusive production of top quark-antiquark pairs

The CEP of top quark-antiquark pairs was recently studied in data collected in 2017, corresponding to an integrated luminosity of 29.4 fb^{-1} [21]. The predicted cross section in the SM at $\sqrt{s} = 13$ TeV is in the $\mathcal{O}(0.1$ fb) range, which makes the observation impossible with the currently available data and might only become accessible in HL-LHC. However, in case cross section enhancements would be detected, they would provide a strong indication of BSM physics.

The $t\bar{t}$ CEP was studied in two decay modes, namely the ℓ + jets, where $\ell = e$ or μ, and the dilepton mode. In the latter, both the W bosons originating from the t decay ($t \to b + W^+$) undergo a leptonic decay as in $W^+ \to \bar{\ell} + \nu_\ell$. In the former, one of the W bosons decays into a quark-antiquark pair.

Events were selected by requiring at least two jets to be identified as

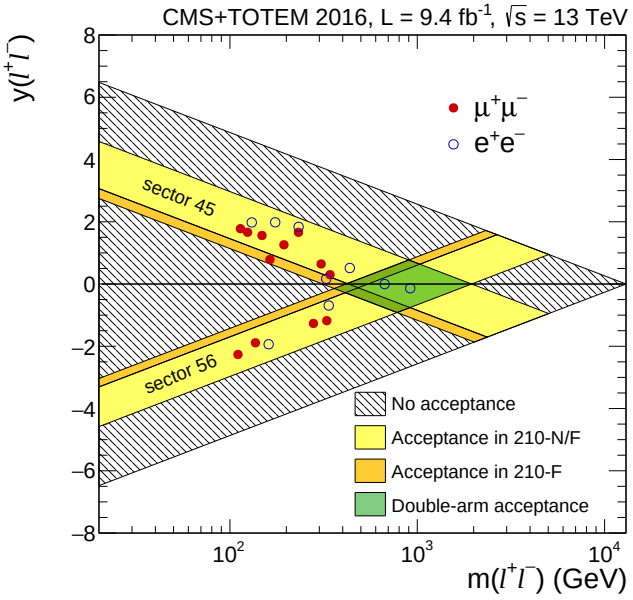

Figure 1.5: Expected acceptance regions in the rapidity vs. invariant mass plane overlaid with the observed dimuon (closed circles) and dielectron (open circles) signal candidate events. The "double-arm acceptance" refers to exclusive events, $pp \to p\ell^+\ell^- p$. Following the CMS convention, the positive (negative) rapidity region corresponds to the 45 (56) LHC sector [20].

originated by b quarks with the DeepCSV algorithm [22]. Events with two leptons of opposite charge, having mass at least 15 GeV distant from the Z boson mass peak, were assigned to the dilepton decay category. Instead, in the ℓ + jets category, the presence of exactly one lepton was required. Candidate events were also required to contain one forward proton in each PPS detector arm.

The strategy for the reconstruction of top quark-antiquark pair is different for the two categories. The dilepton one followed the algorithm used in [23], while the ℓ + jets used kinematic fitting techniques. That consists in fitting, event by event, the kinematic variables of the decay products, while letting them float within their uncertainty range and while imposing physical constraints. These constrains require the W boson and t quark masses to be equal to their known values, and four-momentum conservation in all decays to be satisfied. This method significantly im-

proves the $t\bar{t}$ mass reconstruction precision. In both decay channels, the final results are derived with a multivariate analysis approach (Boosted Decision Tree or BDT), shown in Figure 1.6.

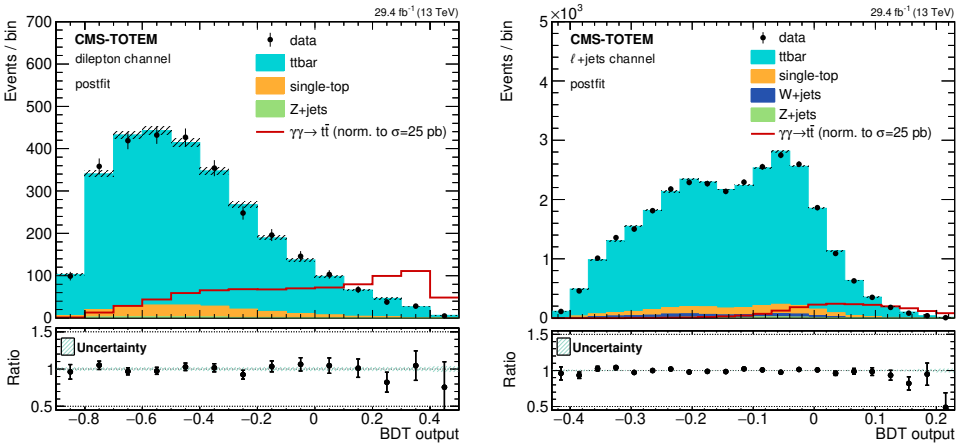

Figure 1.6: Distribution of the BDT score in the signal region for simulated events after the fit, and for data. Left: dilepton mode; right: ℓ + jets mode. The red open histogram shows the expected distribution for signal, normalized to a cross section of 25 pb, approximately 10^5 larger than the SM cross section prediction. For both reconstruction modes, all signal regions are combined. The lower panels show the data-to-prediction ratios; the hatched bands represent the relative uncertainty on the predictions.

Background contributions to the signal region were considered for inclusive $t\bar{t}$ production, single-top (tW) production, V + jets, VV (with V being a W or Z boson), and Drell-Yan. In all cases, to pass the selection described above, background events need to occur in coincidence with protons originated in pileup interactions.

As no excess over the background-only hypothesis is detected, upper limits on the cross section for the two decay modes are set (Fig. 1.7). The observed (expected) limit resulting from the combined fit of the two decay modes is 0.59 pb (1.15 pb). This represents the first result on $t\bar{t}$ CEP with intact protons. Being ~ 3 orders of magnitude larger than the SM prediction, the observed limit leaves room for cross section enhancements caused by BSM physics, which could be further constrained in future studies.

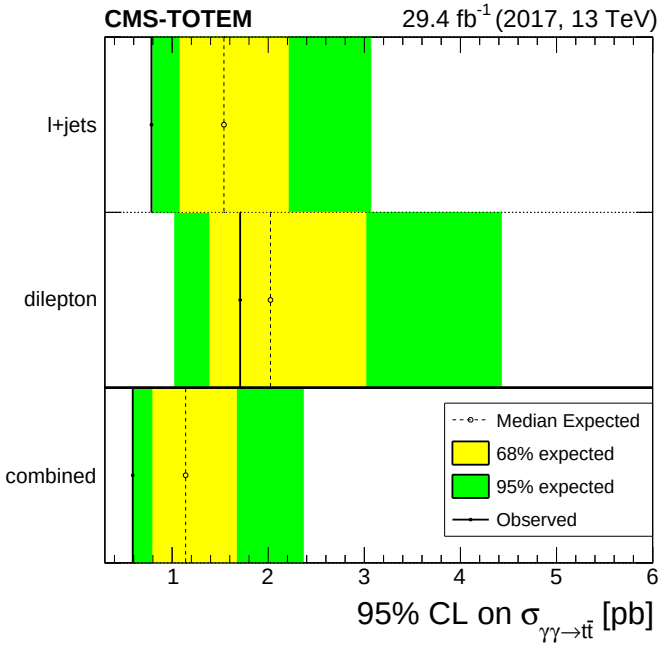

Figure 1.7: Expected 95% CL upper limit for the signal cross section, for the two reconstruction modes and for the combination. The green and yellow bands show the $\pm 1\sigma$ and $\pm 2\sigma$ intervals, respectively.

1.1.3 Central exclusive diphoton production at high mass

The PPS data collected in 2016 (9.4 fb^{-1} integrated luminosity) were used to search for light-by-light (LbyL) scattering [24], recently observed by ATLAS and CMS in heavy ions collisions [25–27]. In fact, being CEP processes mainly initiated by $\gamma\gamma$ interactions, exclusive diphoton production could represent a clean channel to study LbyL interactions in a higher mass range with respect to the one so far explored, of few GeV.

Photons, despite lacking self-interaction in the SM, can scatter off each other because of particle-antiparticle vacuum fluctuations. However many BSM models [28–35] predict enhancements of the LbyL cross sections at high mass. Some of them can be described by effective operators that

extend the SM Lagrangian as follows:

$$L_8^{\gamma\gamma\gamma\gamma} = \zeta_1 F_{\mu\nu} F^{\mu\nu} F_{\rho\sigma} F^{\rho\sigma} + \zeta_2 F_{\mu\nu} F^{\mu\rho} F_{\rho\sigma} F^{\sigma\nu}. \tag{1.3}$$

where F is the electromagnetic field tensor, and $\zeta_{1,2}$ are coupling parameters.

The analysis was carried out by selecting diphoton events with mass within the PPS acceptance and low acoplanarity, as if originating from a back-to-back emission. Photons are required to be isolated and the ξ of the outgoing protons is estimated with the same approach of the (semi)exclusive dilepton production analysis (Section 1.1.1). The diphoton system was further required to be in either a 2σ or 3σ matching window in mass and rapidity around those of the system reconstructed with outgoing protons.

Multiple background contributions were taken into account, with the leading contribution coming from inclusive $\gamma\gamma$ + jets production. Subleading components are produced by $V + \gamma$, where V is either a W or Z boson, and leptons from their decay are misidentified as photons.

No diphoton candidates were found in both matching windows, for a background expectation of 0.23 and 0.43 events, respectively. An upper limit of 4.4 fb is thus set on the LbyL SM cross section within the selection region.

Being the selection efficiency roughly double for anomalous production via Anomalous Quartic Gauge Coupling shown in Equation 1.3, a tighter upper limit is set on the process cross section, at 2.08 fb. This corresponds to the exclusion region, in the model parameter space, shown in Figure 1.8.

1.1.4 Search for missing mass resonances in association with Z or γ production

Recently, data collected in 2017 have been used for searching BSM physics signatures with the missing mass technique [36]. The analysis strategy

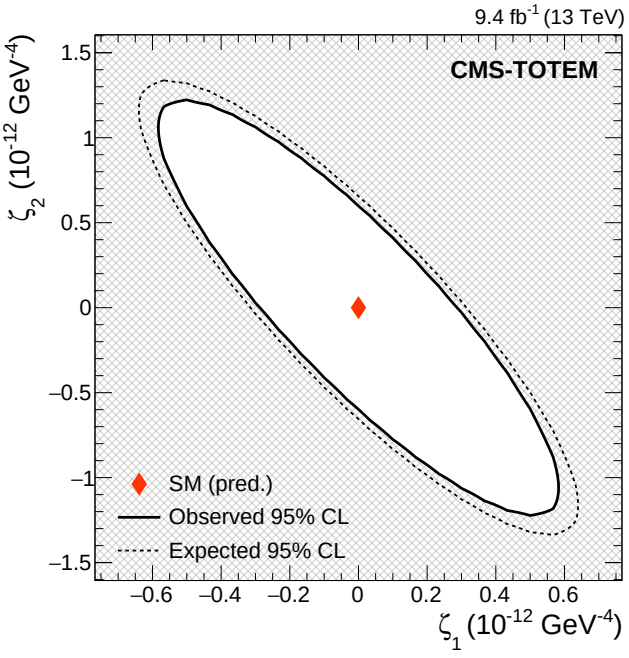

Figure 1.8: Two-dimensional limits on the anomalous four-photon couplings, derived from the observed upper limit on the diphoton production cross section. The shaded area depicts the excluded values of the coupling parameters ζ_1 and ζ_2.

consisted in looking for the production of an unknown particle (χ), in association with a Z boson or a photon (Fig. 1.9). Such unknown particle, assuming a sufficiently narrow decay width, could appear as a resonance in the missing mass (m_{miss}) spectrum, with m_{miss} defined as:

$$m^2_{\text{miss}} = \left[(P^{\text{in}}_{p_1} + P^{\text{in}}_{p_2}) - (P_V + P^{\text{out}}_{p_1} + P^{\text{out}}_{p_2})\right]^2 \tag{1.4}$$

where P_V is the four-momentum of the boson and $P^{\text{out,in}}_{p_i}$ (i=1,2) are the four-momenta of the outgoing and incoming protons, respectively. The transverse momenta of the protons can be neglected, while $p^{\text{out}}_{p_i}$ is computed from the ξ measured by PPS.

The analysis relies on the selection of either two same-flavor opposite-sign leptons (originating from the Z boson decay), or a photon detected in the central CMS detector. In addition, at least one proton is required

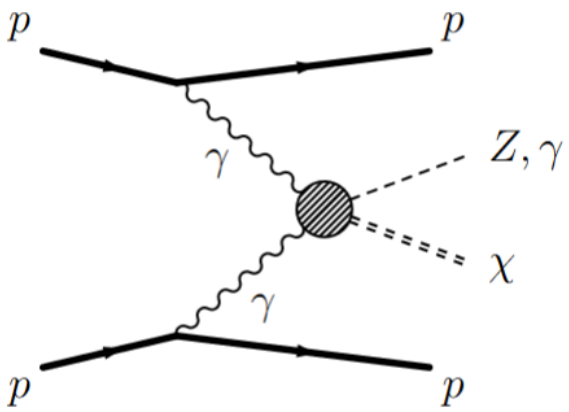

Figure 1.9: Schematic diagram of two-photon production of a Z boson or photon with an additional, unknown particle χ giving rise to a missing mass $m_{\text{miss}} = m_{\chi}$. The production mechanism does not have to proceed through photon exchange. Other colourless exchange mechanisms (e.g. double pomeron) are also allowed. However, at such a high energy scale, electroweak processes become dominant as QCD-based colourless exchanges are expected to be suppressed.

in each PPS detector arm. The signal selection sensitivity as a function of the χ particle mass was studied using a dedicated simplified Monte Carlo generator.

Background components from Drell-Yan or γ+jets, in coincidence with protons coming from pileup interactions, were found dominant, for the $Z+\chi$ and $\gamma+\chi$ categories, respectively. Minor contributions from top-quark production and multiboson processes (WW, WZ, and ZZ) were also considered. Further contributions from single-diffractive processes, with an additional proton from pileup, and SM exclusive production processes were also studied and found negligible.

The data samples analysed correspond to 37.2 (2.3) fb^{-1} integrated luminosity for the Z boson (photon) channel. Results were studied separately for the decay of the Z boson in two muons or two electrons, and finally combined.

No significant excess over the background-only expectation was detected, thus a 95% CL upper limit on the anomalous CEP of $pp \to ppZ/\gamma\chi$

as a function of the m_χ is set (Fig. 1.10).

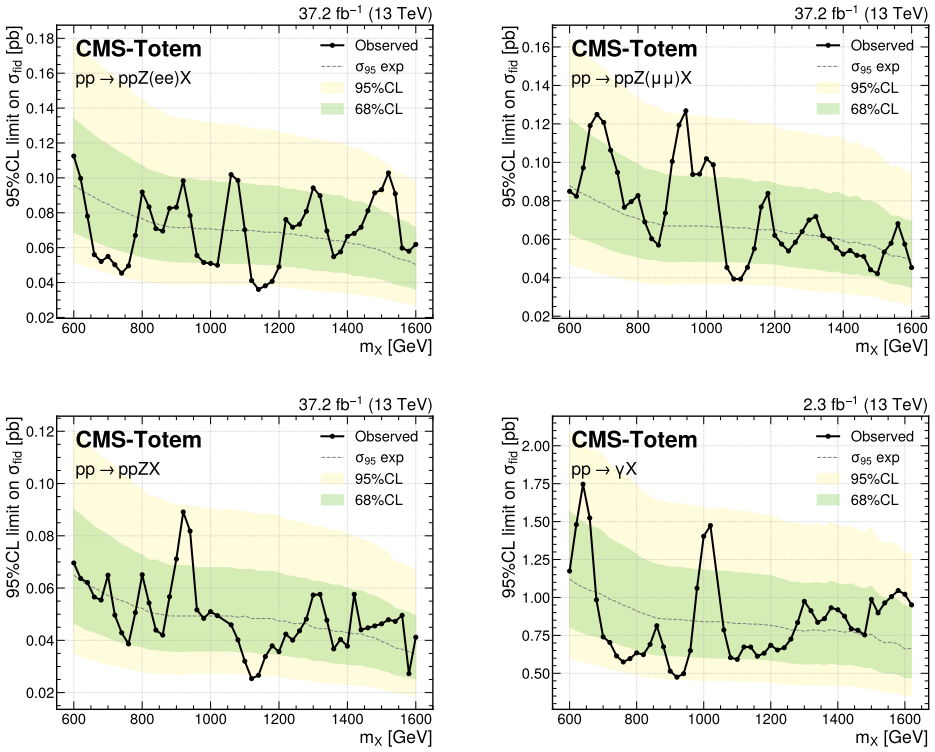

Figure 1.10: Upper limits on the $pp \to ppZ/\gamma\chi$ production cross section at the 95% CL, as function of m_χ. The 95% and 68% CL quantiles of the expected limits are represented by the bands, while the observed limit is superimposed as a curve. The top plots correspond to the $Z \to ee$ and $Z \to \mu\mu$ final states,while the bottom plots correspond to the combined Z and γ analyses.

1.2 Exclusive WW/ZZ production via $\gamma\gamma$ interaction

Vector boson pair exclusive production via $\gamma\gamma$ is allowed at tree level in the SM. This can happen both via triple gauge coupling γWW in t- and u-channel processes and quartic gauge coupling $\gamma\gamma WW$ (Fig. 1.11). The exclusive production cross section of W boson pairs with both protons remaining intact is expected to be ~ 87 fb at $\sqrt{s} = 13$ TeV [37].

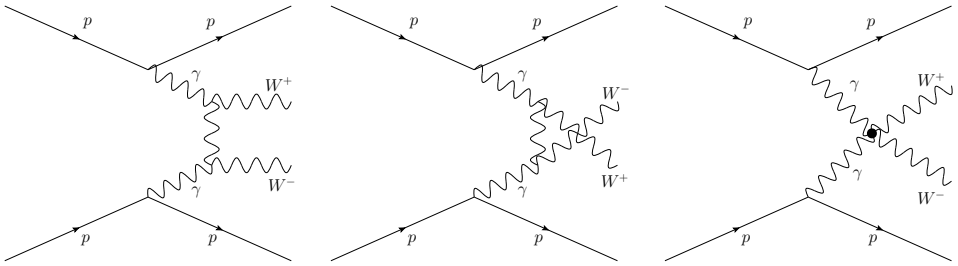

Figure 1.11: Schematic diagrams of $\gamma\gamma \to WW$ production with intact protons according to the Standard Model.

This process, without measuring outgoing protons, has been studied both at the ATLAS and CMS experiments at $\sqrt{s} = 7$ and 8 TeV, reaching 3.0σ and 3.4σ significance, respectively [38, 39]. Moreover, a recent analysis performed by ATLAS on the entire LHC Run 2 dataset ($\sqrt{s} = 13$ TeV) reached observation-level significance, measuring a $\gamma\gamma \to WW$ cross section of 3.13 fb in a fiducial volume close to the detector acceptance [40].

These measurements not only represent a test of the SM predictions, but also provide a powerful handle to constrain BSM theories. In exclusive events, the WW invariant mass (m_{WW}) spectrum is peaked at low values, while new physics at high scale could result in an enhancement of the high mass tail of the distribution. Searching for is thus interesting for probing BSM physics. This is also true for the $\gamma\gamma \to ZZ$ process, which is forbidden at tree level in the SM, and any evidence of it would provide a strong indication of new physics.

1.2.1 Effective Field Theory framework

It is common practice in multiboson BSM physics searches to use the Effective Field Theory (EFT) approach as a theory-agnostic way to model new physics processes. This consists in expanding the SM Lagrangian $\mathcal{L}_{\text{SM}}$ with additional operators $\mathcal{O}_i$ of dimension $\Delta_i \geq 4$ as in:

$$\mathcal{L}_{\text{EFT}} = \mathcal{L}_{\text{SM}} + \sum_i \frac{g_i \mathcal{O}_i}{\Lambda^{\Delta_i - 4}}, \tag{1.5}$$

where the g_i terms are called Wilson coefficients and Λ is the scale of new physics, which must be higher than the energy scale being probed in the experiment for the EFT expansion to be valid.

At energies beyond Λ, scattering amplitudes generated by EFT operators rapidly increase, eventually causing an unphysical unitarity violation. This is a theoretically well-understood feature of EFT and multiple techniques are employed to deal with these divergences (e.g. ad-hoc form factors, clipping or K-matrix unitarization). Further discussion on unitarity preservation in presence of EFT signal, in the context of the search of AQGC in exclusive vector boson pair production is postponed to Section 6.6.1.

An exhaustive summary of the theoretical conventions used to model anomalous triple and quartic gauge couplings (ATGC and AQGC, respectively) is provided in the review at Ref. [41]. However, for the sake of this thesis, only the operator bases used in the search of AQGC presented in Chapter 6 are covered.

The effective operators employed to parameterise the quartic couplings are, following Ref. [42, 43]:

$$\mathcal{L}_{\mathrm{EFT}} = \mathcal{L}_{\mathrm{SM}} + \mathcal{L}^0 + \mathcal{L}^{\mathrm{C}} \tag{1.6}$$

$$\mathcal{L}^0 = \frac{-e^2}{8}\frac{a_0^W}{\Lambda^2} F_{\mu\nu}F^{\mu\nu}W^{+\alpha}W^-_\alpha - \frac{-e^2}{16cos^2\theta_W}\frac{a_0^Z}{\Lambda^2} F_{\mu\nu}F^{\mu\nu}Z^\alpha Z_\alpha \tag{1.7}$$

$$\mathcal{L}^{\mathrm{C}} = \frac{-e^2}{16}\frac{a_C^W}{\Lambda^2} F_{\mu\alpha}F^{\mu\beta}\left(W^{+\alpha}W^-_\beta + W^{-\alpha}W^+_\beta\right) - \frac{-e^2}{16cos^2\theta_W}\frac{a_C^Z}{\Lambda^2} F_{\mu\alpha}F^{\mu\beta}Z^\alpha Z_\beta \tag{1.8}$$

where e is the electron charge, θ_W is the weak mixing angle, and F, W and Z represent the field strength of electromagnetic and weak interactions. The $a_{0,C}^{W,Z}$ coefficients terms are the coupling constants. From the Lagrangian it is clearly visible that scattering amplitude, and thus cross sections, depend quadratically on the $a_{0,C}^{W,Z}/\Lambda^2$ values.

Despite not being the most modern parameterisation, it was chosen for the analysis reported in Chapter 6 as it is the available option im-

plemented in the Forward Physics Monte Carlo (FPMC) [37], which is a common event generator choice for physics studies with forward protons.

Under some assumptions, discussed in further detail in Section 6.6.2, the operators written above can be translated in a linear combination of dimension-8 $f_{M,i}$ ($i = 0...7$) operator coupling coefficients, listed in Ref. [41]. These dimension-8 operators are a subset of the 18-operator basis that can modify multiple vector boson production via AQGC. This basis has found wide usage in searches performed at the CMS and ATLAS experiments [38, 39, 44–48].

The interpretation of analysis results in terms of EFT operator sensitivity provides useful information that can be exploited in further theory studies to constrain multiple models, including composite Higgs [49, 50], warped [50] and large [31] extra dimensions, and CP violating gauge-Higgs couplings [51].

1.2.2 Previous results on anomalous gauge couplings

To this date, the most stringent limits on ATGC have been obtained by CMS in $q\bar{q} \to WW$ and $q\bar{q} \to WZ$ with one W boson decaying into leptons, and the other boson decaying hadronically [52]. These are s-channel processes in which, at leading order, the electroweak boson self-couplings enter via $WW\gamma$ and WWZ vertices for WW production, and WWZ only for WZ production 1.12. Anomalous couplings appear as enhancements of the production foreseen by the SM.

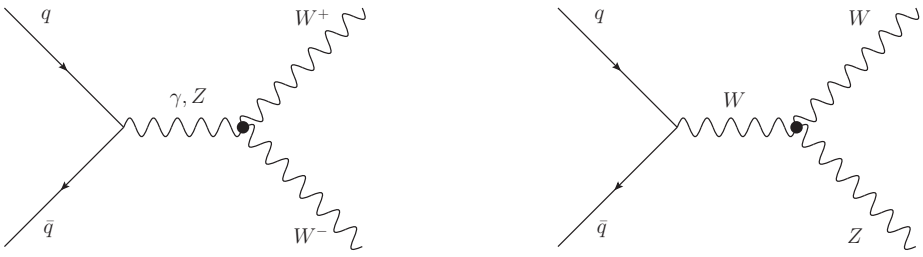

Figure 1.12: Schematic diagrams of $q\bar{q} \to WW$ production via triple gauge coupling.

Also the $\gamma\gamma \to WW$ exclusive process contains two triple gauge coupling vertices (Fig. 1.11). However, it has been shown that its sensitivity to ATGC does not surpass limits imposed by previous measurements at LEP [42], thus neither the more stringent ones cited above.

The exclusive vector boson pair production has proven nevertheless to be a particularly sensitive channel to study AQGC. Early limits on the $a^W_{0,C}/\Lambda^2$ were set by CMS and ATLAS analyses at 7 and 8 TeV center of mass energy collected during LHC Run 1 (2009-2013) [38, 39], improving previous results from the OPAL [53] and D0 experiments [54].

These analyses focused on events in which the boson pair decays into different flavor leptons and neutrinos, detected as missing energy. Looking for event candidates with large rapidity gaps between the leptons and no additional activity associated with their primary vertex, the analyses defined a signal region for SM candidates and looked for AQGC signatures in the large $p_T(e\mu)$ tails. Non-exclusive WW production represented the dominant background and significant uncertainties on the proton dissociation factor affected the SM predictions.

In addition, the limits relied on high-p_{T} events, making the measurement more sensitive to high-mass events than low mass ones. This is reflected in the approximately two order of magnitude difference in the limits obtained with and without unitarization (suppression of the cross section at high mass). The limits obtained by applying a form factor with a cutoff scale at 500 GeV were in the $a^W_{0,C}/\Lambda^2 < \mathcal{O}(10^{-4})$ GeV.

The forward proton tagging capabilities provided by the PPS detector allow to suppress contributions generated by proton dissociation. In addition, anticipating the discussion presented in Section 6.6, the PPS acceptance boundaries at high mass act as a built-in unitarity constraint, granting smaller differences between unitarized and non-unitarized results. These features make the search for AQGC in WW and ZZ exclusive production with proton tagging particularly promising. This analysis has been pursued and a report is given in Chapter 6.

Finally, it must be mentioned that limits on AQGC have also been obtained with channels other than the vector boson pair exclusive pro-

duction. A number of scattering [44–47] and triple boson production [48] processes at 13 TeV have been exploited to provide some of the most stringent limits set to this date.

Chapter 2

The CMS detector and PPS

2.1 The CMS detector

The Compact Muon Solenoid (CMS) is a general-purpose particle detector operating at the Large Hadron Collider (LHC) at CERN. It was designed to study proton-proton collisions with center of mass energies up to 14 TeV at luminosities up to 10^{34} $\mathrm{cm}^{-2}\mathrm{s}^{-1}$.

During LHC Run 1 (2010-2012), pp collisions were produced at center of mass energies up to 8 TeV with 50 ns bunch spacing, and about 25 fb^{-1} of integrated luminosity were collected by CMS and used for physics measurements [55].

In LHC Run 2 (2015-2018) the center of mass energy reached 13 TeV, with 25 ns bunch spacing, and about 137 fb^{-1} of data were collected [56].

The central feature of the CMS apparatus is a superconducting solenoid of 6 m internal diameter, providing a magnetic field of 3.8 T. Within the solenoid volume are a silicon pixel and strip tracker, a lead tungstate crystal electromagnetic calorimeter (ECAL), and part of the brass and scintillator hadron calorimeter (HCAL), each composed of a barrel and two endcap sections. Forward calorimeters extend the pseudorapidity coverage provided by the barrel and endcap detectors. Muons are measured in gas-ionization detectors embedded in the steel flux-return yoke outside the solenoid [57]. Outgoing protons are measured by a forward

proton spectrometer, the so-called Precision Proton Spectrometer (PPS), described in Section 2.2.

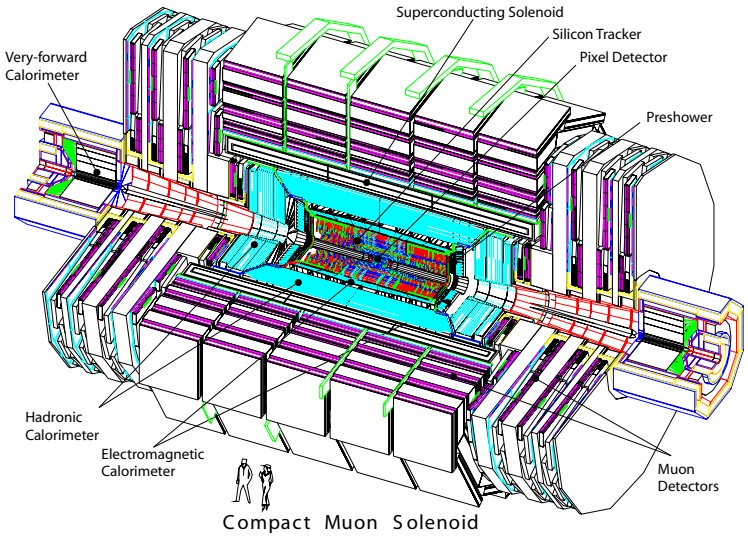

Figure 2.1: Schematic view of the CMS detector.

2.1.1 Coordinate system

The CMS coordinate system is chosen with the y-axis pointing vertically towards the surface and the z-axis that points in the direction of the LHC beam 2 (west). It follows naturally that the x-axis points towards the center of the LHC ring. The azimuthal angle ϕ is measured from the x-axis in the xy plane and the polar angle θ is defined in the rz plane, where r is the radial coordinate on the xy plane. The pseudorapidity is $\eta = -\ln\tan(\theta/2)$, and p_T is the momentum component transverse to the z-axis, computed from the x- and y-components of the momentum.

2.1.2 Magnet

The CMS magnet is a 13-m-long, 6-m-inner diameter superconducting solenoid capable of generating a 3.8 T magnetic field. The 220-t coil is made of 4-layer stabilised reinforced NbTi windings and is large enough

to house the tracker and the barrel calorimeters. The flux is returned through a 10 000-t steel yoke within which four muon chamber stations are integrated.

2.1.3 Tracker

The CMS inner tracking system is designed to provide 3-dimensional space points in the region closest to the interaction point that allow to efficiently and precisely track charged particles and perform vertex reconstruction. The tracker entirely relies on silicon detector technology, with the inner layers using pixel sensors and the outer ones silicon strips.

The original design of the barrel portion consisted in three layers of pixels located at radii between 4.4 cm and 10.2 cm, followed by 10 layers of strips, extending outwards to a radius of 1.1 m. The barrel was complemented by two endcaps composed of 2 (3 plus 9) pixels (strips) disks on each side, granting acceptance up to a pseudorapidity of $|\eta| < 2.5$, with a total length of 5.8 m. The whole tracker consisted of 1 440 silicon pixel and 15 148 silicon strip detector modules [58].

During the first LHC long shutdown (LS1, 2013-2014), the original pixel tracking system was upgraded (Fig. 2.2b). Profiting from the new smaller-radius beam pipe, one additional layer of pixel detectors was installed in the barrel section, while the others were slightly relocated. Upgrades were also performed on the endcaps, changing their layout and adding a new layer. The total number of silicon pixel sensors increased to 1 856, with ≈ 1.9 m^2 of active area (≈ 200 m^2 when including also the silicon strip sensors) [59].

For non-isolated particles of $1 < p_T < 10$ GeV and $|\eta| < 3.0$, the track resolutions are typically 1.5% in p_T and 20–75 μm in the transverse impact parameter. Isolated particles of $p_T = 100$ GeV emitted at $|\eta| < 1.4$ have track resolutions of 2.8% in p_T and 10(30) μm in the transverse(longitudinal) impact parameter.

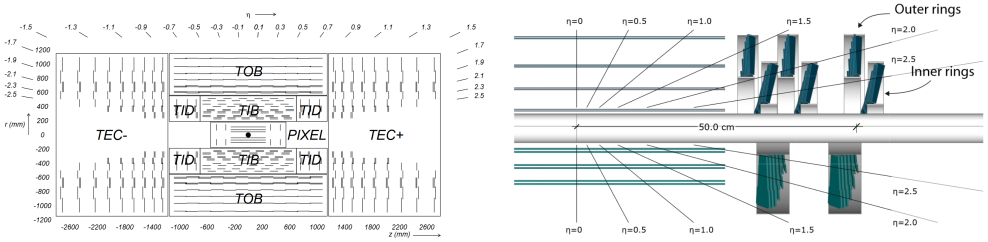

(a) **(b)**

Figure 2.2: (a): Cross section of the CMS tracker. (b): Difference between the Run 2 and 3 (top), and Run 1 (bottom) layouts of the tracker.

2.1.4 Electromagnetic calorimeter

The electromagnetic calorimeter of CMS (ECAL) is a hermetic homogeneous calorimeter made of 61 200 lead tungstate ($PbWO_4$) crystals mounted in the central barrel part, closed by 7 324 crystals in each of the two endcaps. A Preshower detector is placed in front of the endcap crystals. Avalanche photodiodes (APDs) are used as photodetectors in the barrel and vacuum phototriodes (VPTs) in the endcaps. Using high-density crystals allowed to build a fine granularity calorimeter. [60].

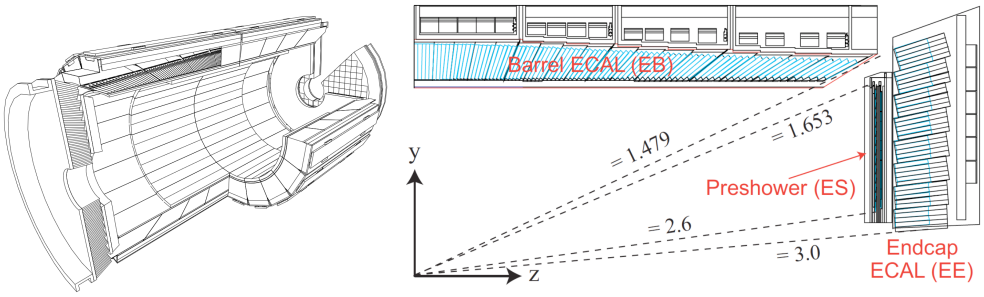

(a) **(b)**

Figure 2.3: (a): Schematic view of the CMS electromagnetic calorimeter. (b): Cross section of a quarter of ECAL, illustrating the crystals arrangement, and the preshower detector.

Figure 2.3 provides a schematic overview of the calorimeter.

The barrel portion of ECAL (EB) covers the pseudorapidity range $|\eta| < 1.479$. The granularity is 360-fold in ϕ and (2×85)-fold in η, with tapered crystal installed in a quasi-projective geometry to avoid

cracks aligned with the trajectory of particles coming from the nominal interaction point, both in the ϕ and η projections. The centre of the crystals front face is located at 1.29 m radius, with a cross section of 22×22 mm^2. Each of them is 230 mm long (25.8 X_0), and the rear face cross section is 26×26 mm^2. The crystals are contained in a thin-walled alveolar structure made of an aluminium layer facing the crystal, and two layers of glass fibre-epoxy resin.

The ECAL endcaps (EE) cover the rapidity range $1.479 < |\eta| < 3.0$ and are located at a longitudinal distance of 315.4 cm from the nominal interaction point (taking into account the 1.6 cm estimated shift towards it when the magnet is switched on). Each EE is divided in two halves (*Dees*), in which crystals are arranged in a rectangular x–y grid. They are grouped into 5×5 mechanical units, held together by a carbon-fibre alveolar structure. The crystals point towards a focal point that is 1 3 m beyond the interaction point. The crystals used in the EE are 220 mm long (24.7 X_0), with a front-face cross section of 28.62×28.62 mm^2, and a rear cross section of 30×30 mm^2.

The Preshower detector is placed in front of the endcaps, covering a pseudorapidity range of $1.653 < |\eta| < 2.6$. The main purpose of the Preshower is distinguishing between single photons and photons produced in pairs in $\pi \to \gamma\gamma$ decays and identifying electrons against minimum ionizing particles. It is a sampling calorimeter with two layers: lead radiators initiate electromagnetic showers from incoming photons/electrons, whilst silicon strip sensors measure the deposited energy and the transverse shower profiles after each radiator. The total thickness of the Preshower is 20 cm.

2.1.5 Hadronic calorimeter

Hadrons typically go through the ECAL without being stopped. The energy measurement of ECAL is thus complemented by the hadronic calorimeter (HCAL), which is a vital element in assuring the CMS hermeticity for hadronic final states and allows for precise missing energy

determination.

HCAL is a sampling calorimeter that uses alternating layers of brass absorber and fluorescent scintillator materials. The calorimeter is subdivided into four parts: hadron barrel (HB), endcap (HE), outer (HO) and forward (HF) calorimeters [61].

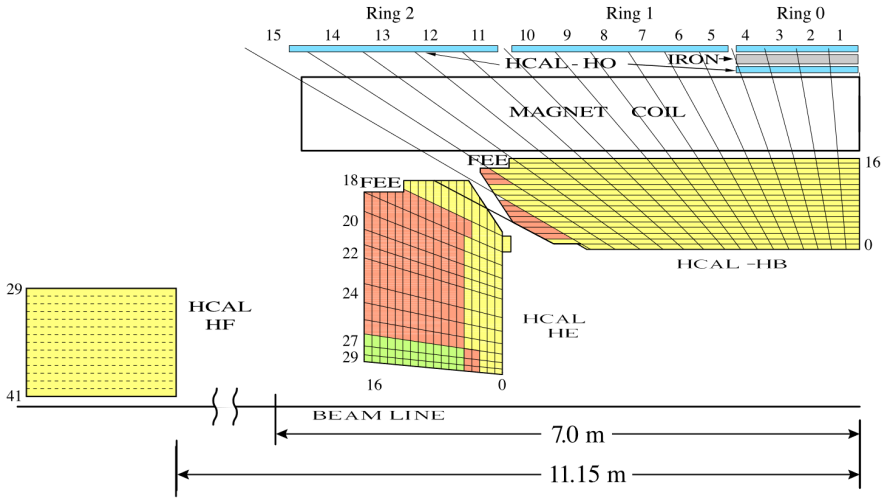

Figure 2.4: Cross section of the CMS hadronic calorimeter, showing the locations of the HB, HE, HO and HF.

The HCAL layout is illustrated in Figure 2.4. The HB is located within the superconducting solenoid, around the ECAL barrel. Since the combined stopping power of EB and HB is not sufficient to fully absorb hadronic showers in the low pseudorapidity range, further scintillators (HO) are placed outside the magnet that acts as a $1.4/sin(\theta)$ interaction lengths-long absorber. HO thus identifies late-starting showers and measures the energy deposited after HB. Together, HB and HO cover the pseudorapidity range $|\eta| < 1.3$.

The HE extend the rapidity coverage in the range $1.3 < |\eta| < 3$ (13.2% of the solid angle), region that contains $\approx 34\%$ of the particles produced in the final state.

Above $|\eta| = 3$, the HF, placed longitudinally at 11.2 m from the interaction point, further increase the reach up to $|\eta| = 5.2$, using radiation-hard, Cherenkov-based technology.

2.1.6 Muon system

The importance of the CMS muon system is paramount, as the acronym suggests. Muons typically escape the ECAL and HCAL, therefore they are measured by outer gas detectors interspersed in the magnetic field return yoke. The muon system identifies and measures the momentum of the muons. Furthermore, together with ECAL and HCAL, it contributes to the first level of the trigger system [62].

The muon system is sub-divided into a cylindrical barrel section and two planar endcap regions, as shown in Fig. 2.5.

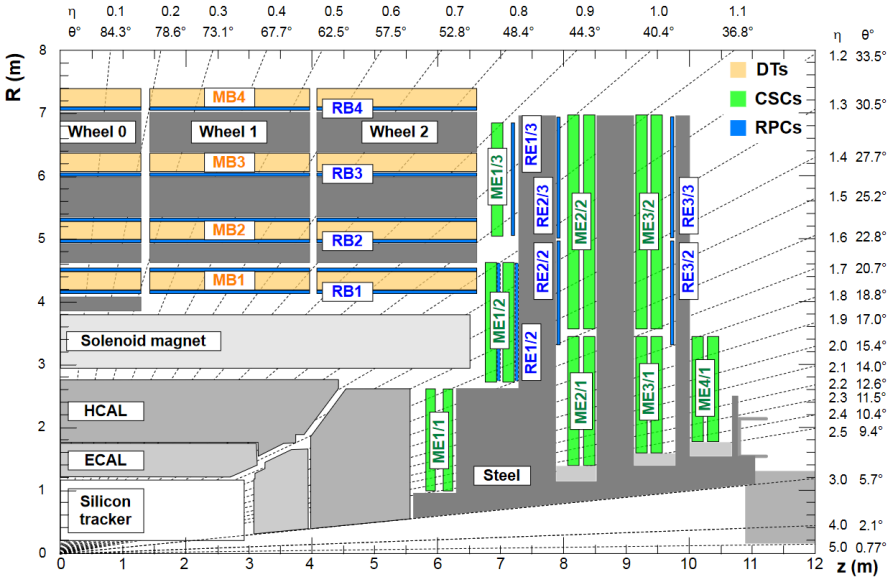

Figure 2.5: Cross section of the CMS detector, enhancing the layout of the muon system. The 4 drift tube (DT, in light orange) stations are labeled MB ("muon barrel") and the cathode strip chambers (CSC, in green) are labeled ME ("muon endcap"). Resistive plate chambers (RPC, in blue) are in both the barrel and the endcaps of CMS, where they are labeled RB and RE, respectively.

In the barrel region, the muon rate is low, and the magnetic field is uniform and contained in the steel yoke. Hence drift chambers with regular rectangular drift tubes (DT) are used. The DTs cover the pseudorapidity region $|\eta| < 1.2$ and are organized in four stations embedded in the magnetic flux return plates. The first three stations contain eight

chambers each, which measure the muon coordinate in the r–ϕ bending plane, and four chambers that provide a measurement in the z direction. The fourth station does not contain the z-measuring planes.

In the endcaps, where both muon and background rates are high, and the magnetic field is large and non-uniform, cathode strip chambers (CSC) are used. CSCs provide fast response time, fine segmentation and radiation resistance, identifying muons in the pseudorapidity range $0.9 < |\eta| < 2.4$. Four stations of 6-layer CSCs are interleaved with the flux return plates in each endcap, arranged perpendicularly with respect to the beam direction. Cathode strips run radially outward and provide a precision measurement in the r–ϕ bending plane, while anode wires lie approximately orthogonal to the strips and provide a pseudorapidity and beam-crossing time measurement of muons.

A complementary system consisting of resistive plate chambers (RPC) is also present in the barrel and endcap regions for triggering. The RPCs provide a fast, independent, and highly-segmented trigger with sharp p_T threshold in the pseudorapidity range $|\eta| < 1.6$. Six layers of RPCs are embedded in the barrel muon system, two in each of the first two stations and one in each of the outmost two. Instead, one plane of RPCs is implemented in each of the first three CSC stations in the endcap region.

2.1.7 Trigger

The LHC collides proton or heavy ion bunches at 40 MHz frequency, corresponding to 25 ns time interval between each interaction. In both Run 1 and Run 2, up to an average of 37 interactions per bunch crossing were reached in proton-proton collisions. As storing and processing all the data produced by CMS in each bunch crossing is impossible, a substantial rate reduction is mandatory. This task is performed by a two-step-triggering system [63].

The first step is called Level-1 (L1) Trigger. It consists of custom-designed, programmable electronics, implementing FPGA technology and ASICs, where speed, density and radiation resistance requirements are

more stringent. The L1 Trigger has local, regional and global components. The local triggers, also called Trigger Primitive Generators (TPG), are based on energy deposits in calorimeter trigger towers and track segments or hit patterns in muon chambers. Regional triggers combine their information and use pattern logic to determine trigger objects such as electron or muon candidates in localized spatial regions. Each object is assigned a rank determined as a function of energy or momentum and quality, reflecting the level of confidence attributed to the L1 parameter measurements. The Global Calorimeter and Global Muon Triggers determine the highest-rank calorimeter and muon objects and transfer the information to the Global Trigger, which decides if the event has to be rejected or accepted for further evaluation by the High-Level Trigger (HLT).

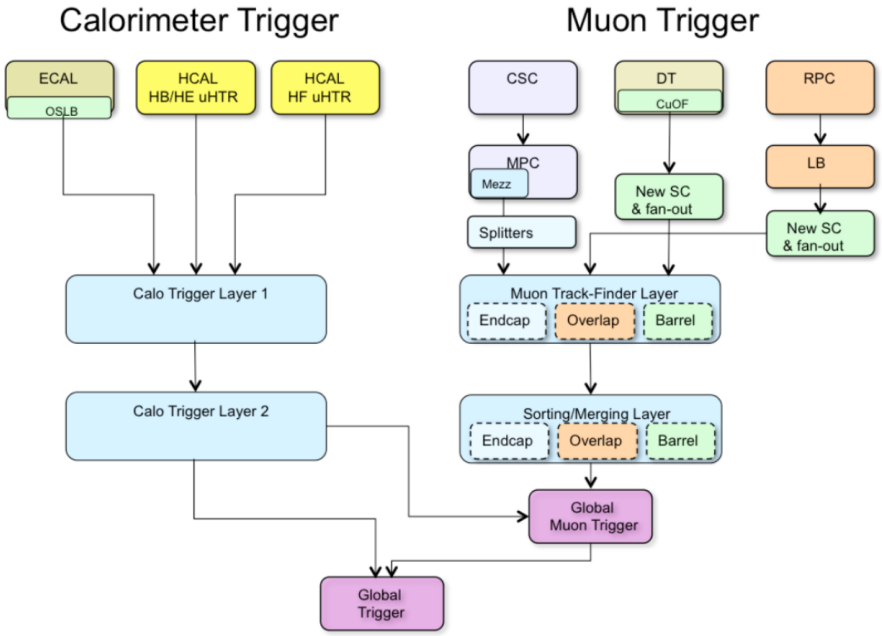

Figure 2.6: Structure of the CMS trigger system.

The HLT is the second step of the selection. Combined with the L1, it provides a rate reduction in the order of 10^6. The HLT is software-based, implemented on a dedicated filter farm of about one thousand commercial processors. HLT algorithms have access to the complete readout data. Typically, a faster, coarser version of the CMS offline event reconstruction

is performed on them. Thus the trigger decision can be taken on complex, physically meaningful quantities.

2.2 The PPS detector

The Precision Proton Spectrometer (PPS) is a magnetic spectrometer installed along the LHC beam pipe on both sides of the CMS experiment. Conceived in 2014 as a joint project by the CMS and TOTEM collaborations, it participated in the CMS Run 2 data taking under the CT-PPS acronym (CMS-TOTEM PPS), starting from 2016 [16]. In 2018, it became an integral part of CMS as PPS sub-detector.

PPS was designed to measure protons that survive interactions in the CMS Interaction Point (IP5). These protons are typically barely deflected from their nominal trajectory and remain within the beam pipe. Therefore, PPS uses the LHC magnets located between IP5 and its detector stations, installed at a distance of ≈ 200 m, to bend them out of the beam envelope.

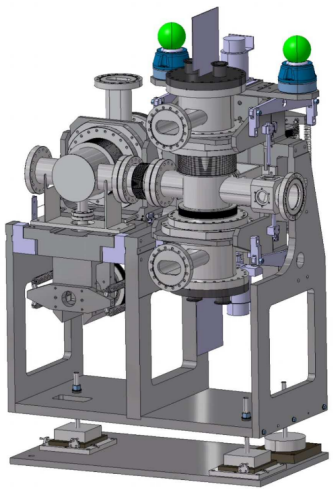

Figure 2.7: Drawing of a RP unit, with horizontal and vertical pots.

PPS detectors are hosted in mechanical movable structures called Roman Pots (RPs), originally installed for the TOTEM experiment (Fig.

2.7). They consist of a cylindrical metallic shroud, which hosts both detectors and front-end electronics, connected to a precision motor that inserts it within the beam pipe. Inside the RPs, detectors are kept cool and in vacuum. The metallic structure is made of 2 mm thick stainless steel, which is thinner only in the region closest to the beam, the so-called *thin window*. The bottom of the window is 0.15 mm thick, while the two walls are 0.5 mm.

The PPS detector apparatus, illustrated in Figure 2.8, follows the naming scheme below:

- Each side of CMS is named following the LHC nomenclature, hence *sector 45* (*arm 0*), which corresponds to the positive end of CMS. The negative end is identified as *sector 56* (*arm 1*).
- Every arm contains three RP groups called *stations*. The station 0 (or 210) is situated $\approx$ 210 m away from IP5, station 1 at 216 m and station 2 (or 220) at $\approx$ 220 m.
- With the exception of station 1, which hosts a single special RP for timing detectors, the others are further divided into RP units called *near*(*nr*) and *far*(*fr*). Stations 0 near sit 203 m away from IP5, stations 0 far at 214 m, stations 2 near at 215 m and stations 2 far at 220 m.
- Each RP unit contains three RPs, two vertical and one horizontal.

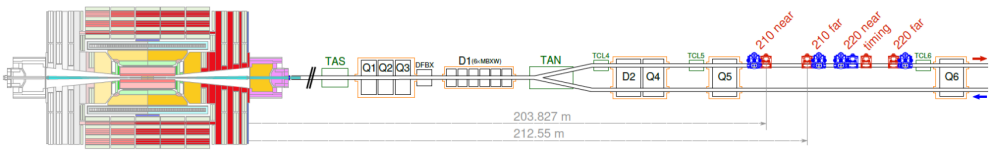

Figure 2.8: Schematic view (not to scale) of the beam line between IP5 (on the left) and the PPS RP units (marked in red and blue on the right). The red units are the horizontal RPs that have been used in Run 2. Other beam elements such as dipole (D1, D2) and quadrupole magnets (Q1-Q4), absorbers (TAS, TAN), and collimators (TCL4-TCL6) are shown.

Only horizontal RPs are used by PPS during standard operation, as the vertical ones fall out of acceptance. Vertical RPs are only used during special runs dedicated to measuring the RP alignment, in which the LHC operates with lower intensity with respect to the CMS standard conditions. In these circumstances, RPs are positioned very close to the beam and also the vertical ones are within acceptance, providing essential information for the PPS alignment procedure. A more detailed description of the PPS alignment is provided in Section 4.2

When the beams are declared stable during standard operation, PPS detectors are inserted down to ≈ 1.3 mm from the beam center. Two complementary measurements are performed on protons: tracking and timing. The former is used to reconstruct the proton kinematics, while the latter, performed on both sides of the IP, provides an additional independent measurement of the z coordinate of the primary vertex, which is important for pileup rejection purposes.

One of the most important requirements that PPS detectors need to satisfy is radiation hardness. The very high proximity to the beam leads to proton fluxes through the detectors up to $\sim 5 \cdot 10^{15}$ protons/cm^2 for 100 fb^{-1} of data-taking, which is above the typical limits of traditional detector technologies.

2.2.1 PPS tracker

The PPS tracker setup changed multiple times throughout the Run 2 data-taking. The first detectors were installed one year ahead of schedule in 2016, as a 3.4σ and 3.9σ excess in $pp \to \gamma\gamma$ at mass values around 750 GeV was detected by both CMS and ATLAS, respectively [64, 65].

As the mass range fell within the PPS expected acceptance, it was decided to anticipate the installation, thanks to the availability of legacy TOTEM silicon strip detectors. Two horizontal RPs per sector, in the 210 near and far stations, were equipped with them.

Each silicon strip detector package is made of 10 planes of edgeless, 66 $\mu\text{m} - pitch$ silicon strip sensors (Fig. 2.9a). The planes are rotated on

the xy plane, forming, in groups of five, a $\pm 45^{\circ}$ angle with the bottom of the RP. The hit efficiency per plane is estimated above 98% before radiation damage effects. Data are read out using a VFAT chip and recorded through the CMS DAQ system.

In 2017, the first 3D silicon pixel modules were installed in the 220 far stations, while the 210 near station detectors were removed. The 210 far strip detectors were replaced with new detector packages, as a countermeasure for radiation damage, both before the beginning of data-taking and at the second LHC Technical Stop (TS2).

Each pixel detector package consists of six planes of 23.4×16 mm^2 or 15.6×16 mm^2 pixel sensors, with a pixel size of 150×100 μm^2 (Fig. 2.9b). Each module is bump-bonded to either four or six PSI46dig readout chips (ROC), depending on its size. A detailed description of the 3D pixel tracker is given in Section 3.1.

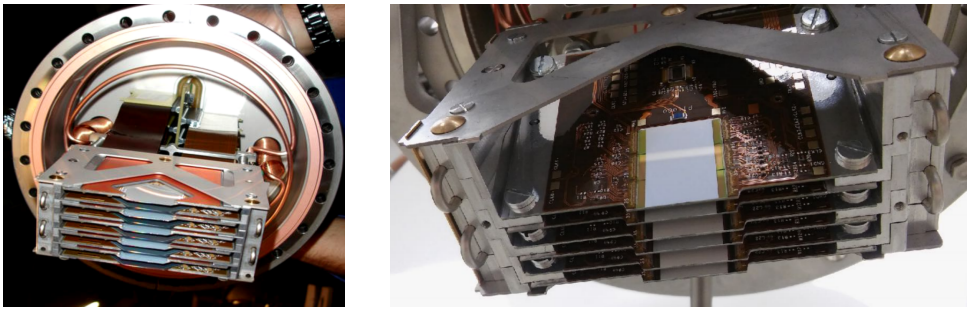

(a) **(b)**

Figure 2.9: (a): Picture of a silicon strip detector package attached to the RP flange. (b): Picture of a silicon pixel detector package.

Finally, in the 2018 data-taking, 210 far stations strips were also substituted with 3D pixel sensors.

Throughout the Run 2, the vertical RPs installed TOTEM silicon strip detector packages in the units where horizontal RPs were used. These detectors were employed only during alignment runs or special TOTEM runs.

2.2.2 PPS timing

When two proton bunches cross, interaction vertices are confined in a volume of a few centimetres in length (the bunch longitudinal dimension has $\sigma_z \approx 7.5$ cm). A high precision timing measurement on protons in both PPS arms allows to constrain further the volume where the interaction originating those protons happened.

By measuring the time difference Δt between the time of flights of the two protons, it is indeed possible to reconstruct the longitudinal vertex position as $z_{pp} = c\Delta t/2$, and thus reject all vertices that are incompatible with this measurement. Detectors with 10–30 ps time resolution are able to disentangle about 50 pileup events.

During Run 2, one RP per sector (station 1) was equipped with timing detector packages. Each detector package consists of four planes of timing sensors.

Besides one plane of Ultrafast Silicon Detectors (UFSDs) [66] that was used for R&D purposes in 2017, the main technology used in Run 2 relied on ultrapure single-crystal chemical vapour deposition (scCVD) diamonds. Diamond sensors are 4.5×4.5 mm^2, 500 μm scCVD crystals. On Single Diamond (SD) detector planes, four sensors are glued in a row, as shown in Figure 2.10a, on top of the hybrid board, and their readout electrodes are segmented. An active area of $\sim 20 \times 4.5$ mm^2 divided in 12 channels is thus obtained. Double Diamond (DD) planes have another four sensors glued symmetrically on the other side of the board. Symmetric diamond pads are connected and read together to roughly double their signal amplitude without increasing noise levels. DD planes were installed for 2018 data-taking (Fig. 2.10b).

Signals coming out of diamond detectors are processed via three stages of amplification, then converted to digital data containing the time of arrival and time over threshold of the detected signal. Further information on the PPS timing detector setup and performance is available in [67].

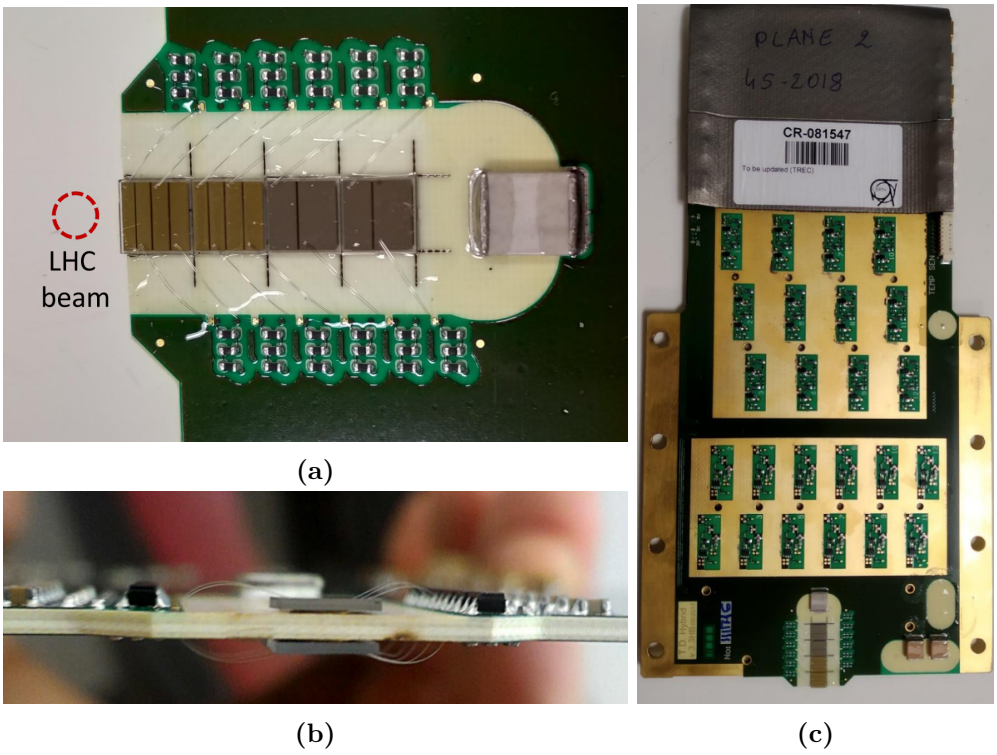

(a) **(b)** **(c)**

Figure 2.10: (a): Top view of a timing detector: sensor segmentation in strips and bonding wires are visible. (b): Lateral view of a double diamond detector, with crystals glued on both sides of the hybrid board. (c): Full hybrid board hosting sensors, amplification channels and HV distribution.

Chapter 3

Run 2 PPS pixel tracker

During PPS Run 2 data-taking, 3D pixel tracking detectors were used in one detector station per sector in 2017 and in all stations in 2018. PPS implemented 3D silicon pixel technology for the first time in CMS achieving remarkable performance in very challenging conditions.

An in-depth description of the Run 2 PPS pixel tracker will be given in the following sections. A report on its successful operation in 2017 and 2018 will be presented and the results of the tracker performance studies will be shown.

3.1 Detector apparatus

Each PPS tracking RP housing pixel detectors (Fig. 3.1) is equipped with the so-called *champignon* (named after its shape), which is the mechanical assembly of detectors and front-end boards that is mounted on the RP and moved during data-taking to approach the detectors to the LHC beam.

A steel flange separates the portion inserted in the RP box, which is put under vacuum during operation, from the outer part, kept at ambient pressure. The portion under vacuum is the so-called *detector package*, a mechanical structure containing six planes of detectors. Each one consists of the sensor, its readout chips and the flexible circuit that connects

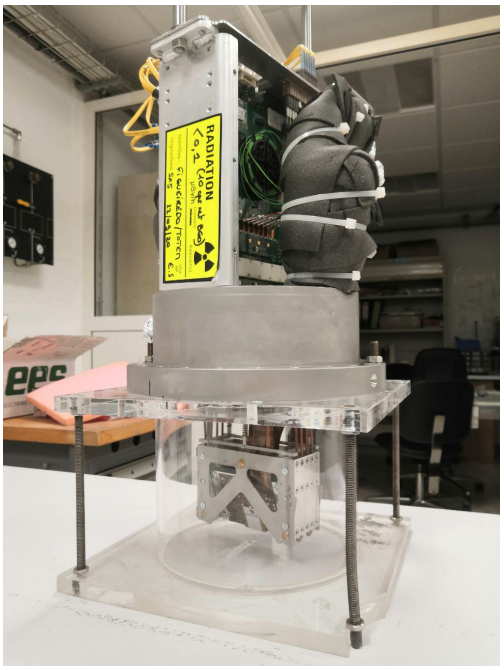

Figure 3.1: Mechanical structure (champignon) containing the portcard and holding the detector package (visible below). The cooling pipes are insulated with grey foam tape to prevent ice formation.

them to the control and communication board. The latter is named *portcard* and extends from inside the RP box, through an epoxy-sealed slit, to the ambient pressure side of the champignon, where most of its electronic components are located. The portcard is further connected to the back-end part of the DAQ and control system via electrical and optical connections. On the champignon sides, insulated cooling pipes bring a fluorine-based coolant in the under-vacuum portion of the RP and are thermally coupled to the detector package.

In the following paragraphs a focus on each detector and DAQ chain component will be provided.

3.1.1 PPS 3D pixel sensors

PPS tracking detectors are exposed to a very harsh radiation environment, given their extreme proximity ($\approx$ 1.5 mm) to the LHC beam. These

conditions lead to proton fluxes up to $5 \cdot 10^{15}$ p/cm^2 for 100 fb^{-1} integrated luminosity and large non-uniformity in the irradiation, presenting about two orders of magnitude proton flux variations in less than 2 mm (see Fig. 3.2) [16].

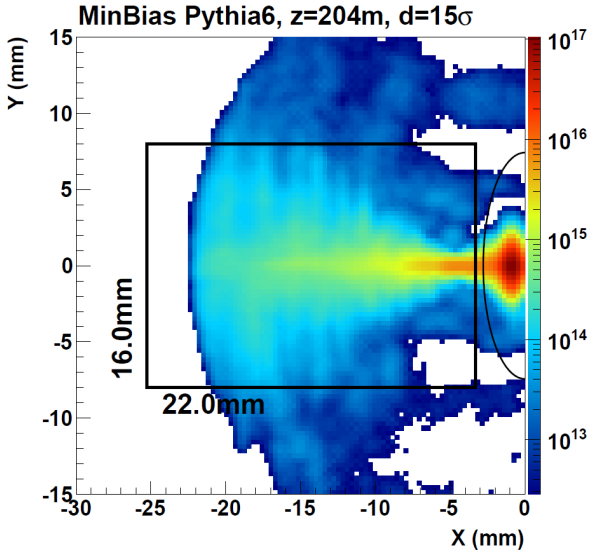

Figure 3.2: Simulated proton fluence in the tracking station at 204 m from the IP for an integrated luminosity of 100 fb^{-1}. The rectangle indicates the detector surface transverse to the beam assuming a detector tilt angle of 20°. The ellipse shows the 15σ beam contour. In the most irradiated area, a fluence of about $5 \cdot 10^{15}$ p/cm^2 is foreseen.

Such operating conditions presented a challenging scenario for traditional planar pixel silicon sensors. When traversing silicon detectors, particles release part of their energy, possibly displacing the silicon atoms that form the crystal lattice of the sensor. This generates the so-called *charge trapping* effect [68], which consists in electron-hole pairs released by the ionizing particle being captured in meta-stable energy states, effectively reducing the charge collection efficiency of the sensor [69, 70]. Irradiation can further cause an increase in leakage current, change of effective doping (and depletion voltage) and damage to silicon oxide layers (the latter is typically more relevant for irradiated electronics).

The effect of charge trapping can be contained by shortening the path length that charges need to travel to reach the electrode [71]. However,

in planar sensors this corresponds to reducing the sensor thickness and thus the amount of charge released.

The 3D pixel technology [72] represents a solution to this issue by implementing vertical columnar electrodes, etched in the sensor bulk [73], effectively decoupling the sensor thickness from the distance between electrodes (see Fig. 3.3).

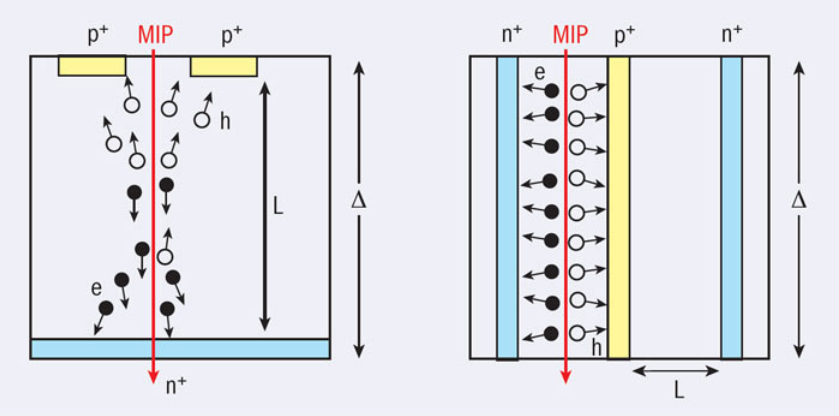

Figure 3.3: Cross-section of a planar (left) and 3D (right) pixel silicon sensor of thickness Δ. The electrodes (yellow) separation L is decoupled from Δ in 3D technology.

This solution comes at the cost of sensors that are more complex to manufacture, present higher capacitance, and contain dead regions, since particles going through a hollow column will not be detected. 3D silicon sensors were thoroughly studied for the ATLAS Insertable B-Layer (IBL), and it was shown that this latter disadvantage can be easily overcome by tilting the sensors to form an angle between the incoming particle and the columns [74].

3D pixel sensors further represent an optimal choice for PPS because of the facilitated implementation of slim or active edges [75]. Tracking detectors must approach the beam without strongly interfering with it, disrupting the LHC operation; therefore being efficient close to the sensor edge effectively extends the detector acceptance.

The short distance between electrodes in 3D sensors also plays a role in the depletion voltage, which is typically one order of magnitude lower

than in planar sensors.

For all these reasons, PPS decided to equip its tracking stations with 3D silicon pixel detectors [16]. An extensive study and characterization of the production for the PPS Run 2 is provided in [76, 77].

During Run 2, PPS used 3D sensors produced by CNM (Centro Nacional de Microelectrónica, Barcelona, Spain). Double-sided processing was used to manufacture non-passing-through 200-μm-deep 10-μm-diameter columns, in 230-μm thick sensors with p-type bulk [78]. p^+ bias electrodes were thus implanted on one side and shorted, while n^+ columns were created from the other side, with dedicated pads for readout chip bump-bonding.

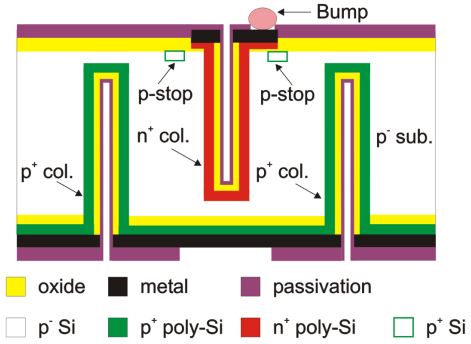

Figure 3.4: Schematic cross-section of the PPS Run 2 sensors. Reproduced from [79].

Sensors were segmented in pixels of size 150×100 μm^2, using two possible electrode configurations identified as 1E and 2E, illustrated in Figure 3.5. In the former configuration each pixel has four bias columns in the corners and one readout electrode in the center; in the latter configuration, each pixel has two shorted readout columns surrounded and six bias columns. The 2E configuration further improves the radiation resistance, effectively shortening the average distance between electrodes [80]. It, however, presents a higher electrode density, increasing the manufacturing complexity and thus lowering the production yield.

In the end, a mixture of 1E and 2E designs were used in the installed detector packages, preferring 2E sensors over 1E, some of which were still

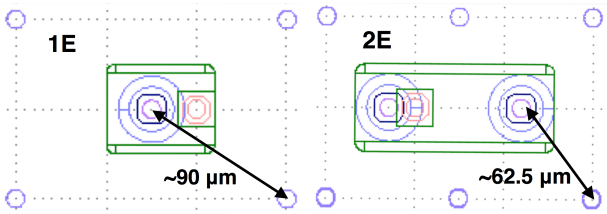

(a) 1E pixel layout. **(b)** 2E pixel layout.

Figure 3.5: The figure shows the two 3D pixel electrode layouts used by PPS in Run 2.

used as a second-choice solution.

The size of the full sensor was dictated by the dimension of the readout chips (ROCs): 80×52 pixels. Modules capable of housing a 2×2 and 3×2 ROC matrix were produced and used in data-taking, with other configurations only employed in irradiation and preliminary tests.

Each sensor implemented a 200 μm slim edge, created with a triple p-type column fence. Furthermore, pixels located within the sensor, at the edge of two or four ROCs, were doubled in size for preserving enough space for ROC positioning (Fig. 3.6).

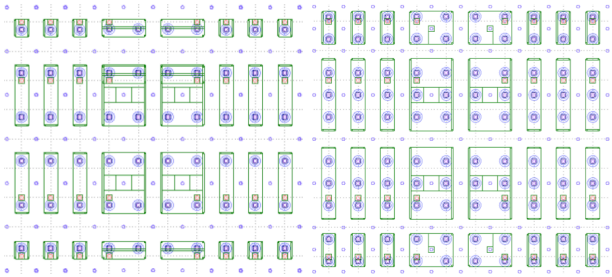

(a) 1E edge layout. **(b)** 2E edge layout.

Figure 3.6: PPS Run 2 sensor layout at the corner of 4 ROCs.

The minimum mechanical and electrical requirements were:

- Wafer bow < 200 μm
- Depletion voltage $V_{depl} < 20$ V
- Breakdown voltage $V_{bd} > 35$ V

- $[I(25\text{ V})/I(20\text{ V})] < 2$

Current-Voltage (IV) characteristics were measured with a probe station on bump-bonded modules, and they were classified depending on their current per ROC at room temperature and operation voltage V_{op}, where $V_{op} = V_{depl} + 10$ V. V_{depl} is the depletion voltage, measured with Capacitance-Voltage measurements and typically in the 5–10 V range. The classification is the following:

- Class A: $I(V_{op}) < 2\ \mu$A
- Class B: $2\ \mu\text{A} < I(V_{op}) < 10\ \mu$A
- Class C: $I(V_{op}) > 10\ \mu$A

In total, 46 acceptable sensors belonging to classes A and B were identified. Twenty-four sensors were used to equip four detector packages: two of them were used both in 2017 and 2018, whereas the other two were installed only in 2018. A detailed evaluation of these sensors before installation is presented in Ref. [77].

3.1.2 PSI46dig readout chip

The 3D pixel sensors installed in PPS are bump-bonded to the PSI46dig readout chip used by CMS [81]. This chip is the evolution of the PSI46v2 ROC [82] and has been designed at PSI for the Phase1 pixel detector upgrade of CMS [83]. It shares with the PSI46v2 chip the 250nm CMOS technology and its well-studied architecture. The full ROC layout is shown in Figure 3.7.

The PSI46dig ROC consists of 52×80 Pixel Unit Cells (PUCs), which amplify and discriminate signal from background, organized in 26 Double Columns (DCs) of 2×80 pixels. Every DC is controlled by its periphery, which hosts buffers for timestamps and data. The chip periphery, shared by all the DCs, digitizes the signal and handles the communication with the outer electronics. A block schematic is shown in Figure 3.8.

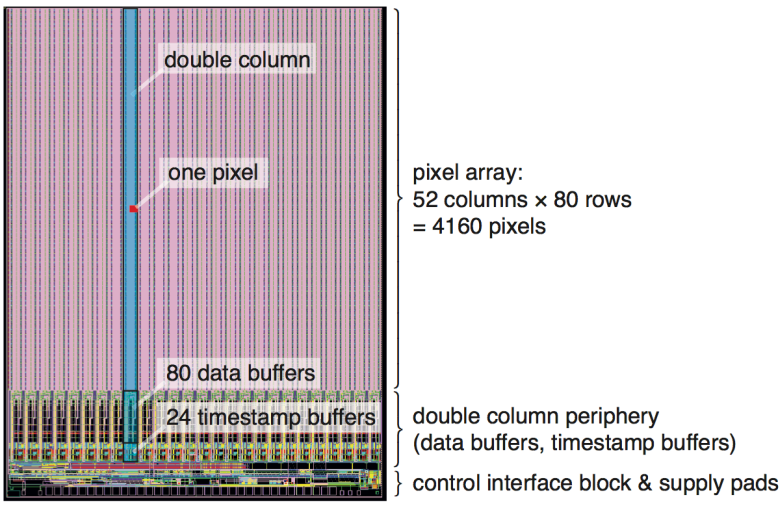

Figure 3.7: Full layout of the PSI46dig pixel chip [84]. Highlighted are the areas of a single pixel, a double column, the data buffers and the time-stamp buffers. The periphery and the supply pads handle trigger information, buffer data and the communication with the outside world.

The PUC receives the signal through the bump-bond and amplifies it with a two-stage system made of a pre-amplifier and a shaper. The shaper output is then sent to the discriminator, which compares the signal with a preset threshold, and, whenever it is higher, stores it in a sample-and-hold circuit, after the chosen delay, recording its peak. At the same time, a fast signal is sent to the input gate of the whole DC logical OR, so that the event timestamp is saved in the buffer.

The timestamp is the momentary content of an 8-bit counter that is increased every LHC clock cycle, whose frequency is 40 MHz. It allows the hit to be matched with the trigger associated with the LHC bunch crossing (BC or BX), which runs on the same clock as the ROC. The trigger maximum latency must not exceed 255×25 ns $= 6.375$ μs.

Once the sample-and-hold circuit of a pixel is in HOLD state, waiting for its signal to be copied in the data buffers located in the DC periphery, it becomes insensitive. The column drain operation ends as soon as the signal height information is transferred. Hits in subsequent clock cycles can be correctly assigned to a specific timestamp as long as no more than

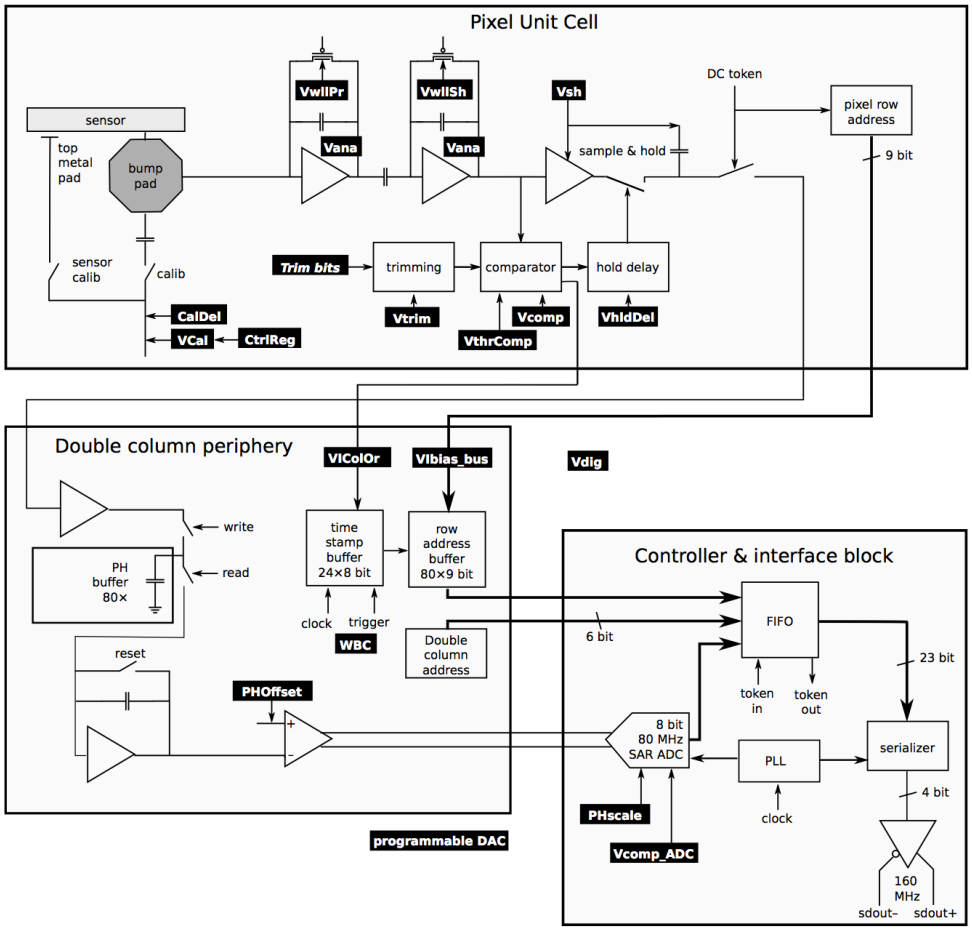

Figure 3.8: Outline of the PSI46dig main blocks.

two column drain operations are pending.

The comparator threshold is controlled through three DAC values. The first is VthrComp (also called VcThr), which sets a global value for all pixels. The other two, called TrimBit and Vtrim, set, respectively, a threshold adjustment on the single pixel and its maximum range, which is common for all the PUCs. It has to be noted that the signal sent to the comparator is negative and the VthrComp DAC value is proportional to the threshold voltage. It follows that a higher VthrComp value is equal to a lower threshold applied on the signal in terms of absolute value. VTrim acts by lowering the threshold. When the TrimBit is set to its maximum value (15) no reduction is applied, whereas, when it is set to its minimum (0), the threshold is maximally lowered.

Everything up to this point happens without involving a trigger signal reception. Once the trigger is detected, a second 8-bit counter that runs with a programmable offset (WBC) with respect to the primary one is saved and compared with the DC periphery timestamp. When a match is found, the hits are put in halt to avoid overwriting, the data are saved in the central readout buffer, and the particle signal is digitized by an 8-bit ADC, shared by the whole ROC. By setting two DAC values, PHOffset and PHScale, it is possible to control the offset and gain of the ADC, in order to match the full range of signals. During this step, it is very important that the WBC value is properly set to reproduce the delay between the hit timestamp and the trigger, so that every hit is associated with the correct bunch crossing.

The current of the analog part of the ROC, namely the comparator and amplifier, is controlled via a DAC called Vana. Its nominal value is 24 mA, which corresponds to roughly 6 μA per pixel. The current flowing through the digital part of the ROC, and in particular the ADC, is controlled via the Vdig DAC.

Every hit in the central buffer consists of a 23-bit word containing: the column number (6 bits), the row number (9 bits), and the digitized pulse height (8 bits). The readout buffer is designed as a FIFO with simultaneous read and write capability, and has a storage capacity of 64

such 23-bit words. Every DC gets re-enabled for regular operation as soon as the data are transferred.

3.1.3 Flex hybrid

Each PPS 3D pixel sensor, bump-bonded to the ROCs, is glued on a flexible kapton circuit, the so-called *flex hybrid*. The circuit was designed in Genova to meet the specific PPS requirements, integrating the functionalities of the CMS Phase 1 Pixel High Density Interconnect (HDI) [85].

As illustrated in Figure 3.9, the flexible circuit is glued to a 0.5 mm thick support layer of Thermal Pyrolytic Graphite (TPG) wrapped in aluminium foil to improve heat dissipation. In later modules the TPG was substituted with aluminium, as tests showed temperature levels being far from the specified limits. The support layer is about 86×59 mm^2 large.

The sensor is glued to the support, in the flex circuit cutout, with the readout chips facing the TPG layer. Wire bonds are used to provide electrical connections.

Besides providing an electrical interface between the readout chips and the portcard, the flex hybrid hosts the Token Bit Manager (TBM), which is responsible for coordinating the data readout of all the ROCs. Run 2 modules were equipped with the TBM08c version [86].

The TBM has two cores (A and B) working independently: core A reads out, in order, ROCs $0, 1, 2$ and core B ROCs $3, 4, 5$. Whenever one ROC is missing, the token ring can be configured to skip it. The TBM job is not only to coordinate the readout of all the ROCs of a sensor, it also manages the clock and L1 trigger distribution, contains Data Keepers and a Communication and Control hub, which distributes the I^2C commands to the correct ROC. If a second trigger signal arrives while the readout operation is not yet finished, the TBM saves it in one of its 32 slots-deep buffer. When half of these slots are full, subsequent triggers are stored until the maximum capacity is reached. However, no token is sent to the ROC and the TBM sends out for them only the header and trailer

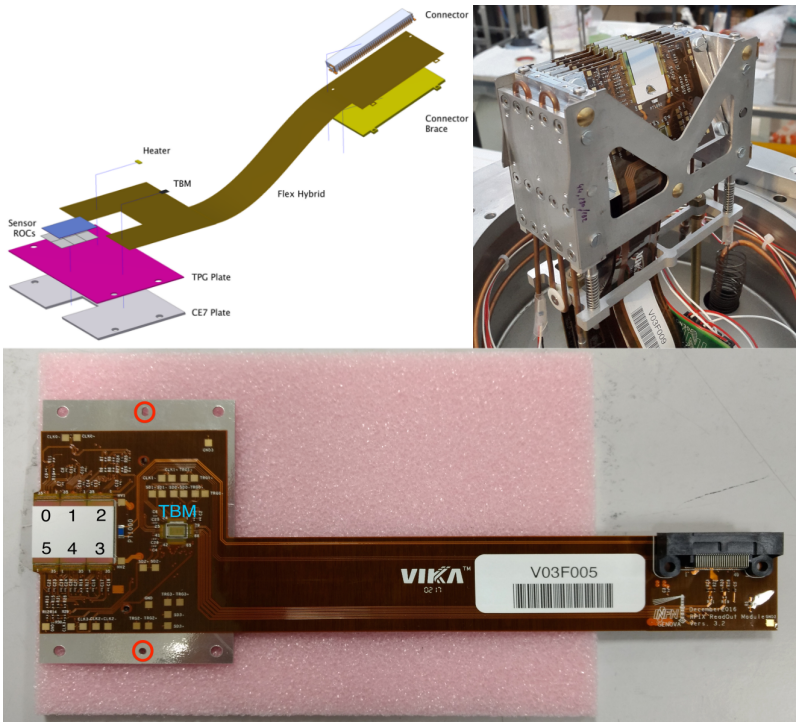

Figure 3.9: Top left: exploded view of a PPS Run 2 module. Top right: picture of the assembled detector package, made of six 3D pixel planes. Bottom: picture of a PPS Run 2 flex hybrid with a 3×2 sensor wire-bonded on it. The numbers on it indicate the ROC numbering convention used in the DAQ. In case of 2×2 modules, ROCs 2 and 3 are not present.

patterns, with the *NoTokenPass* flag, so that the back-end MicroTCA board is kept synchronized.

Additional features of the TBM, such as counters for multiple purposes, automatic detection of high occupancy events, and programmable delays for data streams and signals, can be controlled via a set of registers.

After receiving the 160 MHz data stream from the ROCs, the TBM multiplexes them to form a 320 MHz signal, which is passed to a 4-to-5 bit encoder that transforms it in non-return-to-zero inverted code, reaching the 400 Mhz required for the transmission to the portcard.

3.1.4 Portcard

The portcard (Fig. 3.10) distributes the low and high voltage power to the modules, controls and programs the mezzanines (*slow controls*), and delivers clock, trigger and I^2C configurations to TBMs and ROCs (*fast controls*).

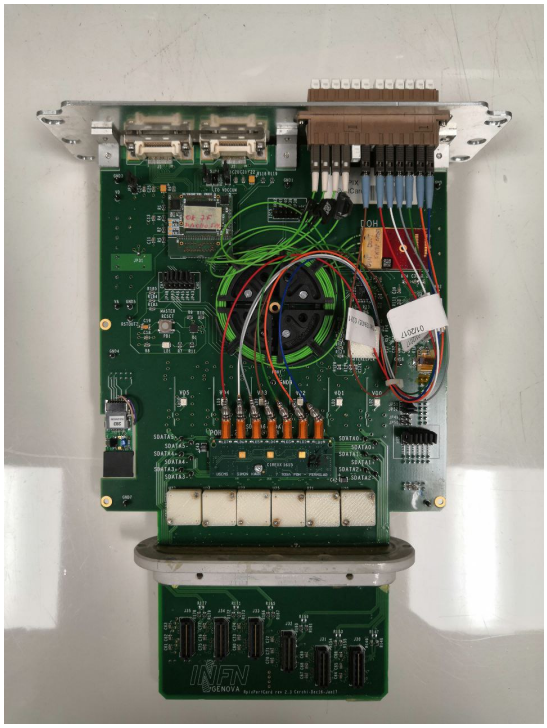

Figure 3.10: PPS Run 2 portcard with the components mounted on it. The six connectors at the bottom provide the links to the flex hybrids and are located inside the secondary vacuum of the pot, while the remaining part of the board sits outside.

Slow control signals are managed with a system derived from detectors used in the TOTEM experiment. The Detector Opto-Hybrid Mezzanine (DOHM), located outside the portcard in a dedicated patch panel, converts and distributes the optical signals received from the back-end DAQ cards. Multiple portcards can be electrically connected forming a loop with the DOHM (*control ring*) [87].

Each portcard houses a Communication Control Unit Mezzanine (CCUM)

[88], which receives the configurations to be sent to other programmable devices present on the same portcard via I^2C protocol: the mDOH, TPLL, QPLL, Delay25, GateKeeper, LCDS drivers, and POH7 mezzanine. They all play a role in the distribution and communication of fast commands.

Fast commands, received via optical fibers, are converted to electrical Low-Voltage Differential Signals (LVDS) by the modified DOH (mDOH). The mDOH communicates on four lines, two of which receive clock and data, while the other pair sends clock and data. As trigger signals are encoded in the received clock, a dedicated chip, the Tracker Phase-Locked Loop (TPLL), separates the two. Subsequently, the Quartz PLL (QPLL) reduces the jitter of the clock signal, before feeding it to the Delay25 chip. As the name implies, the Delay25 applies programmable delays to all the fast command lines, then forwards them to the GateKeeper, where they are converted from LVDS to LCDS (Low-Current Differential Signals). Finally, LCDS drivers send the signals to the TBM of each module.

Data output from the ROCs, encoded by the TBM, is sent out via six 400 MHz LCDS lines to the Pixel Opto-Hybrid (POH7) mezzanine, which converts electrical signals to optical ones and transmits them to the DAQ back-end.

3.1.5 Back-end DAQ

The back-end electronics for the PPS DAQ is derived from the CMS Phase 1 Pixel detector. Based on MicroTCA modular electronics, a MicroTCA carrier hub (MCH) card is used as communication interface between the MicroTCA electronics and the local area network (LAN). The MicroTCA backplane is used to distribute clock, trigger and fast commands, that are received from the Trigger Clock Distribution System (TCDS) via a CMS-custom module called AMC13 [89].

The three back-end cards necessary for the PPS detector operation are implemented on three FC7 MicroTCA FMC carriers [90]. They are called the *Tracker Front-End Card* (Tracker FEC), the *Pixel Front-End Card* (Pixel FEC), and the *Pixel Front-End Driver* (FED) [91].

The Tracker FEC is connected via optical fibers to the DOHM, through which it sends slow control signals to the portcards connected in the control ring. The Pixel FEC communicates directly with the portcards via fiber-links, distributing fast commands. Finally, the FED receives, via optical fibers, data sent from the TBMs, builds the PPS pixel events, and routes them to the CMS Central DAQ system.

All the PPS back-end DAQ is located in the so-called *CMS counting room*, about 100 meters underground, and $\approx$ 200 m long optical fibers connect it to the rest of the PPS electronics positioned either near the RP locations (DOHM) or in the RPs (portcard).

The whole PPS DAQ system is controlled by the CMS Pixel Online software (POS). This application, based on the XDAQ toolkit, is a modified version of the CMS central pixel detector software. It allows not only to acquire data during central CMS data-taking but also to perform calibrations and tests necessary for operating the detector.

3.2 Detector operation

In 2017, the first two 3D pixel detector packages were installed in PPS, in the two 220 far stations, replacing the TOTEM silicon strip detectors.

The operation was smooth, with pixel detectors behaving as expected. After ≈ 3 fb^{-1}, collected over about one month, an issue with one of the RP position sensors arose. This inconvenience required RP insertions to stop until the first LHC Technical Stop (TS1), at the end of June 2017, when it was repaired. This can be noticed as the first integrated luminosity plateau in Figure 3.11.

PPS kept taking data flawlessly in the following months; however, starting from the end of July, pixel detectors started showing some efficiency loss in the most irradiated area. In an effort to compensate for this effect, the bias voltage was progressively increased from the initial operating value of 30 V up to the 70 V reached at the beginning of August. Further increases were not possible without increasing the noise level significantly, and disrupting the detector readout.

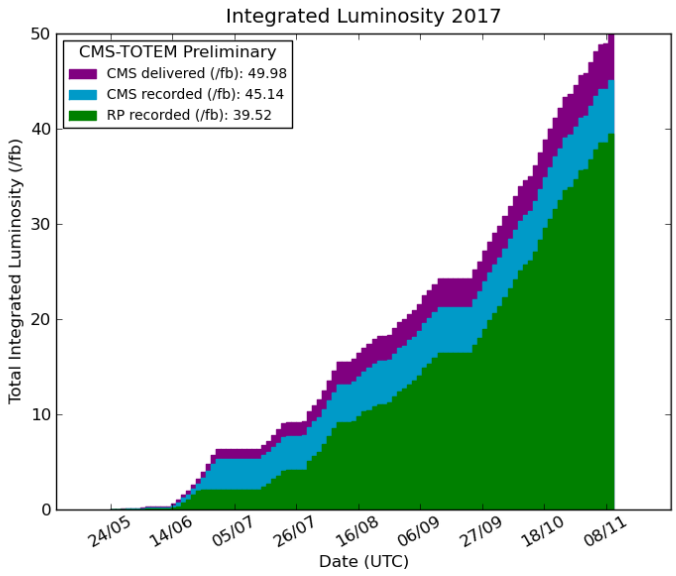

Figure 3.11: The plot shows the comparison between the total integrated luminosity delivered to CMS, recorded by CMS and recorded by PPS, in 2017, as a function of time. The plateaus in the end of June and in the central weeks of September correspond to LHC Technical Stops.

During TS2, in the central weeks of September 2017, it was decided to physically move the detectors in the vertical plane by inserting a 1 mm thick shim below the mechanical structure that held it in place. Such intervention effectively shifted the most irradiated region away from the radiation damage and improved the detector performance.

The detector continued taking data in 2017, reaching a total of $\approx$ 40 fb^{-1} collected, corresponding to about 88% of the total integrated luminosity recorded by CMS. Besides the RP position sensor issue mentioned above, RP insertions always occurred. The integrated luminosity difference was mainly due to the delay caused by the RPs insertion, which can only occur when LHC declares "stable beams".

In 2018, two new detector packages were installed, substituting the strip detectors still used in the 210 far stations. The packages used in 2017 were re-installed, although swapped between the two sectors. This operation effectively flipped the detectors upside-down so that the radiation damage formed in 2017 would be positioned far away from the

irradiation peak.

The data-taking was highly stable, without any stop due to issues with the PPS tracking detectors, as it can be observed in Figure 3.12. Minimal interventions (noisy pixels masking, threshold measurements, etc.) were required to keep the detectors calibrated and functional.

Vertical movements were again performed, this time in both LHC Technical Stops (TS1, mid June, and TS2, mid September), by inserting shims of 500 μm thickness, to better exploit the maximum 1 mm range.

As will be presented in the following Section, radiation damage formation was observed coherently with 2017.

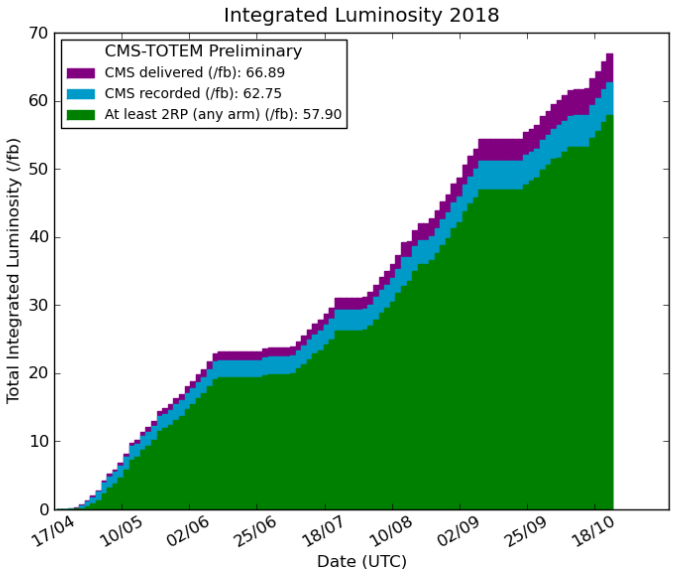

Figure 3.12: The plot shows the comparison between the total integrated luminosity delivered to CMS, recorded by CMS and recorded by PPS (when at least two RPs were inserted), in 2018, as a function of time. The plateaus in June and in the central weeks of September correspond to LHC Technical Stops.

PPS collected ≈ 58 fb^{-1} in 2018, corresponding to the 92.2% of the total CMS recorded luminosity.

3.3 Performance studies

The performance of the Run 2 PPS pixel tracker has been thoroughly studied and characterized. This Section focuses on the pixel tracking detector performance, while the proton reconstruction performance will be the subject of Chapter 4.

To properly present the results, the tracking algorithm is first described in Section 3.3.1, then the efficiency measurement method together with the results are discussed in Section 3.3.2.

3.3.1 Tracking algorithm

The PPS pixel tracker implements a combinatory pattern-based track reconstruction algorithm, which was chosen for its simplicity while still being very efficient performance- and computing-wise. In fact, given the low noise levels of the PPS pixel detectors and the low number of tracks to be reconstructed in each event, the number of hit combinations remains under control and can be handled in a combinatory approach.

The track reconstruction happens through three steps: conversion of digital signals to hits, hit clusterization and track reconstruction.

The first step consists in converting binary data acquired by the DAQ system to the local coordinates of the pixels that have been hit. Once this information is available, a second algorithm recognizes clusters of pixels on each plane, typically formed by a maximum of two pixels in each direction (row or column).

Figure 3.13 shows the cluster size distributions in the horizontal (x) and vertical (y) direction. Proton tracks, that are typically parallel to the beam (z-axis), impinge at an angle with the detector planes, because of the planes tilt around the y-axis. This causes a higher chance for charge sharing in the horizontal direction than on the vertical one. The fraction of size-two clusters is found in agreement with test beam results shown in Ref. [77].

A detector hit is reconstructed in the local detector plane reference

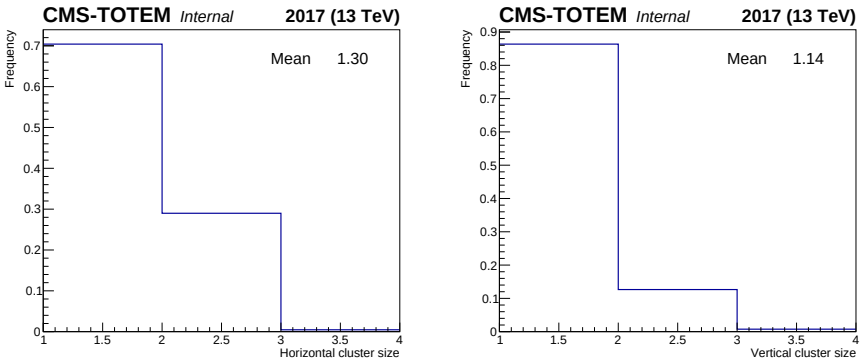

Figure 3.13: Horizontal (left) and vertical (right) cluster size distributions.

frame in the second step. Since a digital measurement of the charge deposited in each pixel is available, the hit coordinates are calculated as the barycenter of the charge distribution, effectively enhancing the overall resolution of the detector by exploiting the charge-sharing capability of the sensor.

Finally, the third reconstruction step generates the track objects, which carry all the track information:

- the RP where the track was measured;
- the χ^2/NdF of the track fit;
- the global coordinates of the track hit, which is the intersection of the track with a conventional scoring plane located at the position of the first plane of the detector package;
- the angles that the track forms with the coordinate axes;
- the hits that have been used in the track fit.

The reconstruction is run independently for every tracking station. If more than 60 hits in the same station or more than 20 hits on the same plane of a station are detected, the track reconstruction for that station is not performed. This approach limits the computation time required by the algorithm and effectively excludes events with anomalous

noise levels or in which the proton interacted upstream of the tracking station, generating a shower of particles. Such events are not interesting for physics measurements, as the proton is lost.

The algorithm calculates the track parameters by fitting the hits with a 3-dimensional line. A fixed limit of 5 on the χ^2/NdF is chosen, and the reconstruction starts by looking into all the hit combinations with the maximum number of planes contributing to the track. Every track that passes the χ^2 check is saved and the hits that contributed to it are removed from the possible combinations. At this point, the algorithm searches for other tracks, reconstructed with a lower number of planes, that can still pass the χ^2 test.

This operation is repeated until a minimum of 3 planes contribute to the track, which is the minimum requirement to identify a going-through particle. If more than 10 tracks are detected, all tracks are discarded, because such events are likely to be caused by proton interactions upstream, as mentioned above.

As visible in Fig. 3.14a, $\sim$ 90% of the reconstructed tracks is fitted with hits from all detector planes and the χ^2 distribution (Fig.3.14b) is compatible with the 8-degrees of freedom scenario (2×6 variables -4 parameters).

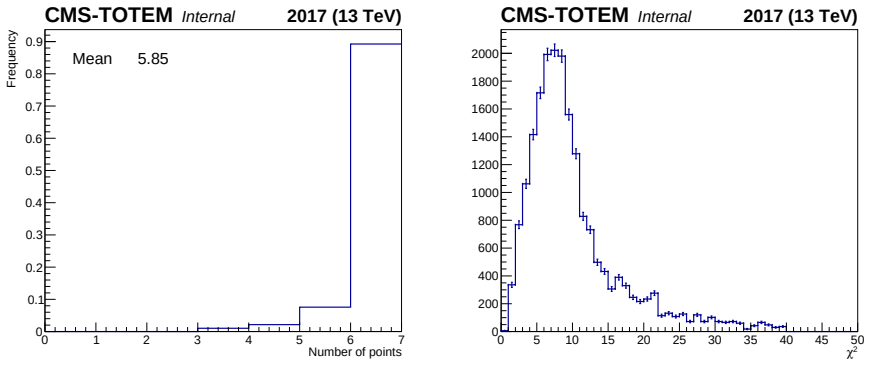

(a) **(b)**

Figure 3.14: Left: typical distribution of the number of points used for fitting. Right: χ^2 distribution for tracks reconstructed with six points.

Finally, the intersection between the detected tracks and the scoring

plane mentioned above is computed after the proper coordinate transformation to switch from the local to the global reference frame (cf. Fig. 3.15 and 3.16). Such transformation makes use of the tracking station global alignment constants measured with the methods that will be presented in Section 4.2.

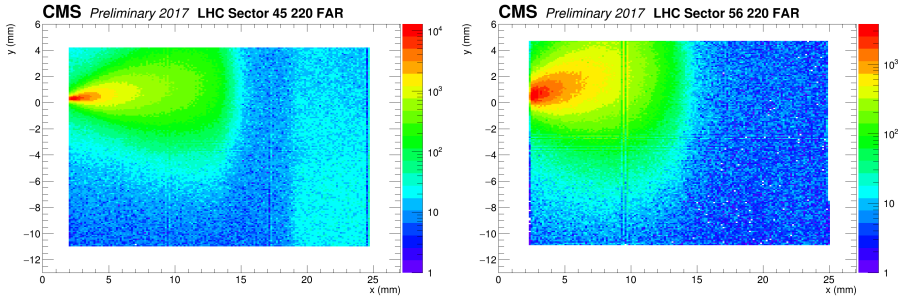

Figure 3.15: Typical track hit distributions for 2017 data-taking. The x–y coordinates of the hit are the intersection of the track with the scoring plane.

3.3.2 Tracker efficiency

One of the most relevant parameters to characterize the performance of a detector is its efficiency. PPS detectors are exposed to a very challenging environment, in which very high and non-uniform irradiation impinges on the detectors.

3D pixel silicon sensors are used because of their inherently higher radiation hardness, although the non-uniformity still affects the performance of the PSI46dig ROCs.

The following paragraphs explain the radiation effects on PSI46dig ROCs, the method used to measure the tracker stations efficiency, and present a summary of the Run 2 results.

Radiation effects on the PSI56dig ROC

In the context of detector studies that preceded the first installation of 3D pixel modules in 2017, beam test at the CERN IRRAD facility had shown timing issues on the modules which were not uniformly irradiated

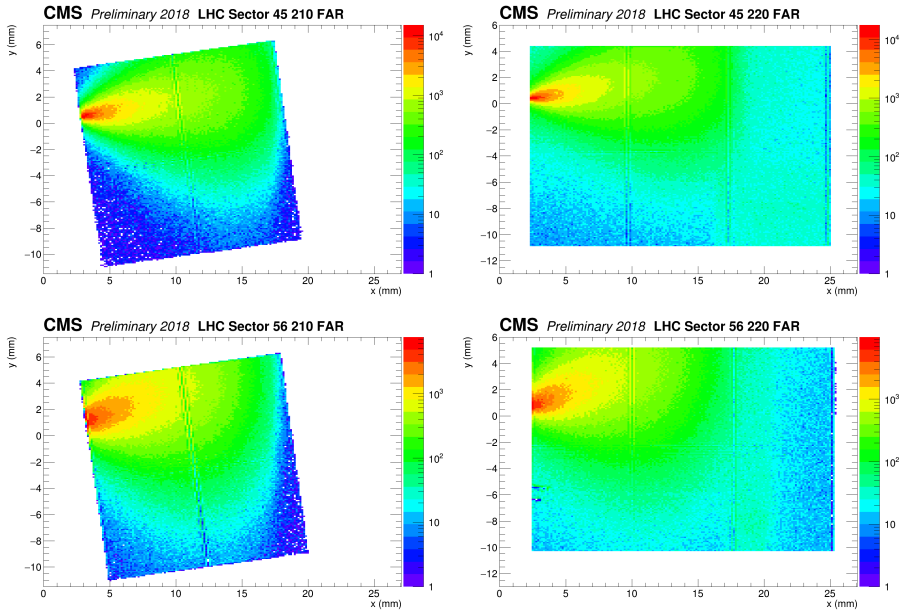

Figure 3.16: Typical track hit distributions for 2018 data-taking. The rotation in 210 far stations reflects an 8° rotation of the RP box about the z, for better acceptance.

[77]. Further investigation of the problem, traced it back to effects caused by radiation damage in the ROC.

In integrated circuits, irradiation causes irreversible damage in silicon oxide layers. This process mainly affects the input transistors of amplifiers located in each ROC pixel unit, causing their transconductance to decrease, therefore lowering the current flowing through them and reducing the gain of the amplifier. When it happens, output signals, as shown in Figure 3.17, have lower amplitude, longer rise time, and increased time walk.

Due to this issue, the signals coming from damaged pixels can be slowed down to the point where they do not cross the threshold in the time window associated with their corresponding bunch crossing (BX), and the hits are assigned to the following one, making the module inefficient. Since it is impossible to apply a delay selectively to damaged pixels, there is no way to recover the performance.

It must be noticed that this effect does not have a sharp threshold,

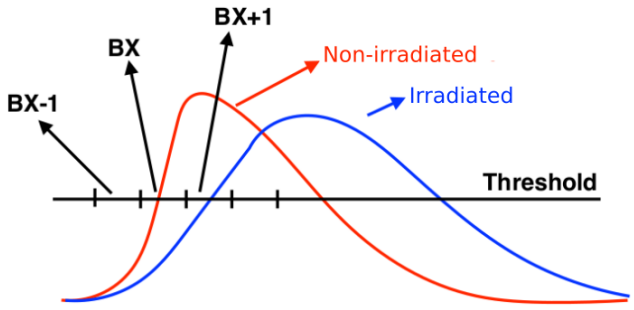

Figure 3.17: Difference between the output signals of an irradiated versus a non-irradiated amplifier for the same input charge.

as the signal delay depends on its height, which is subject to Landau fluctuations. This effect was studied before installation by performing an irradiation campaign at an X-ray facility available at CERN [77]. The overlap between the timing window corresponding to a bunch crossing for an irradiated and non-irradiated pixel was measured via the charge-injection calibration circuit of the ROC. Results showed a 66% drop in the overlap at a dose equivalent to the one reached by the most irradiated pixels after $\approx$ 8.7 fb^{-1} of data-taking. At the dose corresponding to $\approx$ 13.7 fb^{-1} the overlap became null. Therefore efficiency losses caused by radiation damage in the ROCs are expected to appear when pixels pass these levels of dose.

Efficiency measurement method

The efficiency measurement of a PPS tracking station is a two-step procedure: the first part measures the efficiency of each pixel of the detector planes in the tracking station, while the second combines the information of all planes to compute the efficiency of the station as a whole.

The first step begins by considering a pixel in one plane out of six (plane k). Only tracks fitted with points belonging to at least three other planes are considered. The efficiency of the pixel can be computed as the ratio between the number of tracks going through it in which it contributed to the fit, to the total number of tracks passing through the selected pixel:

$$\varepsilon_k = \frac{N_{4,5,6}(k)}{N_3(\bar{k}) + N_{4,5,6}(k \vee \bar{k})} \tag{3.1}$$

where in $N_{i,j,l}(k/\bar{k})$, i, j, l represents the possible number of hits allowed in the track fit, and the content of the parentheses shows whether plane k contributes to the track (k) or not ($\bar{k}$). E.g.: $N_{3,4,5}(\bar{k})$ stands for the number of tracks reconstructed with a number of hits between 3 and 5, and plane k cannot provide one of the hits.

The efficiency of each pixel is measured with the formula above by using a minimum-bias sample of data, in which the trigger prescale was either 1 or constant. The latter requirement is equivalent to considering events with variable trigger prescale and re-weighting them depending on it.

The result of the first step of the measurement is thus a set of efficiency maps, similar to the one illustrated in Figure 3.18, for each detector plane.

The second step of the efficiency measurement requires the combination of the pixel efficiency of each plane. As proton tracks are mainly parallel to the LHC beam, the combined efficiency of the station is studied as a bi-dimensional function of the global x–y coordinates. A data-driven approach is used to model the kinematics of the proton tracks. Selecting a reference data sample collected shortly after the detector installation ensures that the sample is not affected by radiation damage. Therefore, this collection of tracks reproduces the x–y and angle distributions of data.

The intersections of each track with the detector planes are computed, and the efficiency evaluated in the first step for the intersected pixel is assigned. The six efficiency values are thus combined combinatorially to compute the probability of having at least three efficient pixels out of six, assigning a combined efficiency to each track.

The values obtained are plotted as a function of the track x–y global coordinates and normalized by the track x–y distribution, which is equivalent to computing the average measurement for all the tracks going through the same global x–y histogram bin (cf. Fig. 3.19). The final

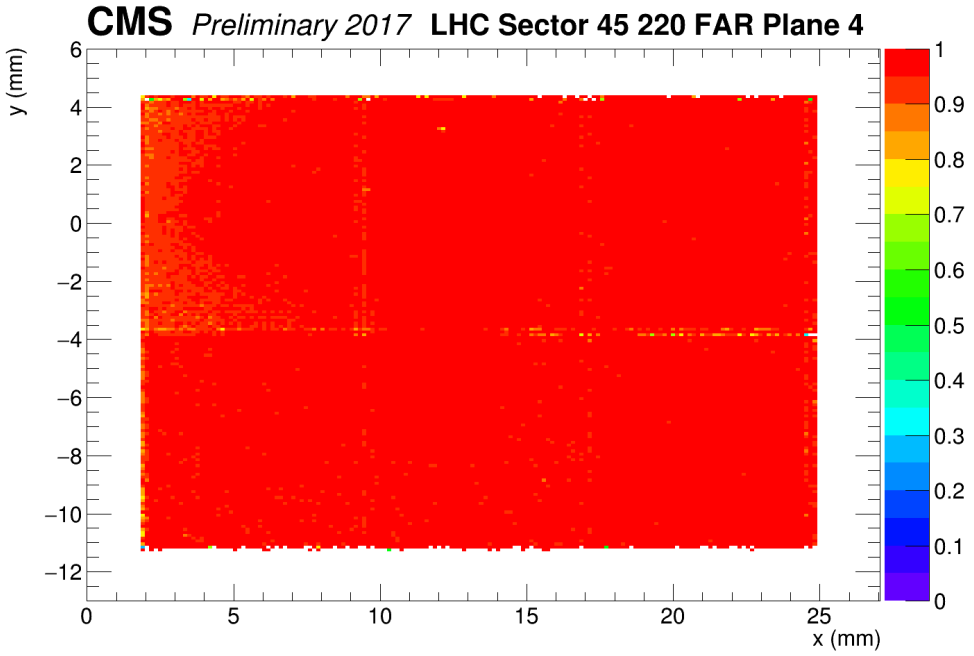

Figure 3.18: Example of the efficiency map of a pixel detector plane measured at the beginning of the 2017 data-taking. Lower efficiency bins appear at the ROCs interface, as a result of the doubled size of the pixels at the ROCs internal edges.

efficiency measurement performed with this method is referred to as *radiation efficiency*, as it is mainly affected by irradiation effects.

Statistical uncertainties of the measurement have been evaluated with a toy Monte Carlo and turned out to be negligible. Systematic uncertainties related to the choice of the reference sample have been estimated by re-evaluating the efficiency for multiple samples. No strong dependence is observed, with maximum fluctuations within 1%.

Efficiency studies results

The efficiency of each detector package was studied in 2017 and 2018 with the method mentioned in the paragraph above. The measurement is performed over long periods of data-taking (so-called *eras*) to provide average measurements for physics analyses. More frequent evaluations

are however done (roughly every 1 fb^{-1}), for detector study purposes.

The initial efficiency measurement showed a very high detector performance in both years, with an average value above 98%, as Figure 3.19 shows for 2017.

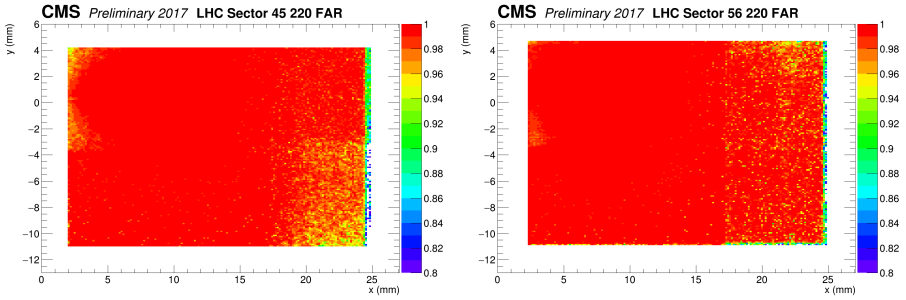

Figure 3.19: Efficiency maps of the detector packages, computed on the first 2.4 fb^{-1} of data collected in 2017 and shown as a function of the global x–y coordinates. The slightly lower efficiency on the right side of the maps is caused by that region being covered by 5 planes instead of 6; a similar effect in the bottom-right corner of RP 45-220-far is due to non-optimal detector configuration.

Radiation damage effects were clearly visible after $\approx$ 10 fb^{-1}. The efficiency maps (Figure 3.22 and 3.23) show the progressive efficiency loss and the expansion of the damaged region, which anyway remains limited to a small number of highly irradiated pixels.

The presence of multiple damaged regions is due to the detector movements performed during LHC Technical Stops (see Section 3.2).

In order to qualitatively estimate the efficacy of such detector movements, an *irradiation peak region* is defined by modelling the track hit distribution. Track maps are sliced vertically in bins of x. The corresponding y projections have a gaussian profile and are fitted, yielding gaussian amplitudes, means and sigmas depending on x. These are further fitted as a function of x as $1/x$ fit for the amplitudes, linearly otherwise.

The lower x_{min} boundary is defined as the left edge of the sensor with no empty pixels, whereas the upper x_{max} boundary is the x coordinate yielding as integral a given fraction (30%) of the track population, estimated with the $1/x$ function. The same fraction is used for all RPs.

The irradiation peak region is centered in y according to the linear fit of the gaussian means, and its width in y is defined as 0.75 times the value obtained by the linear fit to the gaussian sigmas.

A complementary area is also defined as the difference between a rectangle inscribed in the high population part of the distribution and the peak area with the same lower x boundary.

An example of the shapes obtained for the irradiation peak and complementary area is shown in Figure 3.20.

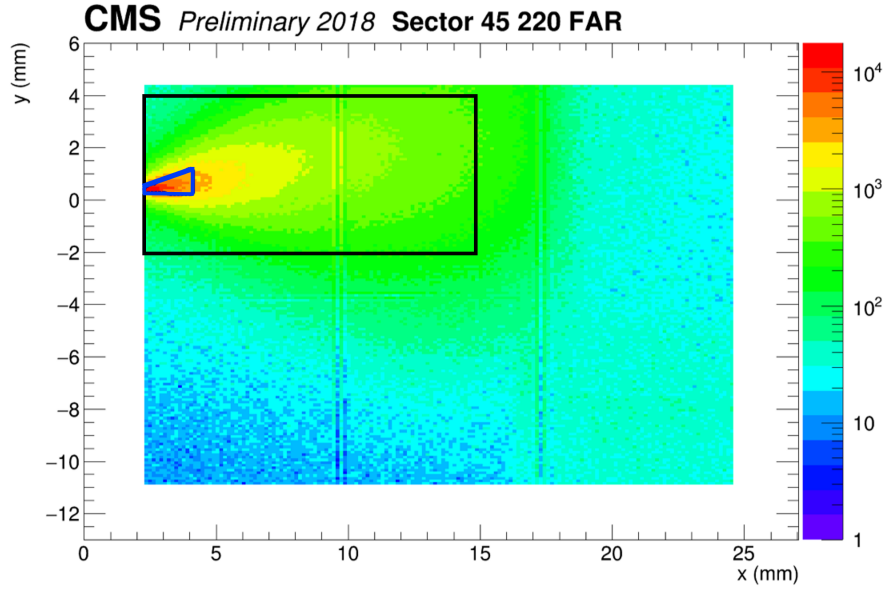

Figure 3.20: Example of the irradiation peak area (blue wedge) and the complementary one (black rectangle), defined and superimposed on an early 2018 track hit distribution.

The average efficiency of pixels in the two regions is computed. If the damage remains within the irradiation peak area, it is expected that the average efficiency in the complementary area remains constant with increasing integrated luminosity.

Figure 3.21 shows the results for 2018 data. Because of the more peaked proton track distribution observed in sector 45, the radiation damage is larger, and because of acceptance differences, 220 far stations always suffer greater damages with respect to 210 far ones.

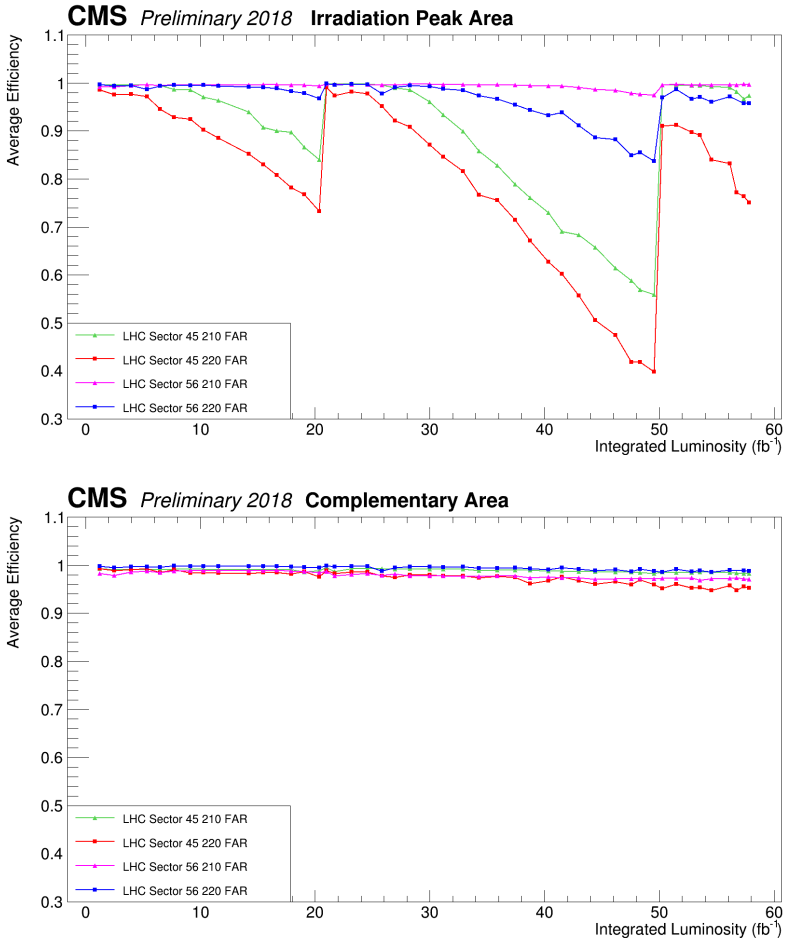

Figure 3.21: Average detection efficiency in the irradiation peak region (upper) and complementary region (lower). Each point corresponds to an efficiency measurement performed over $\sim$ 0.5–1 fb^{-1} of data.

These results show that the vertical movement of the detectors during Technical Stops restores the performance, granting an almost complete recovery. The only exception is the sector 45 220 far station, where the 500 μm movement performed during TS2 was not enough to shift the irradiation peak entirely out of the damaged region.

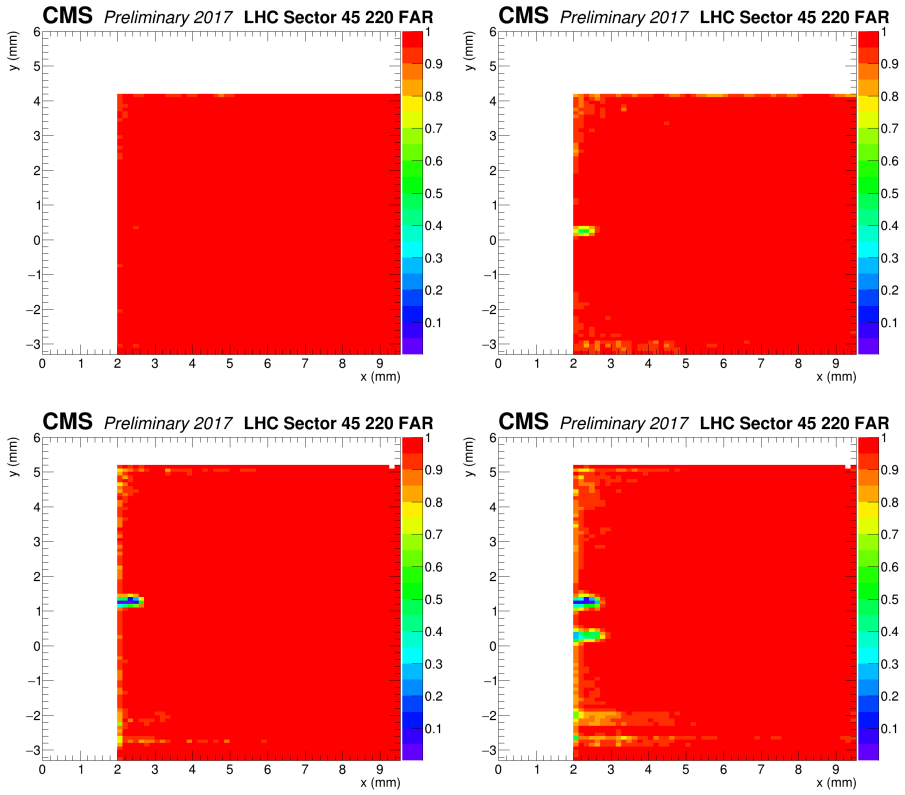

Figure 3.22: Evolution of the detector package efficiency in the detector region closest to the beam for RP 45-220-far, computed with data collected in 2017. During the TS, detectors in both sectors were vertically shifted by 1 mm upwards.
From left to right, top to bottom: efficiency computed after the detector collected $L_{INT} = 0$ fb^{-1}, $L_{INT} = 8.7$ fb^{-1}, $L_{INT} = 18.9$ fb^{-1}, $L_{INT} = 29.5$ fb^{-1}, respectively. Each efficiency map is produced using a small data sample of ~ 0.5–1 fb^{-1}.

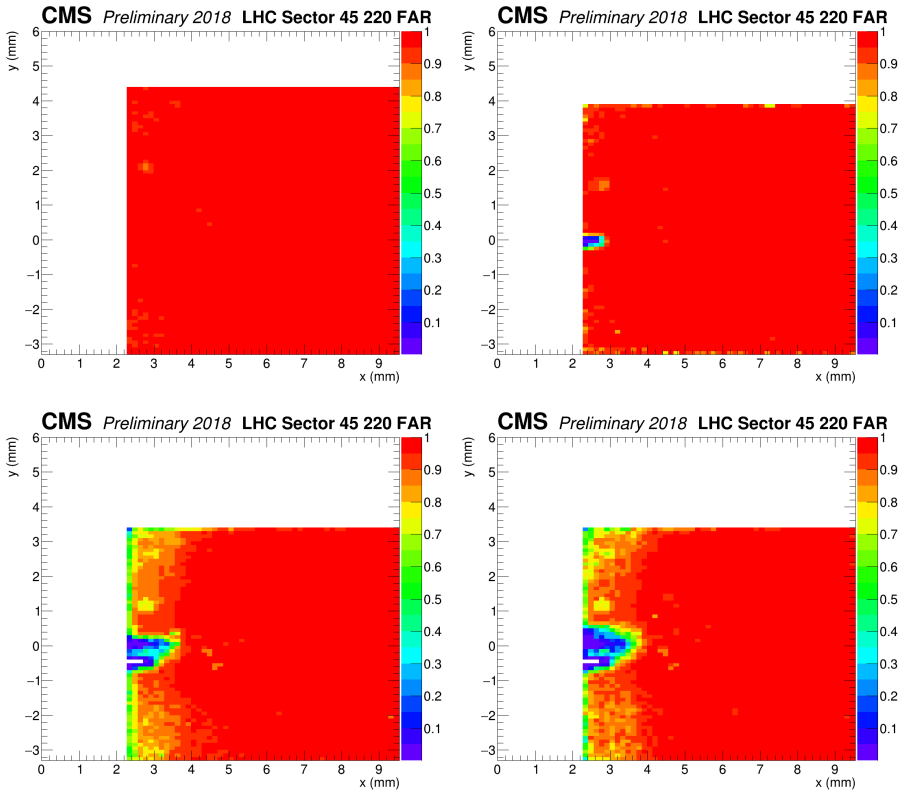

Figure 3.23: Evolution of the detector package efficiency in the detector region closest to the beam for RP 45-220-far, computed with data collected in 2018. During each TS, detectors in both sectors were vertically shifted by 0.5 mm downwards.
From left to right, top to bottom: efficiency computed after the detector collected $L_{INT} = 0$ fb^{-1}, $L_{INT} = 21.0$ fb^{-1}, $L_{INT} = 50.3$ fb^{-1}, $L_{INT} = 57.8$ fb^{-1}, respectively. Each efficiency map is produced using a small data sample of ~ 0.5–1 fb^{-1}.

Chapter 4

Proton reconstruction

In order to reconstruct the proton kinematics from tracks measured by PPS detectors, many elements come into play. This chapter presents an overview of the proton reconstruction and provides insight into the calibration procedures needed for it.

The first section focuses on the proton transport from the IP to RPs. PPS adopts the same approach that is used in accelerator physics to model the proton propagation, which is referred to as *beam optics*. The most relevant quantities for proton reconstruction are introduced, and the calibration of the beam optics is discussed.

The second section covers the procedure that is used to align PPS detectors. This is a complex operation that requires multiple steps, some of which are performed during dedicated data-taking runs, while others are repeated after each RP insertion. Precise knowledge of the PPS detector alignment is essential for proton reconstruction.

The proton reconstruction, based on calibrated optics and alignment, is discussed in the third section. Here an overview of the acceptance limitations imposed by upstream beam elements (collimators) is also presented. Furthermore, the proton simulation is described because it represents a vital tool for PPS data analyses.

Finally, in the last section, the proton reconstruction efficiency is presented with the method used to estimate it. Proper knowledge of the effi-

ciency is an essential ingredient for adequately understanding the overall PPS detector performance and a crucial input for physics analyses.

4.1 LHC optics and proton transport

The magnetic lattice of the LHC in the segment between the CMS IP and the RP positions consists of 29 main and corrector magnets.

The proton kinematics is described by the vector $\mathbf{d} = (x, \theta_x, y, \theta_y, \xi)^T$, where (x, y) and (θ_x, θ_y) indicate the transverse positions and angles. ξ is the fractional momentum loss

$$\xi = (p_{\text{nom}} - p)/p_{\text{nom}} \tag{4.1}$$

where p_{nom} and p are the nominal beam momentum and the proton momentum, respectively.

The proton kinematics $\mathbf{d}$ at a distance s from the IP, is related to its kinematics at the IP, $\mathbf{d}^*$[1], through the transport matrix $T(s, \xi)$:

$$\mathbf{d}(s) = T(s, \xi) \cdot \mathbf{d}^* \tag{4.2}$$

The elements of the transport matrix

$$T(s,\xi) = \begin{pmatrix} v_x & L_x & m_{13} & m_{14} & D_x \\ \frac{\mathrm{d}v_x}{\mathrm{d}s} & \frac{\mathrm{d}L_x}{\mathrm{d}s} & m_{23} & m_{24} & \frac{\mathrm{d}D_x}{\mathrm{d}s} \\ m_{31} & m_{32} & v_y & L_y & D_y \\ m_{41} & m_{42} & \frac{\mathrm{d}v_y}{\mathrm{d}s} & \frac{\mathrm{d}L_y}{\mathrm{d}s} & \frac{\mathrm{d}D_y}{\mathrm{d}s} \\ 0 & 0 & 0 & 0 & 1 \end{pmatrix} \tag{4.3}$$

are the so-called *optical functions*, or linear lattice functions.

They may depend on the LHC settings during operation, such as the crossing angle and β^*, i.e. the betatron function value at the IP. The half crossing angle of the beams at the IP is usually called α.

During LHC Run 2, the crossing angle lay on the horizontal plane, as

[1] the * symbol is used to indicate quantities measured at the IP

it will be in LHC Run 3, multiple combinations of β^* and α were used by the accelerator during data-taking. Typical values for β^* lie in the 0.27–0.4 m range, while half crossing angles remain within 120 μrad and 185 μrad.

LHC employed different strategies throughout the years. In 2016, β^* remained constant, while different crossing angle values were used before and after the second Technical Stop.

In 2017, most of the data were recorded at four discrete values of α (150, 140, 130, and 120 μrad). The highest value was used at the beginning of the fill, and then the crossing angle was reduced to compensate for the instantaneous luminosity loss while taking data. Different β^* values were used before and after TS2.

In 2018, the crossing angle changed continuously during each fill between 160 and 130 μrad, and β^* changed in two steps (0.3, 0.27, and 0.25 m).

4.1.1 Optical functions

In the proton transport matrix, the elements m_{ij} in Eq. 4.3 connect the horizontal and vertical scattering planes. At the LHC, these terms are set to zero nominally for collision optics.

Since the PPS tracking stations directly measure the proton positions, these are the most relevant variables to compute using the transport matrix. They can be written as:

$$\begin{aligned} x &= x_0 + D_x(\xi) \cdot \xi + L_x(\xi) \cdot \theta_x^* + v_x(\xi) \cdot x^* \\ y &= y_0 + D_y(\xi) \cdot \xi + L_y(\xi) \cdot \theta_y^* + v_y(\xi) \cdot y^* \end{aligned} \tag{4.4}$$

with every term described in the following.

The horizontal and vertical magnifications

$$v_{x,y} = \sqrt{\beta_{x,y}/\beta^*} \cos \Delta\mu_{x,y} \tag{4.5}$$

and the effective lengths

$$L_{x,y} = \sqrt{\beta_{x,y}\beta^*} \sin \Delta\mu_{x,y} \tag{4.6}$$

are functions of the LHC betatron amplitudes $\beta_{x,y}$, their value β^* at IP5 and the relative phase advance

$$\Delta\mu_{x,y} = \int_{\text{IP}}^{\text{RP}} \frac{\mathrm{d}s}{\beta_{x,y}} \tag{4.7}$$

The terms $D_x(\xi)$ and $D_y(\xi)$ denote the so-called horizontal and vertical dispersions which are defined by the focusing properties of the LHC magnetic lattice.

Finally, x_0 and y_0 are the beam center coordinates, shifted because of detector misalignments. After the proper detector alignment procedure, described in Section 4.2, the beam appears at $x_0 = y_0 = 0$).

Since the distribution of interaction vertices in the transverse plane is very narrow, $\sigma(x^*) \approx \sigma(y^*) = \mathcal{O}(10\mu\text{m})$, the terms that contain the horizontal and vertical magnifications in Eq. 4.4 are negligible in the proton reconstruction.

In the horizontal plane, the dispersion plays a dominant role. Even though θ_x^* corrections are relevant, especially at high ξ, in the low ξ range $x(\xi)$ can be approximated as

$$x \approx D_x \cdot \xi \tag{4.8}$$

In the vertical plane, instead, the dominant term is due to the effective length, with only minor corrections given by D_y. Therefore

$$y \approx L_y(\xi) \cdot \theta_y^* \tag{4.9}$$

As mentioned above, optical functions may depend both on the β^* and crossing angle. However, when varying these parameters during data-taking, LHC exploited the so-called Achromatic Telescopic Squeezing (ATS) optics, which, among its features, keeps the optical functions

in Eq. 4.5 and 4.6 constant despite the change in β^* [92].

The proton reconstruction is thus unaffected by changes in β^*, while the crossing angle needs to be taken into account.

4.1.2 Optics calibration

Optical functions are determined with a combination of simulation tools and data-driven methods. PPS uses data from the LHC infrastructure databases, such as the currents of the magnet power converters and their calibration data, as input for the Methodical Accelerator Design program (MAD-X). This tool, a general-purpose beam optics and lattice software,computes the optical functions for each combination of settings used by the LHC.

Lattice functions are thus extracted at each RP location, and calibration points are derived from data to tune them. MAD-X is able to compute the vertical effective length $L_y(\xi)$ with good accuracy, shown in Figure 4.1, provided that a dedicated calibration (described in Refs. [93, 94]), using proton elastic scattering events, is performed.

As described by Eqs. 4.4, the θ_y^* of protons at the IP reflects in a smearing of the vertical distribution of protons at the RP locations. Therefore, when $L_y(\xi)$ crosses zero at $\xi_0 \approx 0.025$, the y distribution of the tracks exhibits a "pinch" (cf. Figure 4.2). The measurement of the pinch position thus provides a calibration point for the horizontal dispersion D_x, as it connects the ξ value at which the vertical effective length vanish to the x coordinates of the pinch. This procedure is used to calibrate the LHC optics model, as described in [2].

A complementary approach is also used to cross-check and improve the optical functions calibration: the observation of (semi)-exclusive dimuon pairs (Sec. 1.1.1) [20]. A high purity data set of exclusive $\mu\mu$ events is selected, in which the central $\mu\mu$ system carries the momentum lost by the two forward protons.

The proton fractional momentum loss can be estimated as shown in

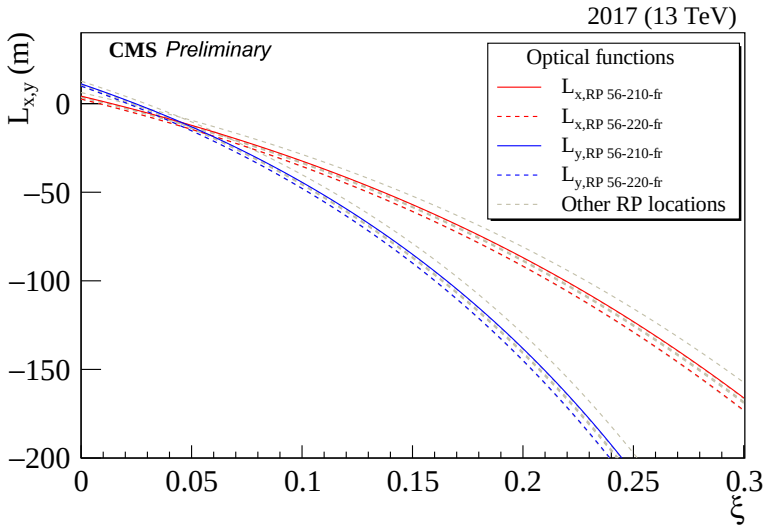

Figure 4.1: ξ dependence of the horizontal and vertical effective lengths L_x and L_y. The horizontal effective length $L_x(\xi)$ decreases faster than the vertical function L_y; both of them cross zero at low ξ, at $\xi < 0.04$. The grey lines show the TOTEM RPs used only for calibration [2].

Eq. 1.2, and reported below in the $\mu\mu$ case:

$$\xi_{\pm}(\mu^+\mu^-) = \frac{1}{\sqrt{s}}\left[p_T(\mu^+)e^{\pm\eta(\mu^+)} + p_T(\mu^-)e^{\pm\eta(\mu^-)}\right] \tag{4.10}$$

Exclusive $\mu\mu$ events form a peak in the $\Delta\xi = 1 - \xi(p)/\xi(\mu^+\mu^-)$ distribution, where $\xi(p)$ is the proton fractional momentum loss reconstructed from PPS, and $\xi(\mu^+\mu^-)$ is computed with Eq. 1.2. This peak is used to calibrate D_x such that the signal peak appears at $\Delta\xi \approx 0$ within resolution. This procedure provides a second independent calibration method for D_x.

The pinch method is limited by how accurately the pinch position can be determined. In fact, even if L_y is null at the pinch point, a vertical smearing is still present because of the vertical magnification and higher order effects. A further correction using the exclusive $\mu\mu$ physics process thus helps improving the D_x calibration.

Table 4.1 shows combined results of the pinch and (semi)-exclusive $\mu\mu$ methods.

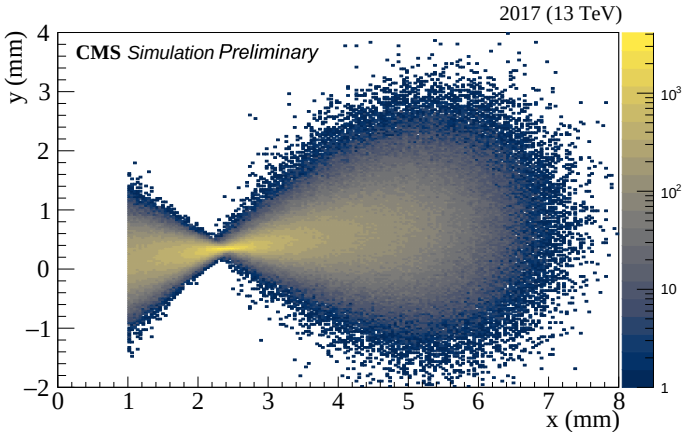

Figure 4.2: Illustration of the "pinch" or focal point at $x = x_0$ where the vertical effective length vanishes: $L_y(\xi_0) = 0$, given the relation $y \approx L_y(\xi_0) \cdot \theta_y^*$. The simulation takes into account that the small vertical dispersion moves particles upward according to $\Delta y = D_y \cdot \xi$ with increasing x and ξ [2].

Year	Half crossing angle (rad)	Sector 45 (cm)	Sector 56 (cm)
2016	185	-9.7 ± 0.4	-6.7 ± 0.4
2017	120	-10.4 ± 0.8	-7.9 ± 0.6
2018	120	-11.3 ± 0.9	-8.7 ± 0.7

Table 4.1: Measured horizontal dispersion values D_x in RP 210-fr at $\xi = \xi_0$. The resulting D_x value is the weighted average of the $L_y = 0$ and (semi)-exclusive $\mu\mu$ results.

With the calibration points mentioned above and other measured constraints (beam position, beam position monitors readings, crossing angle) the MAD-X optics model is used to extend the dispersion values to the total PPS ξ range, as shown in Figure 4.3.

Further calibration of the optics is performed to improve the vertical dispersion D_y measurements and estimate uncertainties on them; this is described in detail in [2].

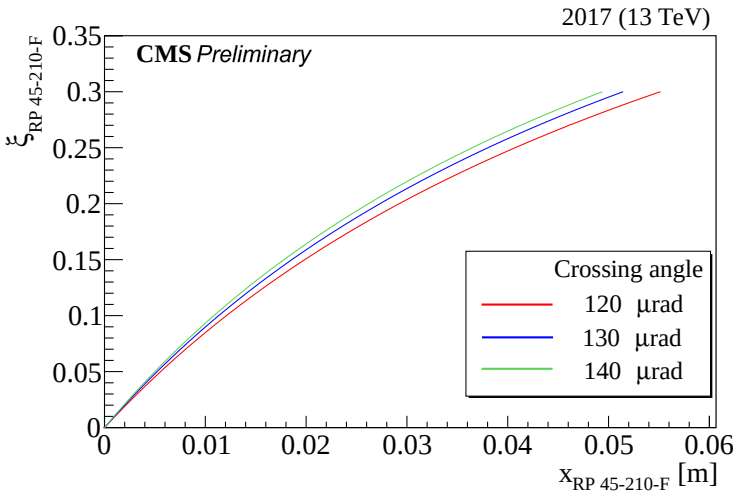

Figure 4.3: The horizontal dispersion function D_x translates the momentum loss ξ of the proton at IP5 to its position x at the Roman Pots. The dispersion function is ξ dependent itself and the figure shows directly the obtained non-linear $x(\xi) = D(\xi) \cdot \xi$ function. The $x(\xi)$ function depends on the crossing angle as well; the figure shows the dependence for three reference angles, which permits to interpolate the function to arbitrary intermediate angles [2].

4.2 Alignment

The alignment of PPS detectors is a complex multi-step procedure that includes aligning detector planes among themselves and RPs with respect to the LHC beam.

Since RPs are movable objects, and the fill-to-fill beam position reproducibility has limited accuracy, some of the alignment parameters need to be re-computed for each LHC fill. The relative position of the RPs with respect to the beam needs to be re-calibrated after each insertion, while the alignment among detector planes in the same station will remain constant until detector replacement operations occur.

The same technique determines the relative alignment among sensor planes in the RPs and between the two RPs in the same arm. Residuals between hits and fitted tracks are minimised in an iterative procedure, which is needed because large residuals due to misalignments are in principle impossible to distinguish from outliers generated by, e.g., detector

noise. The alignment procedure starts therefore with large tolerances $\mathcal{O}(100\ \mu\text{m})$ to accommodate misalignments which, as progressive alignment corrections are applied, are decreased down to $\mathcal{O}(10\ \mu\text{m})$. The typical uncertainty of the relative RP alignment is a few micrometres.

These alignment constants are derived on dedicated datasets, the so-called *alignment fills*. In these fills, the LHC settings are identical to the ones used during standard data-taking (*physics fills*), although lower beam intensity is achieved by injecting a lower amount of bunches (typically two, with respect to the nominal 2500). This yields instantaneous luminosities four orders of magnitude lower with respect to the nominal $10^{34}\text{cm}^{-2}s^{-1}$, and average pileup ≈ 20 (in physics fills it ranges between 15 and 55).

The beam size at the RP locations is approximately $\sigma_{beam} = 0.1$ mm horizontally and $\sigma_{beam} = 0.4$ mm vertically. While during physics fills safety rules allow RP insertions down to a distance of about $15\sigma_{beam}$, in alignment ones PPS is allowed to approach the LHC beam much closer, thanks to the reduced intensity: typically $6.5\sigma_{beam}$ horizontally and $5\sigma_{beam}$ vertically. Such proximity to the beam grants an overlap between the horizontal and vertical stations, as shown in Figure 4.4a, which allows for their relative alignment to be measured.

The absolute position of the beam is instead measured by exploiting the kinematics of protons undergoing elastic scattering, i.e. a process with only two protons in the final state, each having $\xi = 0$ as a consequence of the momentum conservation. Such protons depart from the same vertex with opposite directions and are easy to tag (Section 5.2.1 in Ref. [95]). Their azimuthal symmetry at the IP, propagated by the LHC optics, distributes them elliptically on the transverse plane at the RP locations. Their distribution can be used to extract the precise beam location as shown in Figure 4.4b: the horizontal profile (average along the x axis) is interpolated between the top and bottom RPs, providing information on horizontal alignment and potential rotations in the xy plane.

This information is combined with a minimum bias sample (protons due to pileup, unrelated to any trigger) in the horizontal RP. The vertical

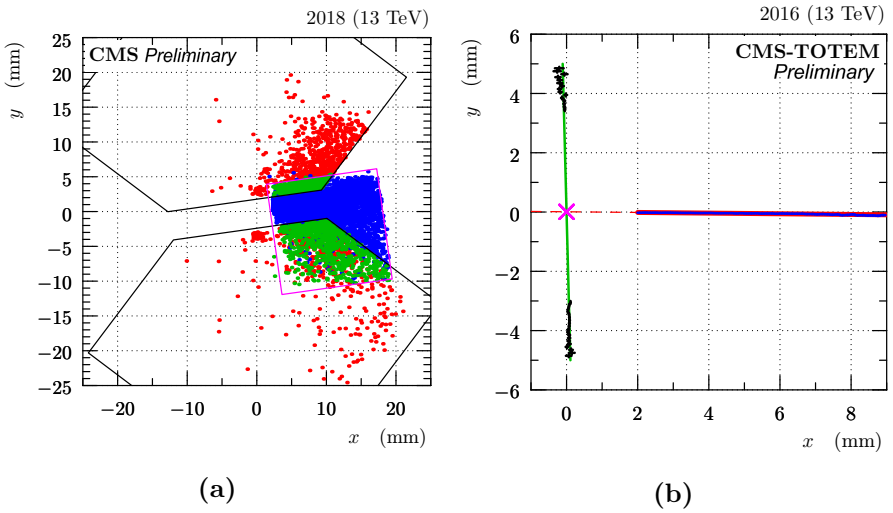

(a) (b)

Figure 4.4: (a): relative alignment between vertical and horizontal RPs (April 2018). The plot shows track impact points in a scoring plane perpendicular to the beam. The points in red represent tracks only reconstructed from vertical RPs, in blue only from horizontal RPs and in green from both vertical and horizontal RPs. The size and position of the RP sensors is schematically indicated by the black (vertical strip RPs) and magenta (horizontal pixel RPs) contours.
(b): determination of the beam position with respect to RPs (September 2016). Black: profile (mean x as a function of y) of elastic track impact points observed in vertical RPs; green: fit and interpolation. Blue: horizontal profile of minimum bias tracks found in the horizontal RP; red: fit and extrapolation. Magenta cross: the determined beam position [2].

profile of the proton distribution is interpolated with a straight line, and the intersection between the two fitted lines corresponds to the beam position, which is determined with a typical uncertainty of about 10 μm.

After each insertion of horizontal RPs during physics fills, corrections on the absolute and relative alignments between stations are derived. The horizontal absolute alignment correction is based on matching $S(x)$, the slope of the $y_F - y_N$ [2] dependence on y as a function of x (Fig. 4.5), by shifting along the x axis the curve measured in the physics fill until the best fit with the one observed in the reference alignment fill is found (Fig.

[2] F and N pedices indicate the far and near stations of the same arm with respect to the IP.

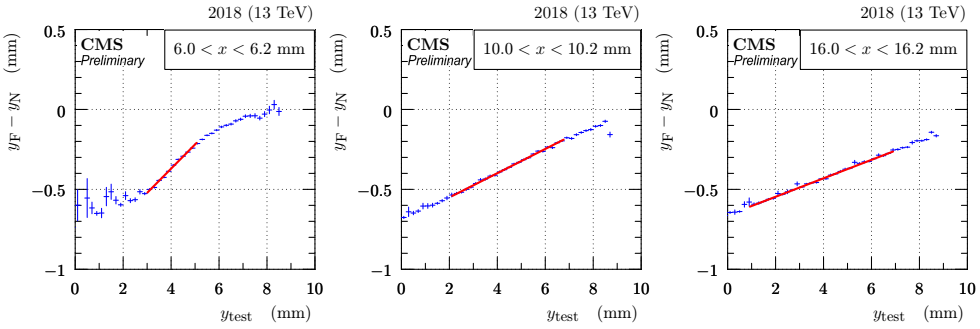

Figure 4.5: Illustration of $y_{\mathrm{F}} - y_{\mathrm{N}}$ dependence on the vertical coordinate of the RP being aligned y_{test} (fill 7139, 2018 and RP 56-210-fr is shown here). The three plots correspond to three x selections as indicated in the legends. Blue: profile histogram of the dependence, red: linear fit in the central part [2].

4.6a). The shift measures the beam absolute horizontal position in each fill.

Finer near-far station horizontal corrections (Fig. 4.6b) are derived by extrapolating the distribution of $x_F - x_N$ versus x_N to the absolute beam position found with the method shown in Figure 4.6a.

Finally, the vertical absolute alignment correction is derived by fitting the mode of y as a function of x with a straight line. The correction is found by evaluating the fitted line at the beam x coordinate found as in Figure 4.6a. The procedure is illustrated in Figure 4.7.

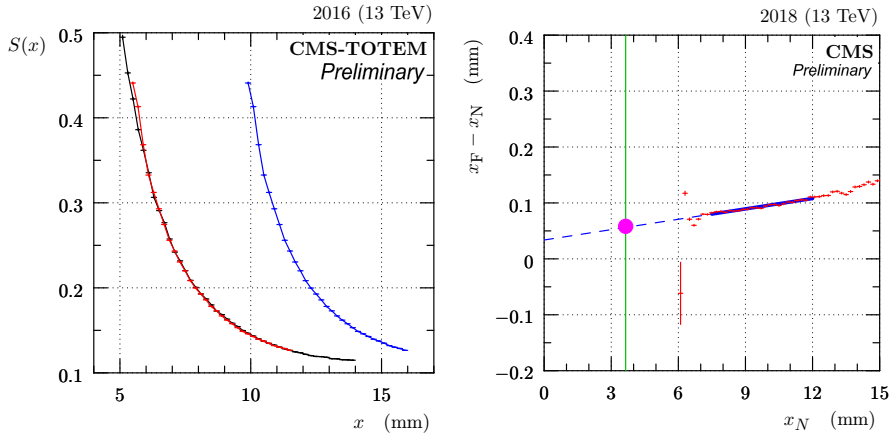

(a) **(b)**

Figure 4.6: (a): illustration of absolute horizontal alignment (fill 5424, 2016 post-TS2 and RP 45-210-fr). Black: data from reference "alignment" fill, blue: data from a physics fill before alignment and red: data from the physics fill, aligned to match with the black reference.
(b): illustration of horizontal near-far relative alignment (fill 7052, 2018 and sector 45). Red: mean value of $x_F - x_N$ as function of x_N. Blue: fit and extrapolation to the horizontal beam position (vertical green line, e.g. from the left plot). The value of the correction is indicated by the magenta dot [2].

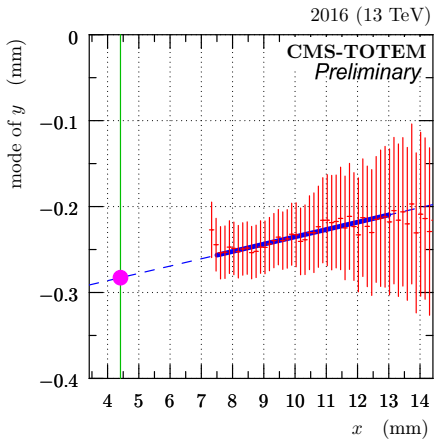

Figure 4.7: Illustration of vertical alignment (fill 5424, 2016 post-TS2 and RP 45-210-fr). Red: mode (most frequent value) of y as a function of x, Blue: fit and extrapolation to the horizontal beam position (indicated by the vertical green line and extracted from Figure 4.6a, left). The value of the vertical alignment correction is indicated by the magenta dot. The error bars represent systematic uncertainty [2].

4.3 Proton reconstruction

The proton reconstruction consists in transforming the measurement of the proton kinematics at the RP location $\mathbf{d}(s)$ in their counterparts at the IP, i.e. $\mathbf{d}^*$ (cf. Eq. 4.2). The back-propagation follows the LHC optics presented in Section 4.1 and its inputs are the four independent track parameters: the intersections with a scoring plane, and the horizontal and vertical angles with respect to the beam (z axis).

Two complementary reconstruction strategies are employed: single-RP and multi-RP.

The former is a simple approach used when tracks are reconstructed with information from only one RP. In this case, tracking detectors cannot provide a valuable measurement of the tracks angle because of their limited resolution. Under these circumstances, only a partial reconstruction is performed, which reflects the leading terms in the optics decomposition in Eq. 4.4:

$$\xi = x_{\mathrm{d}}^{-1}(x) \ , \qquad \theta_y^* = \frac{y}{L_y(\xi)} \tag{4.11}$$

where ξ reconstructed from the first equation is substituted in the second. This method has lower resolution with respect to the multi-RP one because of the neglected terms. However, it allows reconstructing the proton even when the track is not available in the other RP of the arm. The variables y^* and θ_x^* that are not reconstructed are set to zero, as this is a reasonable approximation in low β^* optics.

The multi-RP reconstruction exploits the information from tracks measured in both RPs in the same arm. In this case, all four track parameters are available. The proton kinematics that best matches the observation is searched via χ^2 minimization:

$$\chi^2 = \sum_{i:\ \mathrm{RPs}} \sum_{q:\ x,y} \left[\frac{d_q^i - (T^i d^*)_q}{\sigma_q^i} \right]^2 \tag{4.12}$$

where i runs over the tracking RPs in the arm and q over the two trans-

verse projections, following the notation of Eq. 4.2. The matrix T^i stands for the proton transport between the IP and the i-th RP. The quantity σ_q^i denotes the position measurement uncertainty at the i-th RP in projection q.

Being $\mathbf{d}^*$ a five-dimensions vector, the reconstruction would be underconstrained unless one of the variables is fixed with external information. That is the case of x^*, which is by default set to zero because of the very narrow distributions of the interaction vertices in the transverse plane, which are of the order of 10 μm. Considering the effects given by optical functions, neglecting x^* does not significantly worsen the reconstruction accuracy. Despite being somewhat arbitrary, the choice of fixing x^* over y^* is justified by the fact that results are compatible when doing otherwise.

The multi-RP reconstruction relies on the assumption that its inputs, which are the tracks measured in the near and far RPs, belong to the same proton. That is especially relevant for 2017 and 2018 data, when pixel detectors allowed multiple protons to be reconstructed in the same RP.

Selection criteria are applied to ensure the proper track association (so-called *association cuts*). This also aims to disentangle tracks from multiple protons in the same event (only possible in 2018). The Δx, Δy, $\Delta\xi$ and $\Delta\theta_y^*$, where Δ indicates the near-far difference, should be small when when both tracks originate from the same proton. The distributions of these variables are thus studied to optimise the selection criteria for purity and efficiency, using both MC simulation and data.

The same track cannot be associated to more than one multi-RP proton. Tracks in the near RP that pass the association cuts with multiple tracks in the far RP are thus excluded from the reconstruction. In addition, once a track in the far RP is matched with one in the near, it is removed from further associations.

The optimisation of the cuts is performed separately for each year of data-taking and yields looser cuts for 2016 when multiple associations were not possible (strip detectors in both RPs). Instead, tighter cuts were applied for 2017 and 2018 to exploit the full potential of pixel detectors.

Figure 4.8 shows the difference between the ξs reconstructed at the two RP locations in the same arm versus the multi-RP ξ. The difference is centred in zero and its distribution does not vary with multi-RP ξ. That is expected when the alignment and optics calibration is correct. The phase space covered by the distribution is constrained at low ξ by how much tracking detectors can approach the beam and at high ξ by the upstream LHC collimator.

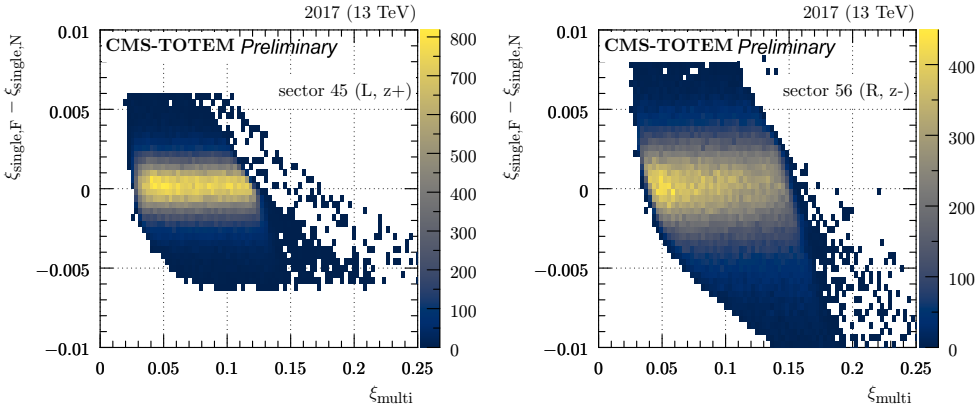

Figure 4.8: Difference of ξ reconstructed with the single-RP method from the near and far RP in each arm, as a function of multi-RP ξ (fill 5849, 2017). Left: sector 45, right: sector 56 [2].

The θ_x^* distribution reconstructed with the multi-RP technique is expected to be symmetrically distributed around zero, with no dependence on ξ. This matches with the observation illustrated in Figure 4.9. The same limits at low and high ξ mentioned above apply, and the sharp θ_x^*-dependent fall at high ξ is used to model the limitations created by the upstream LHC apertures empirically.

Horizontal slices of the 2D distribution (shown in Fig. 4.9) at constant θ_x^* are used to extract the ξ points of discontinuity (cf. green points in Fig. 4.10). These points are then fitted with a two-segment line in the form:

$$\theta_x^* = \theta_0 + a\,(\xi - \xi_0)\ , \qquad a = a_0 \text{ for } \xi < \xi_0 \text{ or } a_1 \text{ for } \xi \geq \xi_0 \tag{4.13}$$

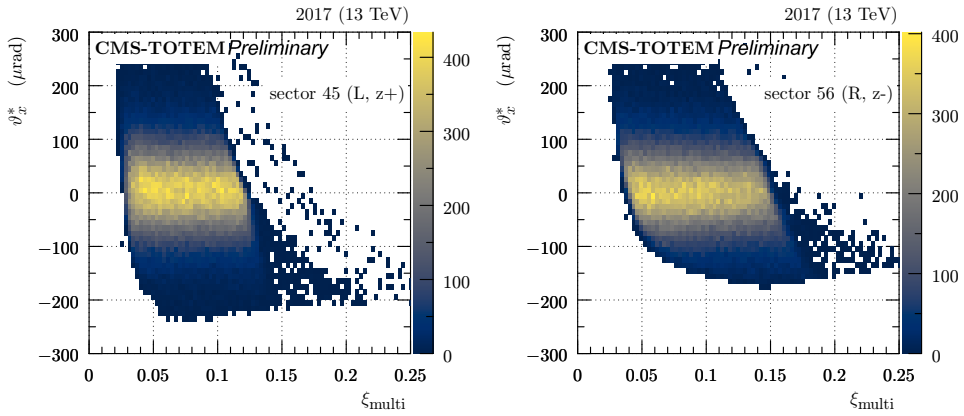

Figure 4.9: Histogram of θ_x^* vs. ξ as reconstructed with the multi-RP method (fill 5849, 2017). Left: sector 45, right: sector 56 [2].

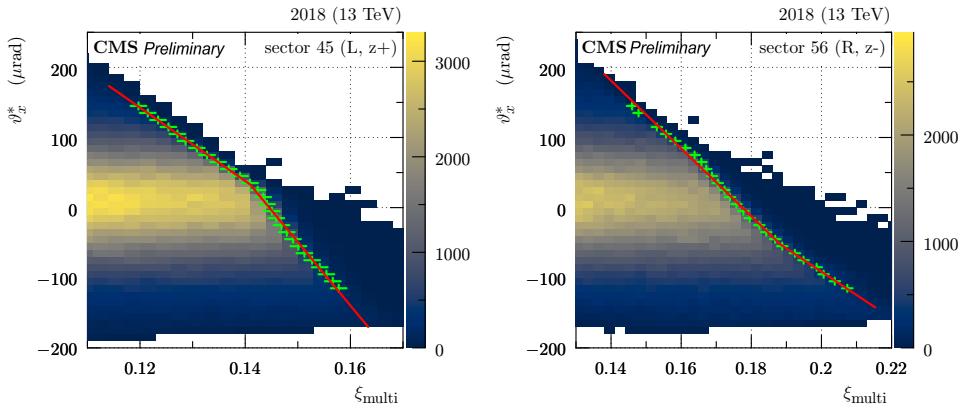

Figure 4.10: Distribution of θ_x^* vs. ξ reconstructed with the multi-RP method (fill 6617, 2018), zoomed at high ξ. The green markers represent the identified aperture cutoff, the red line the fit according to Eq. (4.13). Left: sector 45, right: sector 56 [2].

The slope of the two lines is given by the interplay of the horizontal dispersion and effective length at the limiting LHC element. The aperture limits are therefore determined for each crossing angle.

Finally, the fitted functions are used to parameterize the apertures and suppress spurious protons reconstructed in the region forbidden by the LHC collimator. These tracks are not compatible with protons coming from the IP and are either part of the beam halo or secondary particles generated by proton interactions in the beam pipe.

4.4 Proton simulation

PPS developed a fast simulation of forward proton propagation for detector and physics studies. Simulation details such as multiple scattering and particle interactions with the detector mechanical structure are neglected. The simulation accounts for:

- beam smearing at the IP: vertex smearing and beam divergence
- proton propagation to the RP position according to the LHC optics
- aperture limitations (as described in Section 4.3)
- geometrical detector acceptance
- digitisation: detector hits are created at the nearest strip/pixel
- detector efficiencies: efficiency maps extracted from data are used (this feature can be disabled in specific use cases)

The simulation can be run with a realistic distribution of relevant parameters such as β^*, crossing angle, optics, apertures, and RP positions.

The fast simulation output is a collection of detector hits, with a software structure identical to the one produced during data-taking when detector digital outputs are clustered into hits. Once the hit collection is generated, the PPS track and proton reconstruction software can be applied.

The source of protons for the simulation is up to the user. By default the simulation uses a particle gun that generates random protons with a uniform ξ distribution, and Gaussian θ_x^* and θ_y^* centered at zero with 60 μrad RMS.

Figure 4.11 shows a comparison between track positions from protons produced with the default generator and minimum-bias events in data (no explicit event/track selection). The track position is defined as the intersection between the track and a scoring plane at the nominal RP position. In the left plot, it is visible that the simulation reproduces well

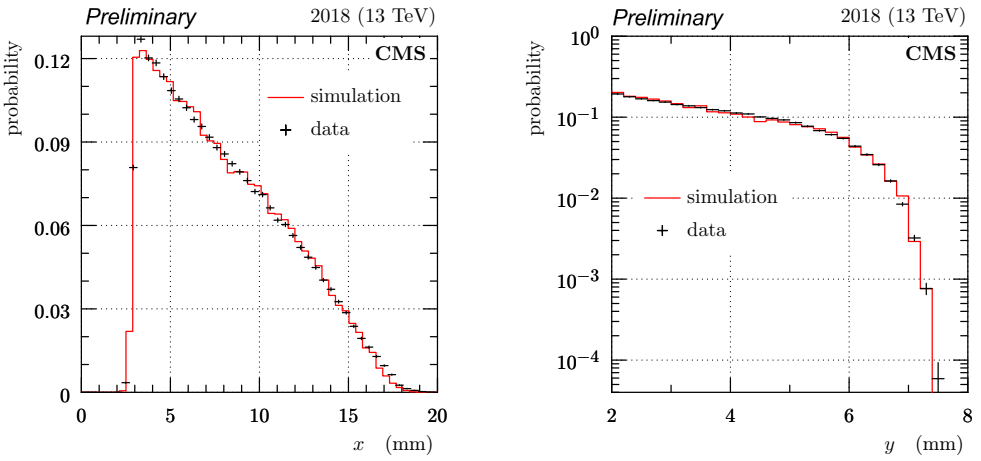

Figure 4.11: Comparison of track distributions from simulation (red) and LHC data (fill 6738, no explicit event/track selection, black), for 2018 pre-TS1 configuration, RP 56-210-fr. Left: distribution of horizontal track positions; right: distribution of vertical track positions (zoomed around the upper sensor edge) [2].

the sharp cutoff due to the sensor edge at low x and the smooth decrease at large x, caused by the upstream collimator. In the right histogram, a close-up of the upper region of the sensor is shown (cf. Fig. 3.16). Also in this case, the simulation describes well the sensor edge and agrees with the observed tracks.

The proton fast simulation also allows comparing the detector acceptance and performance throughout the years as a function of ξ. Figure 4.12 shows the effect of the interplay between optics and detector acceptance in Run 2. Results can be compared with Figure 4.16, where also detector efficiencies are taken into account.

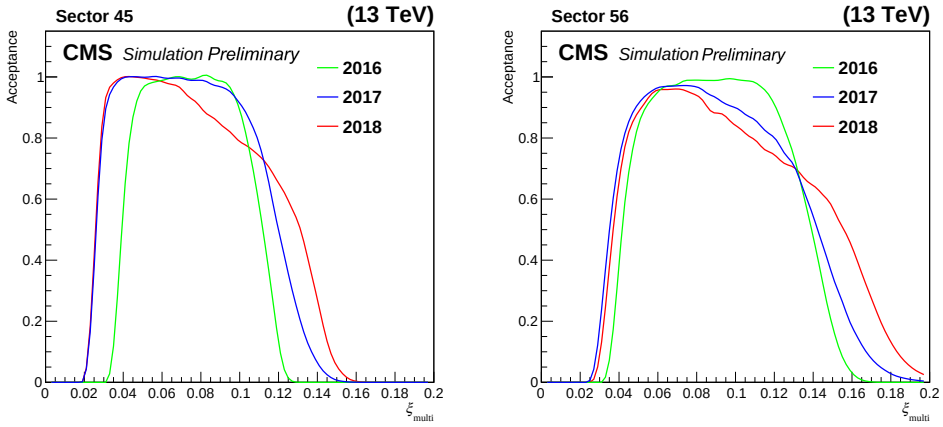

Figure 4.12: Fraction of reconstructed multi-RP protons, as a function of $\xi_{multiRP}$, for a proton sample produced with the PPS fast simulation. Only acceptance effects are taken into account [2].

4.5 Proton efficiency

The efficiency of the PPS tracking detector needs to be closely monitored, as radiation-induced effects can degrade the performance along the operation.

Multiple factors need to be taken into account: the efficiency of the detectors, the reconstruction algorithm efficiency, and the probability that the proton interacts with the material between the two tracking stations, and is lost.

PPS used multiple detector technologies during the data-taking, and the definition of the efficiency changes accordingly.

In 2016, with only strip detectors used, allowing only one proton track to be reconstructed in each station, the reconstruction algorithm efficiency is close to 100%, as loose association cuts can be used (cf. Section 4.3). The dominant role is played by detector effects, such as radiation damage and multi-tracking inefficiency. A more detailed description is given in Section 4.5.1.

In 2017 and 2018, pixel detectors could resolve multiple tracks in the same station, and a different approach for the efficiency estimation is

used. The reconstruction efficiency for multi-RP protons was split into two independent multiplicative factors: the efficiency of the "near" detector and the so-called multi-RP efficiency. The former takes into account only the detector-related effects for the "near" RP (strips in 2017 and pixels in 2018), while the latter accounts for detector-related efficiency in the "far" RP (pixels in both 2017 and 2018), the reconstruction algorithm efficiency, and the proton propagation.

The first factor, for strips, is derived as described in Section 4.5.1, while the method used for pixel detectors is presented in Section 3.3.2. The multi-RP efficiency is discussed in Section 4.5.2.

Efficiency corrections are computed for each RP and data-taking period separately.

4.5.1 Silicon strip detector efficiency

Two main sources of inefficiency affect the PPS strip detectors: radiation damage and the presence of multiple tracks in the same event. These effects have been studied separately and are described with two efficiency factors.

If more than one particle produces signal in the strip detectors, track candidates that do not correspond to a real particle, the so-called ghost tracks, are found. Because of this, strip detectors can only be used in events where one track is present [96]. Events with one or more protons in strip detectors show at least one track pattern in both strip orientations, or a hit multiplicity greater than the threshold set for the pattern-recognition algorithm to give up.

In minimum-bias samples, events with one or more protons in the strip detectors are selected. This is done by requiring either at least one track pattern in both strip orientations, or a number of detector hits greater than the maximum allowed by the pattern recognition algorithm, which is tuned to accept a single proton track with some tolerance for detector noise. The selected events are used to compute the efficiency factor, which is the ratio between the number of reconstructed tracks and the number

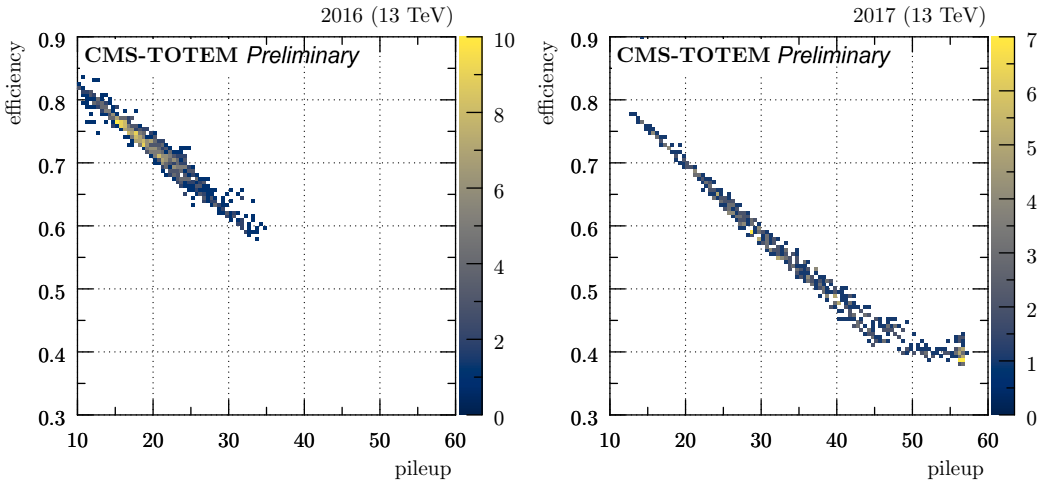

Figure 4.13: Strip multiple track efficiency factor versus pileup in RP 45-210-fr. Left: data-taking period between the first and the second 2016 Technical Stops. Right: data-taking period between the second and the third 2017 Technical Stops [2].

of selected events. This efficiency factor is inversely related to the pileup, and ranges between 40 and 80%. Consistent results are observed in both 2016 and 2017, and across different sectors, as illustrated in Figure 4.13.

The second factor takes into account the time-dependent decrease of the detector efficiency produced by radiation, and it has been studied with a tag-and-probe method [97]. The main cause for the decrease in the efficiency observed is the radiation damage in the silicon strip sensors. These devices, designed for lower radiation fluences in the context of the TOTEM experiment [98], suffered losses in their charge collection efficiency, thus losing performance.

In order to probe the efficiency of the strip detectors in one station, minimum-bias events with one reconstructed track in the other RP (tag) of the same arm, passing loose quality criteria, are selected.

Events with more than one recognized track pattern in the strip detector being probed are excluded, together with events with multiple tracks in the tag RP, with pixel detectors. A matching window of $|\Delta\xi| < 0.01$ is defined, where $\Delta\xi$ represents the difference between the single-RP ξ measurement associated with the track in the tag RP, and the measurement

in the RP being probed, if a track is detected.

The efficiency correction factor is defined as the ratio between the number of events in which a strips track satisfies this matching criterion, and the total number of events selected. Statistical uncertainties have been found negligible, and two sources of systematic uncertainty have been evaluated. A 1% uncertainty is associated to the choice of the minimum-bias sample used for the estimation; an uncertainty of the same size is associated to the variation of the quality criteria applied to the tagging track. A larger (10%) conservative systematic uncertainty is applied to 2016 efficiency factors because a different method is used. Efficiencies are derived by comparing ξ distributions in data with respect to the ones observed in the alignment fill, when the detectors had not suffered any radiation damage yet. The uncertainty is estimated by comparing with results obtained with the tag-and-probe method.

Figure 4.14 shows the results as a function of the x–y global coordinates of the track measured in the tagging RP, for the region covered by the detector acceptance and below the collimator aperture limits. The area damaged by radiation is clearly visible and its size and inefficiency grows with the integrated luminosity. However, values higher than 95% are consistently found in the efficiency plateau region. Similar results are observed in the 2016 data, although the lower collected integrated luminosity reduced radiation effects.

Data-taking periods in which strips detectors were not inserted or operational are excluded from the presented results. They mainly affect the last period of 2017 (bottom-right plot of Fig. 4.14), where they account for $\approx 10\%$ efficiency loss.

In 2016, the correlation between inefficiency factors caused by the presence of multiple tracks in strip detectors in the "near" and "far" RPs in the same sector has been measured between 50% and 80%. The complete tracking inefficiency can therefore be computed as the product of the following factors: the multiple tracks inefficiencies (taking into account their correlation), the radiation damage inefficiency for both the "near" and "far" station, and the proton interaction probability. The

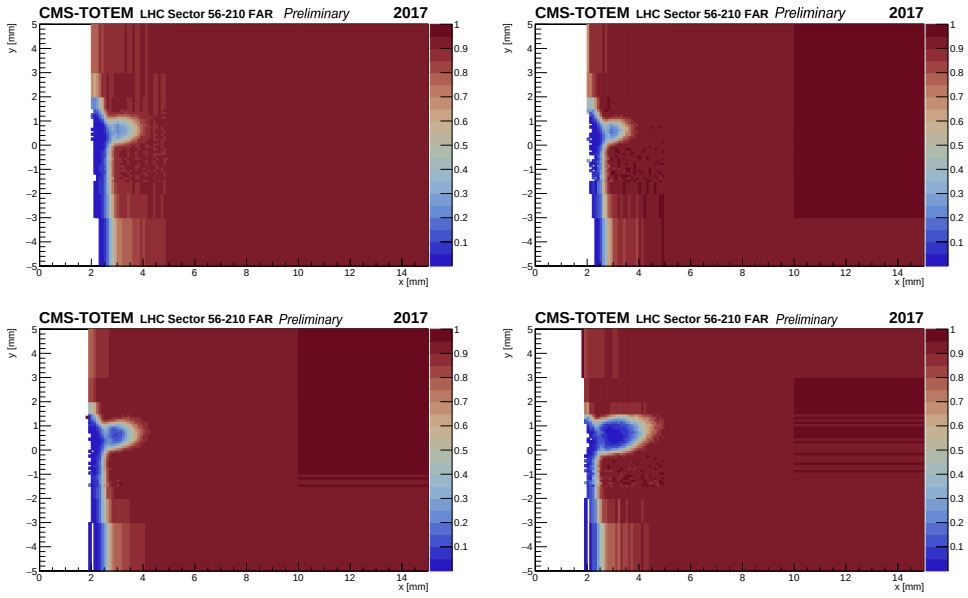

Figure 4.14: Strip detector tracking efficiency corrections for radiation effects, computed with data collected in 2017, over different consecutive data-taking periods. The figure shows the results for the RP 56-210-fr, as a function of the x–y global coordinates of the track measured in the tagging RP 56-220-fr, for different periods. Each period is defined as an interval in integrated luminosity computed since the detector installation.
Top left: L_{INT} = 0–9 fb^{-1}. Top right: L_{INT} = 9–10.7 fb^{-1}. Bottom left: L_{INT} = 10.7–18.5 fb^{-1}. Bottom right: L_{INT} = 18.5–22.2 fb^{-1} [2].

latter has been measured by the TOTEM experiment to be approximately 2% [99].

4.5.2 Multi-RP efficiency

The multi-RP efficiency factor is evaluated in the same way in 2017 and 2018, and takes into account the efficiency of the detectors installed in the 220-fr RPs, the efficiency of the multi-RP reconstruction algorithm, and the probability that a proton propagates from the 210-fr RPs to the 220-fr without interacting. These multiple components are evaluated together using a tag-and-probe method. For each data-taking period, minimum-bias samples have been selected for this purpose. Each single-RP proton reconstructed with the 210-fr RPs is used as tag, provided that its track

angle measured with that tracking station is lower than 20 mrad. This selection excludes very inclined background tracks that do not originate from the interaction point.

The efficiency is evaluated as the ratio between the number of times in which a multi-RP proton is reconstructed using the single-RP tag proton, and the number of tag protons. The systematic uncertainties related to the sample choice for the efficiency estimation are $\approx 1\%$. Asymmetric statistical uncertainties are evaluated with the Clopper-Pearson frequentist approach [100]. This method allows to define a confidence interval with a slightly conservative coverage, which accurately takes into account the binomial behaviour of the efficiency as a random variable.

The efficiency is plotted in Fig. 4.15 as a function of the x–y global coordinates of the 210-fr RP scoring plane. The overlap between the acceptances of the RPs in the same sector, combined with the collimator aperture limits, defines the shape of the efficiency map.

This efficiency has generally a plateau value higher than 90% in 2017, and slightly lower in 2018. These high values reflect the good performance of the detectors and of the reconstruction algorithm. Lower performance can be observed in the most irradiated region because of radiation damage and multiple tracks. The latter takes place when more than one track in the 220-fr RP satisfies the association requirements with the 210-fr RP track. Under these circumstances the multi-RP reconstruction cannot choose between the 220-fr RP tracks and fails, causing inefficiency.

Consistent results are observed in 2017 and 2018 when restricting the analysis to events with a single track in the 210-fr RP. A small loss in the performance of the 2018 multi-RP reconstruction algorithm is observed when including events with multiple tracks in the "near" station, because of the higher multiple-match probability, as mentioned above.

Figure 4.16 shows the fraction of reconstructed multi-RP protons predicted by the fast simulation, taking into account both efficiency and acceptance effects. The difference in the shape of the plots for the three years is mainly due to the different acceptance (cf. Fig. 4.12). The higher value of the fraction is 2018 reflects the presence of the pixel detectors in

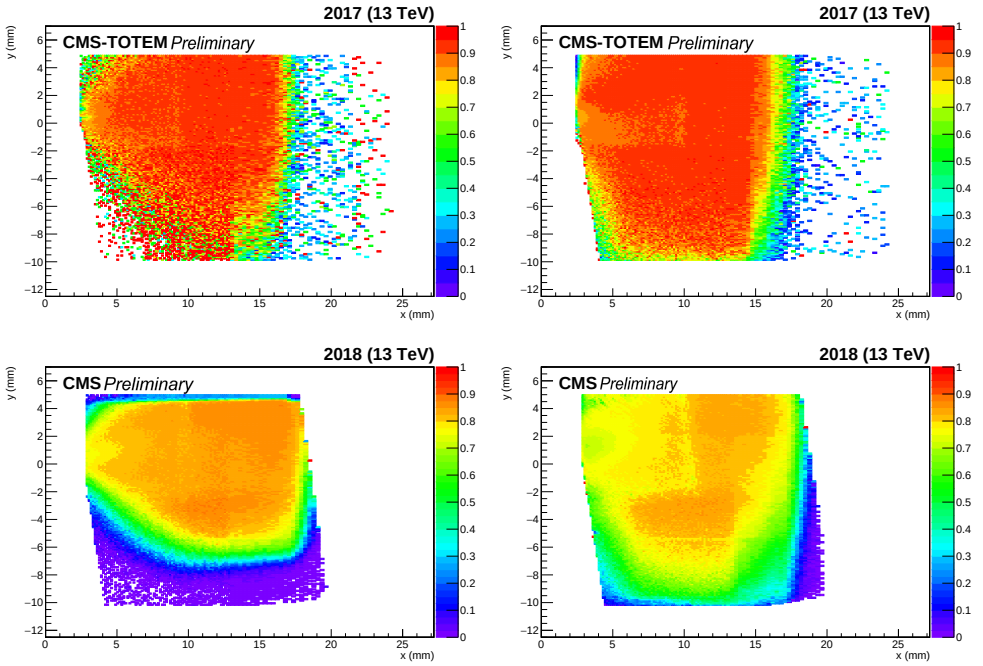

Figure 4.15: multi-RP efficiency factor that includes the efficiency of the detectors installed in the 220-fr RPs, the efficiency of the multi-RP reconstruction algorithm, and the probability that a proton propagates from the 210-fr RPs to the 220-fr without interacting, shown as a function of the global x–y coordinates. Top: multi-RP efficiency in sector 45 (left) and 56 (right) at the beginning of the 2017 data-taking. Bottom: multi-RP efficiency in in sector 45 (left) and 56 (right) at the beginning of the 2018 data-taking [2].

both RP stations.

The difference between the 2016 and 2017 performance is caused by multiple factors: the average pileup in 2017 was significantly higher than in 2016, producing a higher strip multi-tracking inefficiency (Fig. 4.13). The luminosity collected in 2016 was about one fourth than in 2017, making radiation damage less severe. Furthermore, the 45-210-fr RP was not available for a significant portion of 2017 ($\approx$ 24% of the whole data-taking), thus effectively lowering the overall efficiency, as downtime is included as an inefficiency component. The effect of each efficiency component is also shown in Fig. 4.17.

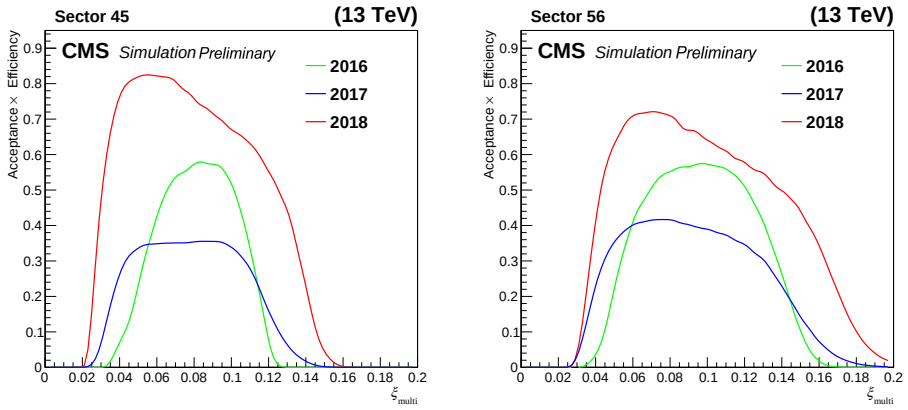

Figure 4.16: Fraction of reconstructed multi-RP protons, as a function of ξ_{multi}, for a proton sample produced with the PPS fast simulation. Acceptance and efficiency effects are taken into account. The left and right plots show results for sector 45 and 56, respectively. The efficiency systematic uncertainties, computed combining in quadrature the systematics estimated for each efficiency factor, are 10%, 2.7%, and 2.1% for 2016, 2017, and 2018, respectively [2].

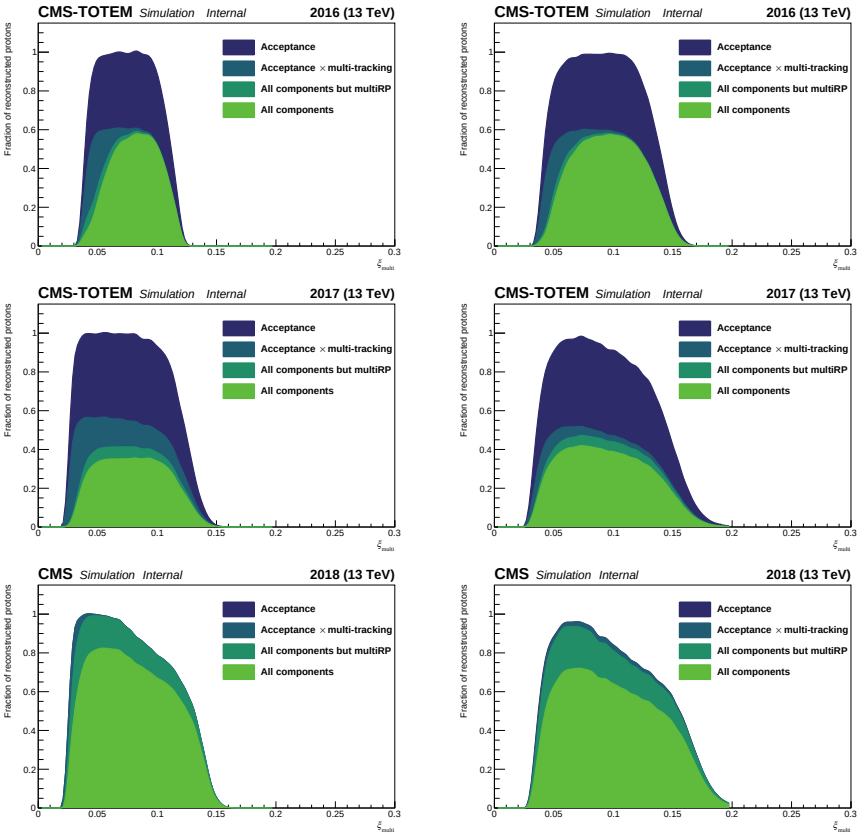

Figure 4.17: Fraction of reconstructed multi-RP protons, as a function of ξ_{multi}, for a proton sample produced with the PPS fast simulation. On the left(right), distributions for sector 45(56) are shown. The histograms show, from darkest to lightest, the effect of: acceptance only; acceptance and strips multi-tracking inefficiency; acceptance, strips multi-tracking inefficiency, and near RP detection efficiency; all components. The plots on the third line show that the 2018 efficiency is higher mainly as consequence of the multi-tracking capability of pixel detectors.

Chapter 5

Run 3 PPS pixel tracker

During Run 3, the LHC is foreseen to deliver between 190 and 270 fb^{-1} of 13.6 TeV data with a leveled luminosity of $2 \cdot 10^{34}$ $cm^{-2}s^{-1}$. At the time of writing this thesis, because of the ongoing COVID-19 pandemic, the duration of Run 3 is still under discussion, and this will affect the effective integrated luminosity.

The PPS Run 3 tracker was designed to withstand about 200 fb^{-1}. However, in case of performance degradation due to excessive irradiation, it will be possible to replace detector planes with spare parts during short tunnel access.

In the present chapter, the preparation of the PPS Run 3 tracking detector is described.

The first section focuses on the differences with respect to the Run 2 setup.

The second section illustrates the detector movement system implemented to withstand the integrated luminosity foreseen in Run 3, its mechanical implementation, installation and control software.

The third section describes the qualification and calibration of the new detector modules that will be installed for data-taking.

The fourth section focuses on the so-called *rolling calibrations*, which are a tool developed for the Run 3 data-taking that will allow high-level detector calibrations to be performed during operation.

5.1 Detector apparatus

The design of the Run 3 PPS pixel tracker is strongly derived from its Run 2 version.

The same stations used during Run 2 are being re-equipped in these first months of 2022 with new detectors. Each station houses six planes of a new version of 3D pixel silicon sensors. They are read out with the PROC600v4 chip, and the TBM is updated to a new version to maintain compatibility with the readout chip.

The mechanics of the detector package was re-designed entirely to accommodate a linear actuator mount. The motor allows for vertical movements of the whole detector package inside the RP box, a strategy that was proven helpful in Run 2 (Fig. 3.21). This new addition to the package enables remote movements without physical access to the RPs and largely increases the movement range.

To achieve that, the size of the aluminium plaquettes, to which the flex hybrids are glued, was decreased. The flex hybrid was completely re-designed, a necessity driven by the change of the TBM version.

5.1.1 PPS 3D pixel sensors

In 2021, thirteen 6-inches wafers of 3D pixel silicon sensors were produced by Fondazione Bruno Kessler (FBK). Each wafer (layout shown in Fig. 5.1) contained 36 sensors of size compatible with a 2×2 readout chip matrix (details about the PROC600 chip are presented in Section 5.1.2). In Run 2, the sensor portion furthest from the LHC beam (covered by two ROCs) often fell out of acceptance. This led to the decision of reducing the sensor size (Fig. 5.3a). Furthermore, the 2×2 sensor size matched the photolithography "cell" dimension of the implantation machine, making the production less error-prone and thus increasing its yield.

The wafers used for the production are 150μm-thick p-type (FZ) high resistivity substrates, directly bonded to 220 μm-thick p-type low-resistivity (CZ) handle wafers.

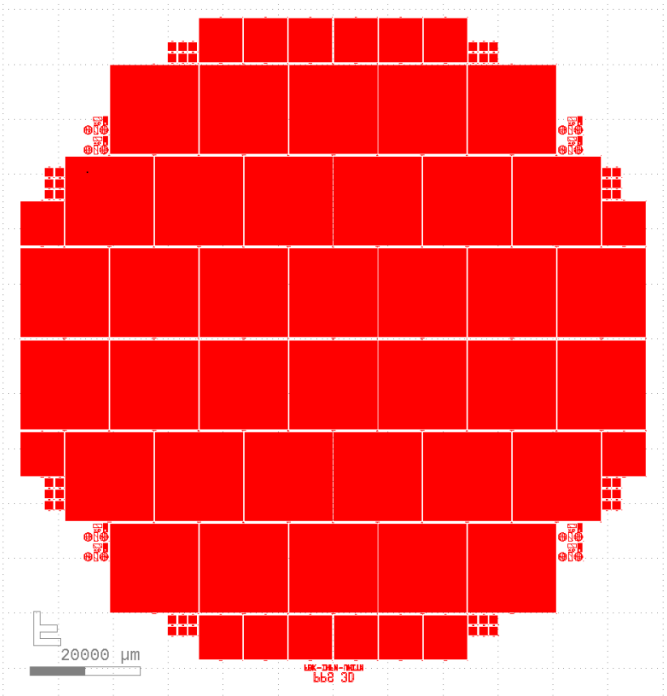

Figure 5.1: Wafer layout for the PPS Run 3 pixel sensor production. The larger rectangles indicate 2×2-sized sensors, while smaller ones are 1×1 sensors (not used in the PPS system) and test structures.

Although sharing the same pixel size (150×100 μm^2) with their Run 2 counterpart, the new sensors differ in many other aspects. First of all, FBK produced the sensors with a process developed in the context of the INFN-FBK R&D program [101] for the new ATLAS and CMS trackers for "Phase 2" (HL-LHC). It consists in etching and doping the electrodes of both types from the same active sensor side (so-called *single-sided* process).

The 5 μm-diameter junction columns of doping type n are shorter and connected to bump-bonding pads, whereas p-type ohmic columns of identical diameter traverse the active layer and reach into the handle wafer on the other sensor side. The handle wafer is later thinned down, reaching a 220 μm total sensor thickness, and a metal contact is deposited, providing electrical contact for reverse-biasing the sensor. Figure 5.2 shows the resulting cross-section.

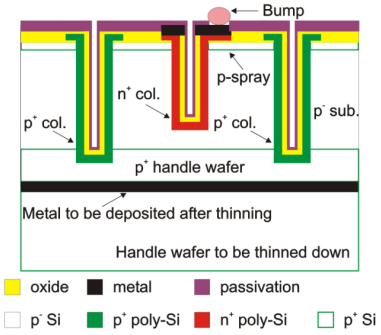

Figure 5.2: Schematic cross-section of the PPS Run 3 sensors. Reproduced from [79].

Electrodes are etched in the 2E geometry also used for some Run 2 sensors (Section 3.1). The size of pixels along ROC edges is doubled, as illustrated by Figure 5.3b, in order to fit the ROC chips.

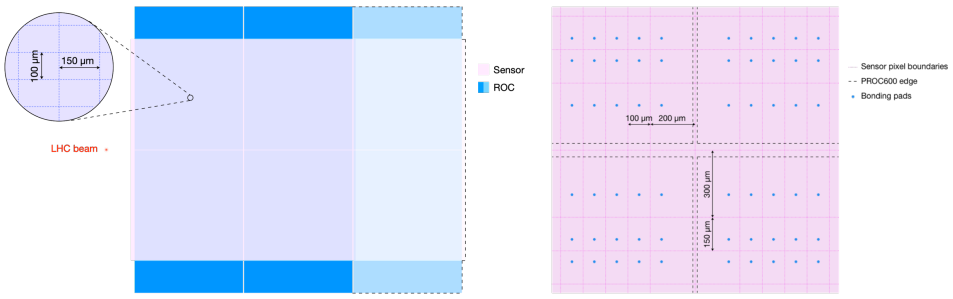

(a) **(b)**

Figure 5.3: Schematic representations of PPS Run 3 sensors. (a) shows the difference in size between Run 2 and Run 3 sensors. (b) shows the geometry of pixels at the edges between ROCs.

Each sensor needs to meet the following specifications to be considered fit for usage:

- Depletion voltage $V_{depl} < 10$ V
- Breakdown voltage $V_{bd} > 50$ V
- $[I(x + 2\text{ V})/I(x)] < 2$

where V_{depl} is the depletion voltage, measured with Capacitance-Voltage measurements. Current-Voltage (IV) characteristics are measured for

each sensor after applying a temporary metallization. That allows to measure the breakdown voltage and verify that the third specification is met. The latter prevents sharp current increases while increasing the bias voltage in the range below the breakdown. 2×2 sensors were classified based on their leakage current at room temperature and operation voltage V_{op}, where $V_{op} = V_{depl} + 20$ V:

- Wafer bow < 200 μm
- Class A: $I(V_{op}) < 16$ μA
- Class B: 16 μA $< I(V_{op}) < 40$ μA
- Class C: $I(V_{op}) > 40$ μA

Out of the 2×2 468 sensors produced, 238 passed all the requirements (50.9%), all of them belonging to the Class A category. The three highest yield wafers were sent for bump-bonding at the IZM (Fraunhofer-Institut für Zuverlässigkeit und Mikrointegration), and the first production of 40 units was issued, followed by a second for another 20.

5.1.2 PROC600v4 readout chip

In Run 3, the PPS 3D pixel sensors will be read out by PROC600v4 chips (PSI ROC for 600 MHz/cm^2, version 4) [102], arranged in a 2×2 matrix. Originally designed for the Phase I Upgrade of the CMS pixel project [103] in 250 nm CMOS technology, numerous spare units remained available after the tracker installation. That drove the choice of changing the PPS front-end readout to PROC600s, which are interchangeable with PSI46dig chips for the PPS tracker purposes.

The PROC600 was designed to sustain up to a 580 MHz/cm^2 pixel hit rate, the maximum foreseen by MC simulations for the layer 1 of the CMS tracker and much higher than the maximum 120 MHz/cm^2 observed in the layer 2 with PSI46dig chips. In order to achieve this, a new double column readout architecture was needed to maintain acceptable hit efficiency. The

column digital readout represents the major change with respect to the PSI46dig chip, whereas pixel unit cells and most of the chip periphery (containing DACs, readout buffer and ADC) are substantially identical. The PROC600 and PSI46dig share the same pixel array dimension (52 columns and 80 rows) and size (150×100 μm^2).

In the PSI46dig, the column drain happens by reading sequentially all the pixels that have detected a hit. Instead, the PROC600 reads out double-columns in 2×2 pixel clusters. The cluster location is dynamically adjusted along the column depending on the position of the hits, i.e. the grouping of pixels in clusters is not fixed, but varies event by event. Even if the cluster is not fully occupied, the pulse shape detected by all its pixels is transferred to the periphery, together with the cluster address. Pixels not containing hits are then zero-suppressed in the output. This is the so-called Dynamic Cluster Column Drain (DCCD) mechanism. Its main purpose is to allow the CMS layer 1 tracker to profit from the usual presence of 2×2 clusters when running at high rates. Under these circumstances, the mean number of clusters is about 1.2. The readout of the 2×2 cluster takes the same amount of time as the single-pixel readout in the PSI46dig, yielding a 2.4 gain in speed.

Another relevant difference between the two chips is the data output format. While the size of data words is identical, their meaning slightly differs. The PSI46dig encodes the hit address by transmitting the double column number and a second identifier which runs over the 160 pixels in the double column. The PROC600 instead transmits the hit row and column numbers.

The effects of non-uniform irradiation on the PROC600 are expected to be similar to what has been observed with PSI46dig, as they share the same CMOS technology and have common front-end amplifier characteristics.

5.1.3 Flex hybrid

A drastic change in the flex hybrid geometry took place for Run 3. The circuit was re-shaped in order to fit on the back-side of the sensor. The circuit is glued to the back-side of the sensor, while ROCs are attached to the 0.9 mm-thick aluminium plaquettes. The plaquette, 2.3 mm shorter than its Run 2 counterpart, together with the reduced flex circuit size, provides the essential tolerance needed for the vertical movement to occur.

The material traversed by protons is, in order: 0.4 mm of aluminium (the area covered by the sensore is thinner than the one around it), the PROC600 chips (180 μm-thick), the silicon sensor itself (220 μm), and the flex circuit (445 μm-thick).

Further changes in the flex circuit were also needed to adjust lines and pads in order to be compatible with PROC600 chips and the new TBM10d [104] version, necessary for the PROC600 readout. The TBM10d working principles are identical to those of the TBM08, used in Run2, however its internal structure differs. Within the TBM10d package, two TBM08 units are present (two cores each, Section 3.1.3). Data output lines are also doubled, therefore the maximum data throughput capability increases by a factor two.

This is a necessary feature for the CMS layer 1 tracker, where two ROCs are connected to each TBM08 core (thus 8 ROCs are read out by each TBM10d chip). A single TBM08 chip would not be able to provide enough data transfer rate for all the ROCs.

In the PPS case, instead, this feature is not needed, and the four ROCs are connected to the TBM08 cores in one TBM08 unit, while the other unit is left unused. The ROC readout order, in the TBM token ring, is similar to the one used in Run 2: maintaining the same numbering (shown in Fig. 5.4), one ring reads first ROC 0 and then ROC 1, while the other goes, in order, through ROC 4 and ROC 5.

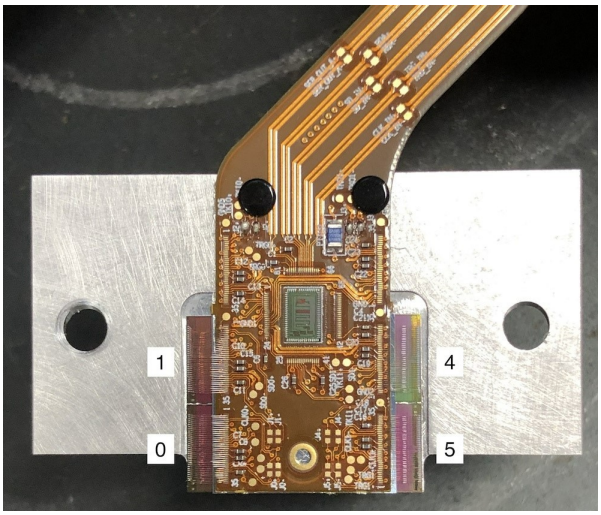

Figure 5.4: Close-up picture of the Run 3 flex hybrid. Numbers denote ROC identifiers.

5.1.4 Detector package

The detector package mechanics was wholly re-designed for Run 3. Besides the cooling capillaries and top spring mount, every other part was adapted to allow for movement and to accommodate the motor.

The moving part of the package (bottom of Fig. 5.6a) is pressure-fitted on two hard plastic rails on the top, which guide its movement. A commercial compact linear actuator (Zaber LAC10A-T4A [105] shown in Fig. 5.5) is mounted to the rear aluminium side panel (black component in the top-left of Fig. 5.6a). It is mechanically coupled to the left aluminium wall via a precisely machined steel cup that matches the shape of the motor tip. Springs on the right side (not visible in the figure) provide the force needed to keep the package in place and return to the initial position when the motor retracts.

The Zaber motor in use can produce a 40 N force in its 10 mm range, which is more than sufficient since the nominal movement range of the detector package is between 5.2 and 5.7 mm. Furthermore, the small size of the linear actuator, together with its nominal 0.024 μm movement resolution, make it ideal for the PPS tracker needs.

Figure 5.5: Picture of the Zaber LAC10A-T4A linear actuator.

A linear motion potentiometer (Bourns 3048 model [106]) is also mounted below the motor (blue component in Fig. 5.6c). The resistance between its cursor and one of the reference electrodes varies linearly in the 0–10 kΩ range with the position of its shaft, which has a half-inch range (12.7 mm). The potentiometer provides a second position measurement, independent of the motor.

Redundant position measurement is essential for the motor operation, as the linear actuator can only attempt precise movements but is not equipped with a feedback mechanism. This implies that if the actuator, which is a stepping motor, came across an obstacle that does not allow some steps to be performed, it would not be able to detect it and thus would not reach the desired position. The presence of a second position measurement solves this ambiguity.

Multiple contact points with the RP walls are provided by steel ball supports mounted on the aluminium side panels of the detector package (the four contacts near the bolts in Fig. 5.6c). A similar solution is also used on the bottom panel of the package, with three points of contact provided by precisely calibrated (larger) ball spacers, which define the distance of the sensors from the thin window.

The modules are inserted in their slots at the bottom of the package and kept in place by dowel pins. Even if only six will be equipped with modules, eight module slots are available for future developments. The slots are machined in an inclined fashion in order to form a 20° angle between the sensor planes and the plane orthogonal to the LHC beam. This is a slight change with respect to the 18.4° inclination in Run 2,

which will increase the charge sharing among pixels.

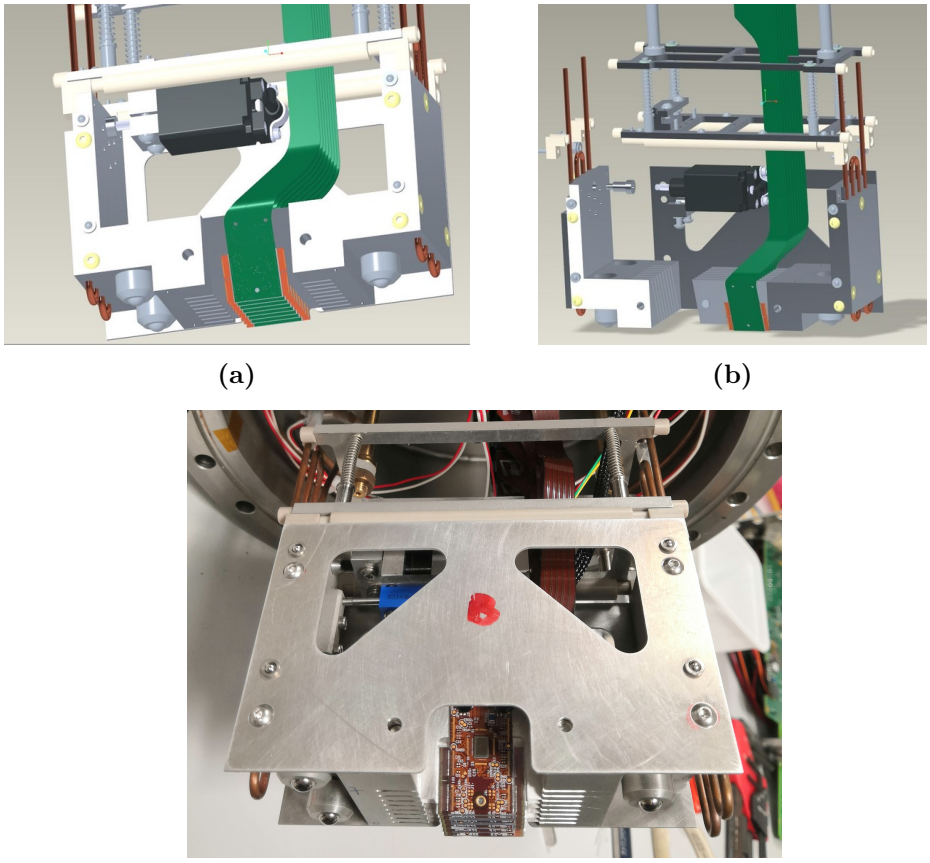

Figure 5.6: (a): side view of the Run 3 pixel detector package CAD model. (b): exploded view of the detector package CAD model. The linear actuator is visible at the top. The position sensor (potentiometer) and front aluminium side panel, which would cover the motor, are not shown. (c): picture of the first assembled detector package. The position sensor is visible below the linear actuator (blue component) and the side panel is mounted.

5.1.5 Portcard and DAQ

The Run 3 revision of the portcard shares almost all of its component with the one used in Run 2 data-taking (Section 3.1.4).

The main addition to the board is the support for two additional detector planes. Connection interfaces identical to the ones used for pixel planes are also available for the two additional ones. However, limited connectivity to the rest of the board components (control chips etc.) is provided.

This design choice aims to leave the board open to many possible implementations for future developments without imposing the same control and readout electronics on devices installed in the two spare slots. Their connectors are routed outside the board portion that sits in vacuum and left unplugged. Given the available space in the portcard housing in ambient temperature, such connectors will provide an interface for mezzanines that will implement the readout and control electronics of the two additional planes and remain within that same housing.

Another update introduced in the Run 3 revision of the portcard is the usage of POH4 opto-hybrids instead of POH7. Mainly driven by the extremely limited availability of POH7s, with respect to the high amounts of POH4 mezzanine spares available after the CMS central pixel tracker installation, two POH4 modules will be used in the new portcards.

The POH4 modules support only four output fiber channels, with respect to the seven supported by POH7s, as the name suggests, therefore two of such modules are used in parallel. Each detector plane data output is connected to one of the fiber channels, sending data to the Pixel FED.

Finally, connections for the linear actuator and position sensor have been added.

The back-end DAQ system is substantially identical to the one used in Run 2. The same structure is shared, with minor differences in the firmware versions used on the FC7 cards and updates to the Pixel Online Software (POS) that grant compatibility with the CMS central DAQ. Because of the differences between PSI46dig and PROC600 in the hit

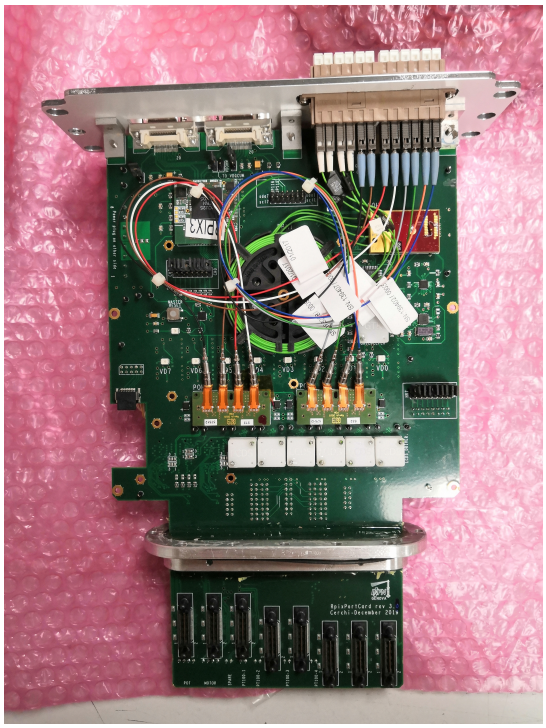

Figure 5.7: PPS Run 3 portcard prototype with all the components mounted on it. The eight connectors at the bottom provide the links to the flex hybrids and are located inside the secondary vacuum of the pot, while the remaining part of the board sits outside. The two connectors on the left are the additional ones, not connected to the control electronics.

encoding, a minor update to the Pixel Online Software data decoding was needed and propagated to the reconstruction software.

Improved module calibration routines have been implemented in the POS. A detailed description is provided in Section 5.3.

5.2 Pixel tracker movement system

The pixel tracker movement system controls and operates the linear actuators installed in the detector packages. Developed for Run 3, it was designed to implement a reliable and easy-to-use interface for the motors without requiring complex and time-consuming tunnel activities for its installation. An overview of the hardware and software implementations

and preliminary tests is presented in the following sections.

5.2.1 Hardware implementation

The linear actuators installed on the pixel tracker detector packages are controlled with a dedicated X-MCC2 driver module [107], shown in Fig. 5.8, produced by the motor manufacturer.

Figure 5.8: Picture of the X-MCC2 motor driver.

X-MCC drivers can connect to many Zaber devices and move them either via a rotating knob or a USB interface that receives commands from a computer. Furthermore, X-MCC modules can implement multiple channels, each one called *axis*. This is the case for the X-MCC2, which has two of them. Linear actuators move only in one direction; therefore, one axis is enough to control a motor. In the pixel detector case, the two linear actuators of the stations in the same arm are controlled by the same X-MCC2 module and connected to its two movement axes.

Zaber devices are not rated for radiation application, but linear actuators are mainly made of metallic components, which are mostly unaffected by irradiation; therefore, their usage is safe. However, this is not the case for X-MCC drivers, which contain electronic components whose functionality could be heavily affected by ionizing particles. Because of this, ≈ 50 m-long cables were installed in the LHC tunnel from the RP positions to the so-called *alcoves*, existing caverns lying behind concrete shielding (Fig. 5.9). The alcoves already host some PPS components such as

vacuum pumps and low voltage power supplies, alongside LHC machine devices (control electronics, helium pumps etc.).

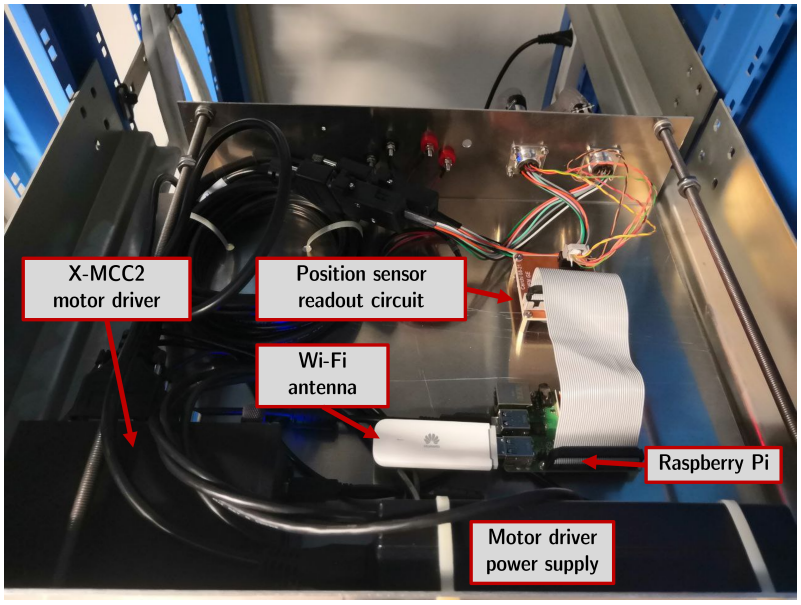

Figure 5.9: Picture of the control electronics for the movement system installed in the alcove. The X-MCC2 driver is visible in the lower-left part of the picture, close to its power supply unit, on the right. The Raspberry Pi is in the center, with the 4G modem. It is connected to the dedicated auxiliary circuit to read the position sensor via a flat ribbon cable.

The X-MCC2 motor driver is therefore positioned in a dedicated rack slot in the alcove. To allow for remote control, a Raspberry Pi 3B+ microcomputer [108] is connected to it via USB and external communication with the Raspberry Pi is provided with a 4G USB modem by Huawei. Such a solution was pursued as no cabled network connection is available in the alcoves, and its addition would have significantly increased the cost and complexity of the control system installation. On the other hand, a CERN 4G phone network by Swisscom is available at all times in the tunnel and it provides a direct access point to the CERN General-Purpose Network (GPN), representing a clean and inexpensive solution for the movement system.

An additional task assigned to the Raspberry Pi is to read the 10 kΩ linear potentiometer that provides feedback on the detector package po-

sition. This is performed via an auxiliary circuit that uses a MCP3008 10-bit ADC to digitize the potentiometer output, used as a voltage divider.

This setup is identically replicated in the two PPS arms. A virtual machine in the CERN network is used to communicate with the two Raspberry Pis located in the alcoves and provides a single monitoring and control point to the user.

5.2.2 Software implementation

The software that monitors and control the pixel detector movement system is designed with the following principles:

- Easy configuration: allow for quick installation and commissioning, without constraints induced by the software.
- Ease of use: do not require specific training or knowledge to perform detector movements.
- Detector safety: it must be impossible to issue movements that might damage the detectors.
- System safety: only recognised users should be allowed to issue detector movements.
- Monitoring and logging: detector position information must be regularly collected, kept safe, and accessible during operation.
- Fault tolerance: the system must be able to recover almost automatically when errors occur, e.g. connection or power loss.

The movement system is controlled via multiple programs that are installed partly on the Raspberry Pis and partly on the above-mentioned virtual machine. Both parts communicate with an online database supplied by CERN via the Database On Demand service (DBOD) [109].

The entire software is available in three dedicated repositories, and its documentation is provided in the CMS TWiki system. Most of the code

is written in Python, except for XML configurations, SQL commands to interact with the DB and some bash scripts.

The software is configured via a global XML file, used by the Raspberry Pi code and the web interface. It contains information about:

- Detector motors in use: their arm, station and RP identifier
- Motor driver axis to which each motor is connected
- Static IP address of the Raspberry Pi connected to the motor driver
- Limits of the linear actuator range of motion
- Motor movement speed limit
- DB connection data
- Movement system calibration parameters
- Position sensor logging parameters

The presence of an easy-to-read shared configuration file makes the setup of the system fast and quick to change.

Database

The database uses a MySQL 8.0.26 instance deployed and maintained by the CERN DBOD service. Its purpose is to ensure adequate preservation and availability of detector position and movement data.

Two are the main tables contained in the DB: *movements* and *measurements*. The former logs whatever movement is issued by the motor system, together with the relevant information to pinpoint it in time and location, i.e. the date and time of the start and finish of the movement, its nominal length, the RP identifier and the initial and final position measured by the linear actuator. The latter contains data about the potentiometer reading performed by the Raspberry Pi, again with the associated time and RP reference.

There is one additional table type saved in the database, which is called *hysteresis*. Its name recalls the hysteresis calibration that is performed with the software (further details are given in the web interface section). Multiple movements are issued in the calibration, and position measurements are taken with the linear actuator and the potentiometer at each step. Hysteresis tables store the data points collected, which are provided to the user in the web interface and act as a calibration curve to tune precise movements.

Raspberry Pi software

The Raspberry Pi is a single-board computer suited for light tasks. The movement control system runs a Debian-based operating system called Raspbian, and it performs multiple tasks mainly targeted at providing connectivity to the motor drivers and logging the motor positions.

Two bash scripts are automatically executed when the Raspberry Pi is powered up. The first activates the 4G USB modem and connects to the CERN GPN. Since Raspberry Pis are powered via remotely controlled power supplies, power-cycling the board is always possible and it allows to recover it in the event of a connection loss. The first script is re-executed and the connection re-established when this is done. The second script launches a socket server application that listens on a defined port. This allows external devices to communicate with the Raspberry Pi via that port in an ad-hoc protocol.

The server is configured to receive commands from devices that identify themselves with a pre-defined password. Such commands are used mainly to issue potentiometer measurements and launch the execution of the Zaber-Bridge application [110]. This program allows the Raspberry Pi to forward TCP/IP signals to the motor driver, such as the motor commands sent by the web interface.

An alternative solution would see the Raspberry Pi directly executing the application that sends such motor commands. This is, however, avoided to lighten the Raspberry's workload and centralise this task,

which is instead executed only by the web interface that runs on a dedicated virtual machine.

Concurrent with the server execution, a background process starts performing position sensor measurements at pre-defined time intervals. Such interval is defined in the global XML configuration file.

After each measurement, an attempt to write data to the DB is made. If the DB turns out to be unavailable, measurements are cached locally in a text file and sent to the DB whenever it becomes available again. This solution minimises potential data losses because of DB unavailability or connection issues. Because of the relatively large amount of memory available to the Raspberry Pi, many months of position readings could be stored locally and manually recovered in case of unexpected long-term connection issues.

Web interface

The web interface of the pixel detector movement system is a Python Django application that provides a graphic view of the detector to the user. Its primary purpose is to make the user interaction easy for monitoring, commissioning and operation purposes. Deployed on the CERN OpenShift platform [111], it runs on a dedicated virtual machine and represents a single point of contact for the user that needs to operate the movement system.

Two levels of safety are required to access the page, which is reachable only within the CERN network: a user can connect only when authenticated via the CERN Single Sign-On (SSO). When correct authentication is detected, it is checked for further access rights granted via the CERN e-group system, a mailing list service widely used for similar purposes.

The web page dynamically changes appearance depending on the user's membership in a dedicated group. If the user is not a member, he or she will be presented with information about the current status of the movement system, such as the last known position readings and calibration curves. Otherwise, specific buttons and editable fields will also

appear, giving the user a way to insert precise movement quantities and buttons to issue such commands.

When a command is issued, the virtual machine connects to the relevant Raspberry Pi, starting the Zaber-Bridge application. After that, the movement TCP/IP command is sent to the Raspberry Pi using the Zaber-motion library [112] and logged in the database.

More frequent position measurements are performed during the movement to guarantee adequate monitoring, and the software checks for any possible error, e.g. if the connection is lost abruptly or the movement is restrained. Any error is printed in the user web interface and logged in the web server console.

The web server is also equipped with detector damage protection mechanisms: if a movement outside the detector package is issued, an error is detected, and the command is stopped.

The web interface implements a quick hysteresis measurement tool that is currently hidden to avoid inadvertent activation. When such a command is issued, the motion range of the detector package, specified in the configuration XML file, is sub-divided into a configurable amount of intervals, usually about 20. Successive movements of appropriate size are issued, and the position of detector package is measured after each of them. This measurement first moves in one direction, extending the linear actuator and then retracting it.

The resulting graph, shown in the web interface (Fig. 5.10), illustrates the detector package true position, measured by the linear potentiometer, as a function of the motor nominal position. If no strong resistance is found along the path, the two quantities are expected to be linearly correlated, with a possible small non-linearity at their extreme, where the detector package approaches its motion range limits. Such non-linearity can appear differently when changing the direction of movement and thus yield a hysteresis curve.

Since these measurements have been observed to be highly reproducible, they can be used as calibration curves by the user who needs to define the motor movement length. Data points are therefore saved

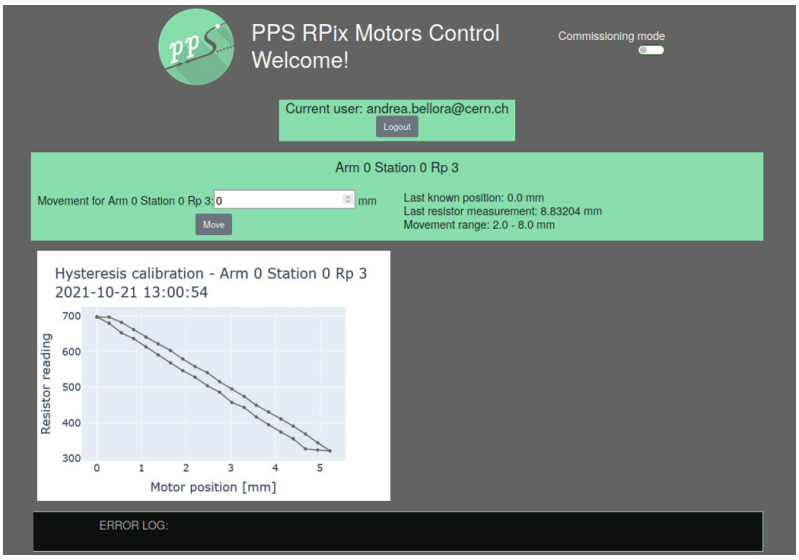

Figure 5.10: Example view of the user web interface for controlling the tracker movement system.

in the dedicated database tables, and the last measurement graph is presented to the user in the web interface for each detector station enabled.

5.2.3 Movement system tests

An extensive series of tests was performed to confirm the proper functioning of the pixel tracker movement system.

Preliminary checks on the motor suitability were carried out at the INFN laboratories in Genova, confirming that the linear actuator can provide enough force to move the detector package in a dedicated mock-up and that the installed springs are capable of pushing it in the opposite direction. Movement along the whole range was achieved both at ambient temperature and in operational conditions, about $-20\,^{\circ}\mathrm{C}$, by testing the system in a climatic chamber. Furthermore, the linear potentiometer reading showed no strong dependency on temperature; hence no corrections to its position measurement is needed.

The control system was thoroughly tested in 2021: repeated movement commands were sent reliably, with a negligible fraction of failures, all

detected by the system. The motor control over a long distance was tested with a dedicated 70 m long cable and did not show any performance degradation caused by its usage.

The network connection via 4G modem proved to be very stable, as it continuously functioned for several months. Tests in the LHC tunnel showed adequate connection characteristics in the alcove, where the Raspberry Pi boards will be located. Recovery procedures in case of connection loss were also successfully tested.

Each detector package was characterised in the H8 beam test facility at the CERN North Area, where a RP mock-up is available and equipped with vacuum and cooling units identical to the ones used in the LHC tunnel. Preliminary hysteresis measurements were performed both manually and with the web interface, validating its functionality.

An example of the typical result obtained during a hysteresis calibration using the web interface is presented in Figure 5.11. The short non-linear regions at the extremes of the movement range represent points where the displacement detected by the actuator does not correspond to the effective detector package movement. The movement interval is represented by the excursion of the linear potentiometer reading, shown in 10-bit ADC counts (c_{ADC}). The conversion from ADC counts to displacement in mm can be performed with the following formula:

$$l = \frac{127\,\text{mm}}{1023} \cdot c_{ADC} \tag{5.1}$$

which accounts for the total excursion of the potentiometer (127 mm) and the 10-bit ADC range.

The range of motion of each detector package was determined and found compatible with expectations.

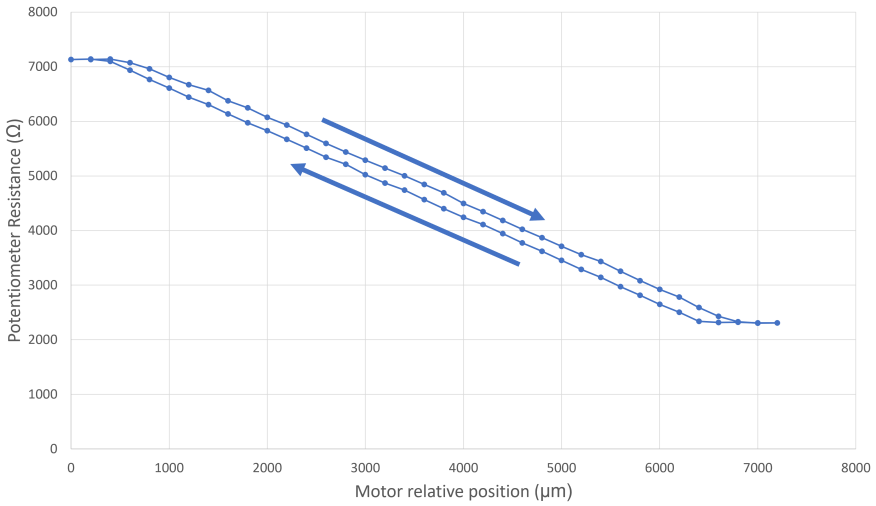

Figure 5.11: Hysteresis calibration performed on a detector package installed in the RP mock-up in the CERN North Area. The potentiometer resistance, measured with the dedicated circuit connected to the Raspberry Pi, reflects the real position of the detector package. The motor relative movement reflects the cumulative displacement issued to the linear actuator. Arrows denote the direction of movements when while collecting data points.

5.3 Tracking package qualification and calibration

In order to qualify the functionality of tracking champignons, a set of tests was developed and performed during Run 3 preparation, based on the procedures employed in Run 2.

The qualification covers many aspects: mechanical adequacy, vacuum tightness, cooling functionality, and electronics tests. The latter part, which is the most extensive, assures the functionality of the detector modules and the portcard components. Furthermore, results from electronics tests are used to derive DAQ configurations that are crucial for the proper detector operation.

The following sections describe each testing procedure, that together with the movement system test presented in Section 5.2.3 complete the preparation of tracking champignons for installation. Tests are usually

performed in this order: firstly, the functionality of the modules is checked with the so-called Digital Test Board (DTB), developed for testing the CMS Phase I ROCs at the Paul Scherrer Institut (PSI). This procedure allows selecting modules that are suitable for installation and ready to be assembled in detector packages. The second tests are calibrations performed with the μTCA DAQ system (Section 3.1.5), that are essential to prove the functionality of the portcard and its compatibility with the detector modules. Finally, the champignons are assembled and tested in a RP mock-up, equipped with vacuum and cooling services.

5.3.1 Module tests with the DTB

The DTB (Fig. 5.12) is a test board which mounts an Altera Cyclone III FPGA to control the board and the communication with the module ROCs. A custom digital level translator chip (LCDS-LVDS) handles the conversion of signals from the FPGA to the ROCs and TBM, and data from the detector are stored in a 128 MB RAM. The DTB is connected to a computer via USB and is controlled via pXar, a custom program developed for the PSI46dig ROC and adapted for the PROC600.

Figure 5.12: Picture of the Digital Test Board (DTB).

Most of the tests performed with the DTB can be repeated with the

μTCA back-end and will also be performed during operation, while not actively taking data, for monitoring and re-calibration.

Preliminary functionality test

In order to assess the basic functionality of a pixel module, a series of preliminary checks is performed.

First of all, a test checks whether programming the ROC registers is possible, by verifying that voltages and currents respond correctly. Registers are then set to their nominal value and the DTB measures the analog current draw (Iana) of each ROC, which is expected to be about 25 mA in nominal conditions (Fig. 5.14a).

Successive tests make use of the charge injection circuit of the ROC, which allows to send a calibration charge to the amplifier input of each pixel. A primary optimization of the charge injection is thus needed for further tests. This is done by performing a double efficiency scan of two ROC registers: CalDel and VcThr (also called VthrComp). The former sets the delay of the charge injection with respect to the trigger signal. The latter is directly proportional to the threshold of all pixel comparators. It must be noted that the input signal to the comparator is negative, therefore, in terms of signal amplitude, higher VcThr values correspond to lower thresholds.

While performing the registers scan, 200 Vcal (8 ke^-) calibration charges are injected. The shape of the efficiency scan (Fig. 5.13) resembles a tornado, thus the result is usually called *tornado plot*. The bottom of the tornado indicates the value where the threshold is greater than the injected charge. Conversely, at the top, the threshold becomes so low that the ROC buffers are filled with noisy hits, causing inefficiency. The horizontal width of the tornado corresponds to the 25 ns acceptance window associated with each bunch crossing, equivalent to approximately 62 CalDel.

The tornado is slanted because of time-walk effects, i.e. signals of greater amplitude,relatively to the threshold, cross the threshold earlier

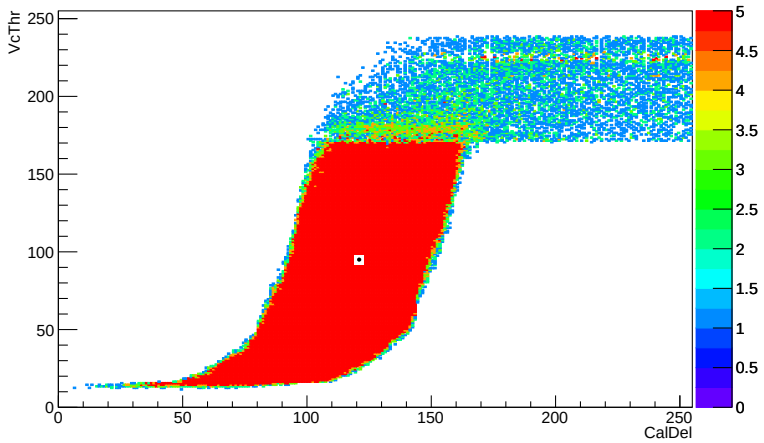

Figure 5.13: Example of tornado plot (efficiency in the CalDel-VcThr plane) for a Run 3 PROC600 module.

than small amplitude ones. Hence, at lower thresholds, the calibration pulse has to be delayed more (higher CalDel) than at high thresholds.

To perform subsequent calibrations, a CalDel-VcThr working point is chosen in the center of the tornado efficient region, as shown in Figure 5.13.

The next preliminary test consists in injecting each pixel multiple times and checking how often a consistent data stream is obtained. This is the so-called *PixelAlive* test. Then the *Address Decoding* test is performed, which compares the address of the hit pixel in the output data with the one in which the calibration charge was injected. The last preliminary check is the *Mask* test, in which the comparator of each pixel is disabled while injecting the charge. The test verifies that no output is observed, confirming that the pixel is indeed masked.

All these tests are performed on one single pixel at a time while masking the others to avoid cross-talk effects. An example of the test results is shown in Figure 5.14. In Address Decoding and Mask tests, pixels not passing the test are assigned a -1 value, while the ones deemed dead by the PixelAlive tests are assigned a 0 value.

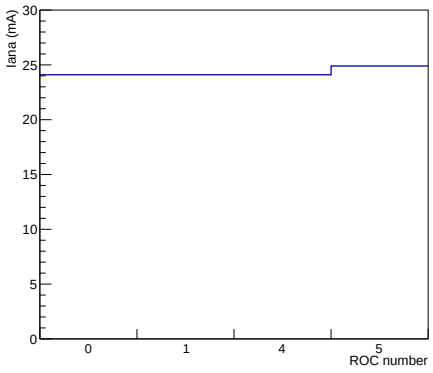

(a) Analog current drawn by each ROC, numbered following Fig. 5.4, as measured by the DTB.

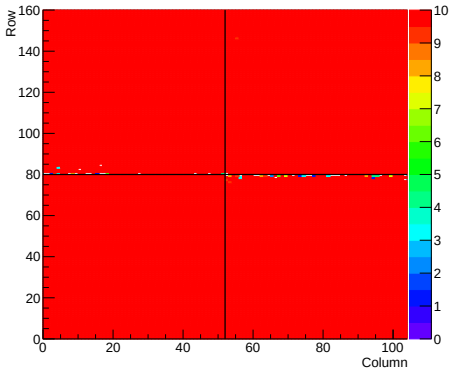

(b) Result of the PixelAlive test on one module. Malfunctioning pixels are detected along its top border.

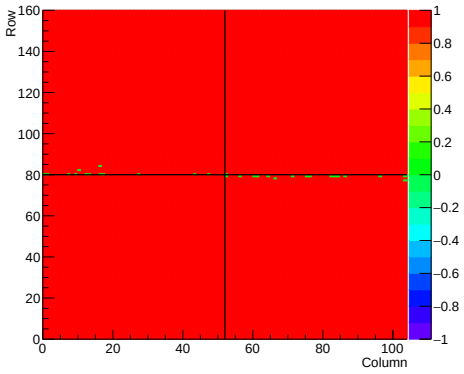

(c) Result of the Mask test.

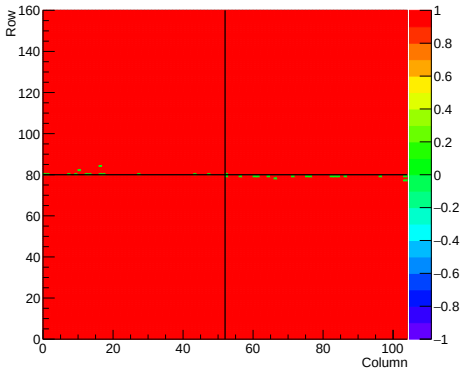

(d) Result of the Address Decoding test.

Figure 5.14: Example of the preliminary test results on a Run 3 pixel module.

Threshold measurement

The charge injection capability of the ROC allows to measure the comparator threshold of each pixel. This is done by performing an efficiency scan as a function of the injected charge. In an ideal noiseless case, the efficiency should follow a step-like function, going sharply from zero to one when the injected charge exceeds the threshold. The presence of noise, assumed to be gaussian, smoothens the transition, resulting in an *S-Curve* shape for the efficiency as a function of the injected charge. The width of the slope (σ) represents the noise, while the 5% point corresponds to

the measured threshold.

The result is obtained by fitting the efficiency with an error function, as illustrated in Figure 5.15:

$$S(x) = \frac{1}{2}\left(1 + Erf\left(\frac{x-\mu}{\sigma\sqrt{2}}\right)\right), \; Erf(x) = \frac{2}{\sqrt{\pi}}\int_0^x e^{-t^2}dt \tag{5.2}$$

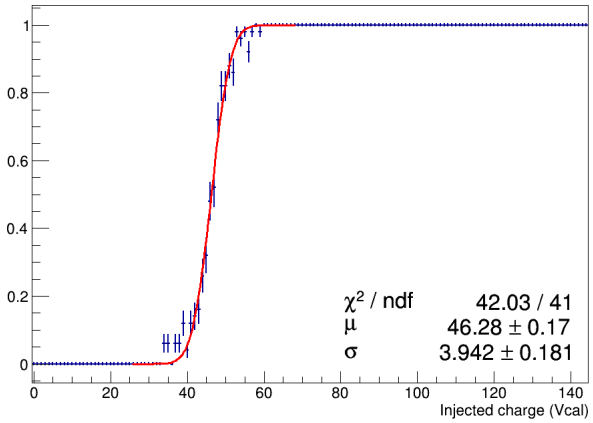

Figure 5.15: Efficiency scan as a function of Vcal, fitted with equation 5.2.

The threshold measurement is performed on each pixel, with a maximum of 3 parallel pixel injections, far from each other. This speeds up the measurement, while avoiding cross-talk effects and stress in the charge injection circuit, which cannot handle too many (~ 10) concurrent precise injections.

Figure 5.16 presents threshold measurement results for all the pixels in a Run 3 detector package, and shows the noise and threshold 2D distributions on one of the modules. In the two lower plots, pixels along the internal borders (row 79 and column 51) usually show higher noise. This is because the dimension of those pixels is doubled to fit multiple ROCs on the same sensor; their larger capacitance induces larger noise levels. This is also reflected in the excess in the noise distribution tail between 6 and 8 Vcal.

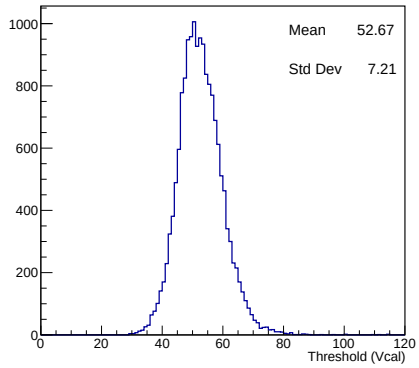

(a) Threshold distribution.

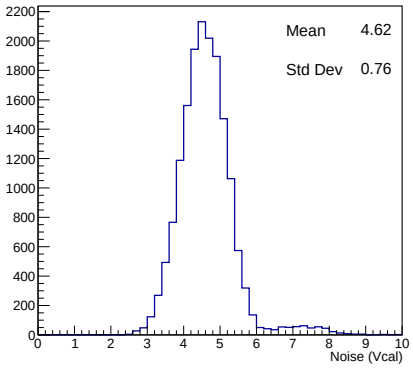

(b) Noise distribution.

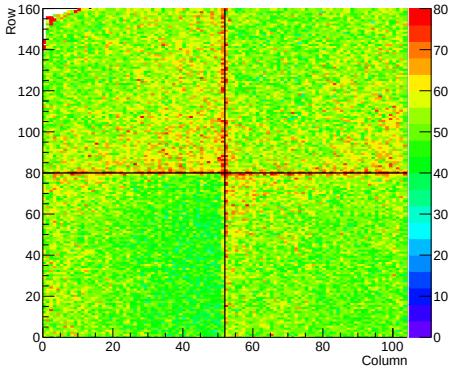

(c) Module 2D threshold map.

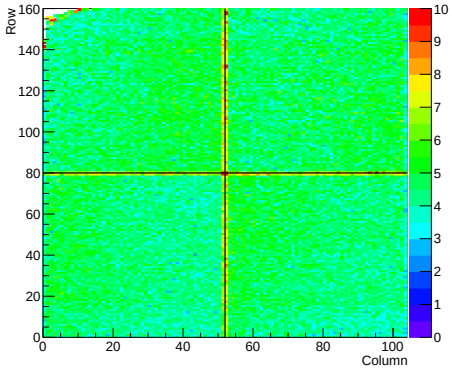

(d) Module 2D noise map.

Figure 5.16: Example of the S-Curve measurement results on a Run 3 pixel detector package.

Trimming

The *trimming* procedure aims at reducing the threshold spread among pixels in one ROC. Threshold fluctuations are intrinsic to the electronics, however they can be counter-balanced by properly setting the TrimBit and Vtrim DACs. In order to do so, multiple steps need to be performed. Firstly, all TrimBits are set to their maximum value of 15, corresponding to no threshold voltage reduction, and a VcThr value that makes all pixels efficient for injected charges above the target value.

After this, the threshold, in Vcal units, is measured for all pixels. The pixel with the highest threshold is identified and its TrimBit is set to

zero (maximum threshold voltage reduction). The maximum reduction is determined by the Vtrim DAC, which is unique for the whole ROC. In order to choose the correct Vtrim value, a double efficiency scan as a function of Vcal and Vtrim is performed on the selected pixel. Vtrim is determined by requiring the threshold of that pixel to be equal to the target value.

This assures that the TrimBit-induced threshold reduction range covers all the other pixels in the ROC and with an iterative procedure all the other TrimBits are determined.

Finally, another threshold measurement is performed to confirm that the trimming procedure was successful and the threshold spread actually decreased. Threshold RMS reductions in the 40–70% range are usually observed (Fig. 5.17).

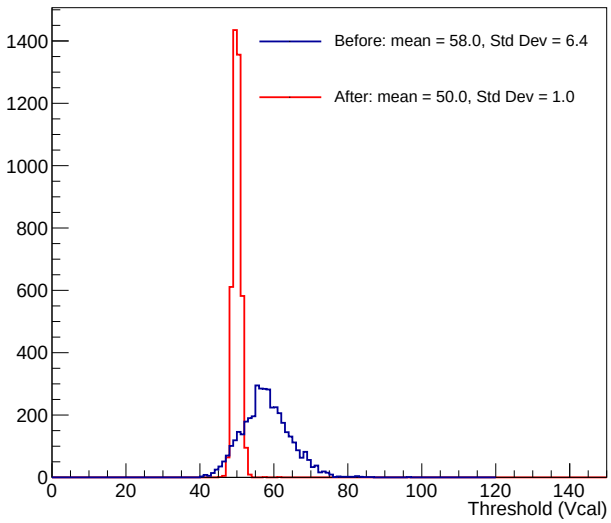

Figure 5.17: Threshold distribution of a ROC before and after trimming.

Pulse height optimization

The pulse height optimization is necessary to set the PHOffset and PH-Scale registers, which regulate the offset and dynamic range of the 8-bit

ADC of the ROC. Values must be chosen in a way that ensures the digitization of signals coming from any pixel, thus has to account for pixel-to-pixel variations. Furthermore, a better resolution at low amounts of charge is preferred, despite the possible ADC saturations due to large signals. In fact, large charge releases are seldom detected by a single pixel, as they often generate multi-pixel hit clusters. Instead, when the charge is shared among two or more pixels, lower signals are induced and their accurate digitization allows to improve the hit position measurement by estimating it as the charge barycenter or exploiting the charge distribution asymmetry.

In order to find suitable PHOffset and PhScale values, a gain measurement is performed on all pixels. The minimum signal that can be converted by the ADC, regulated by the PHOffset register, is set to match the smallest detectable signal of the ROC when produced by the lowest gain pixel. Conversely, the PHScale DAC is set so that the highest signal to digitize, detected by the highest gain pixel, remains within the ADC range.

Gain calibration

The final step of the ROC test consists in measuring the calibration curve between the charge injected and the ADC output, for each pixel. A wide-range scan in Vcal, from about 2100 e^- up to 56 ke^-, is performed and the ADC output is fitted with the formula:

$$\mathrm{ADC} = p_0 + p_1 \cdot \tanh\left(p_2 \cdot \mathrm{Vcal} + p_3\right) \tag{5.3}$$

which represents the best model for the ADC behaviour in its full range. However, the ADC shows a good linearity in the relevant low-charge region and a linear approximation describes the relation well enough (Fig. 5.18). The slope and intercept of the straight line are thus derived from the fitted parameters from equation 5.3, respectively.

The gain and pedestal measurement is very important for properly assigning weights to pixel hits in the cluster reconstruction. It is not only

performed with the DTB to assess the functionality of detector modules, it is also repeated with the DAQ system after detector installation and during technical stops or periods with no active data-taking, in order to maintain the calibration curves used in reconstruction up to date.

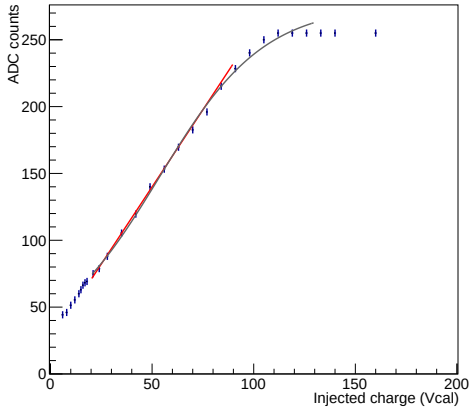

(a) Vcal vs. ADC fit.

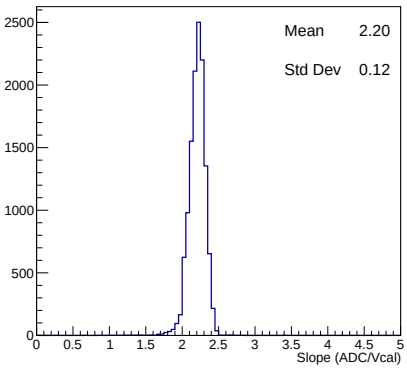

(b) Slope distribution.

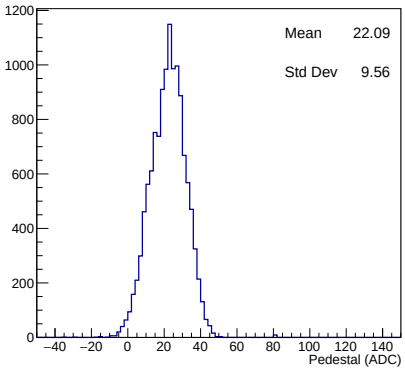

(c) Pedestal distribution.

Figure 5.18: Example of the gain calibration fit measurement results. The upper figure shows the Vcal vs. ADC count characteristic in the low Vcal region. The gray line is the Eq. 5.3 fit and the red line its linear approximation. In the two lower figures the slope (left) and pedestal (right) distributions for a Run 3 pixel detector plane are represented.

X-ray tests

The final test performed with the DTB consists in checking that the bump-bonding procedure was successful. In fact, all the previously described tests, inject calibration pulses in the ROC front-end amplifier, hence they are blind to possible issues in the connection between sensor and readout chip.

This test is performed by exposing, for about 15 seconds, each module to radiation generated via an X-ray tube (Compact 3K5 X-ray generator model by GNR-Ital Structures [113]) in the Genova INFN laboratory. The tube is operated at a voltage between 5 and 60 kV, with currents in the 0.1-60 mA range. The silver anode yields an X-ray spectrum with two peaks at about 22-25 keV.

Data are acquired with a 100 kHz random trigger. The hit distribution is inspected, and pixels with damaged bump-bond are found, as they do not present any hit.

X-rays penetrate the module from the flex-hybrid side, going, in order, through the flex, the sensor and the readout chip. Figure 5.19 displays the hit distribution detected by a good quality detector module.

The copper ground layer of the flex-hybrid absorbs part of the radiation, therefore regions where the layer is not present show higher hit counts. Such regions correspond, for instance, to the circular wire-bonding pad on the flex hybrid PCB dedicated to the sensor for high-voltage connection. Other pads where surface mounted components are soldered, can also be seen.

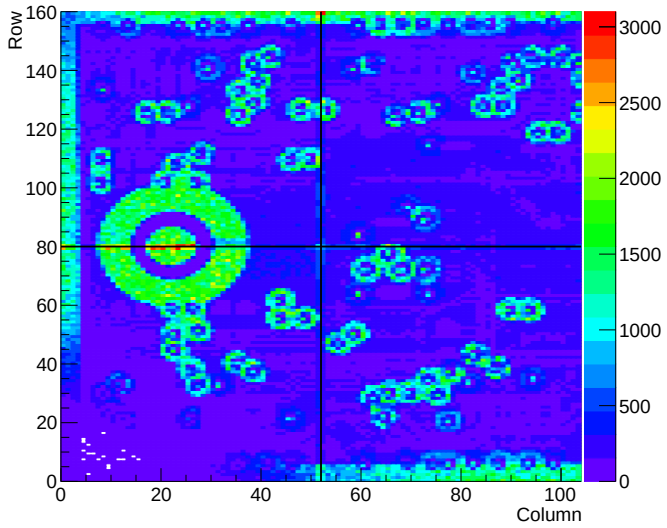

Figure 5.19: Hit distribution observed when performing the bump-bonding functionality test. The detector module is exposed for 15 seconds to the X-rays produced by the tube operated at 30 kV and 4 mA. The regions with higher hit concentration correspond to features in the flex hybrid layout (circular patterns indicate interrupted parts in the ground layer) or correspond to regions where the flex does not cover the sensor area (lines along the edges). In both cases, the X-rays have to traverse a lower amount of material, thus having higher chance of being detected.

Module production summary

Out of the 60 bump-bonded sensors, 49 were used for module production and one was used for testing and qualifying production tools. The remaining 10 were kept for spares. Current-Voltage characteristics were measured again, to verify the breakdown voltage and the leakage current in operational conditions: 38 modules ($\sim 78\%$) were found suitable. Out of these, three of them showed issues in communicating with the ROCs which prevented their configuration, and thus were discarded. All the rest remaining ones were deemed suitable for installation.

On average, less than 10 non-working pixels per ROC were found (less than 3‰), and finally, 24 out of the 35 fully qualified modules were assembled in detector packages and used for further qualification and

testing.

5.3.2 Qualification with the MicroTCA system

After detector modules are tested with the DTB and assembled in detector packages, they are connected to the portcard and further qualification is performed with the MicroTCA DAQ system described in Section 3.1.5.

These tests aim at configuring the portcard and TBMs, ensuring good communication between the back-end DAQ and detector modules. Any test performed with the DTB, can be repeated with the MicroTCA system, allowing for full-assembly tests with vacuum and cooling. Only X-ray tests are not repeated after the complete assembly of the champignons.

In the following paragraphs, a description of the test procedures unique to the MicroTCA system is presented.

POH bias calibration

The POH4 mezzanines are responsible for sending the data output from the TBM to the back-end DAQ. The laser drivers installed on them are powered with a DAC-adjustable current (POHBias).

The calibration consists in reading the Received Signal Strength Indication (RSSI) value from the FED, which indicates the amount of light detected, while scanning the POHBias register (1 DAC = 0.45 mA). The curve (Fig. 5.20) shows three behaviours: at low values, the digital signal is too low and the RSSI barely changes. A second part follows, where the RSSI grows slowly because only part of the digital signal is above the detection threshold. Finally, in the third part, the signal is completely above threshold and the RSSI increases linearly with the bias.

A working point is chosen in the initial region of the third part, in order to ensure good communication while reducing the laser stress as much as possible. Since POH mezzanines are very delicate components, this calibration also represents a quick way to verify that no damage happened to the POH after handling the portcard.

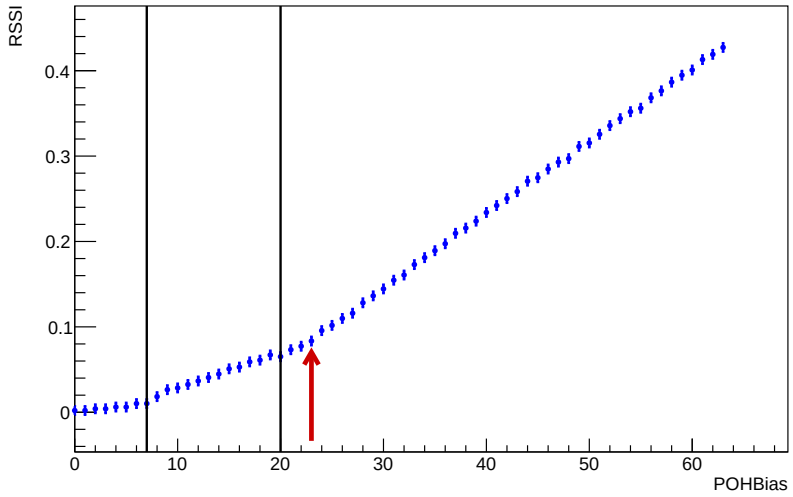

Figure 5.20: Output of the POH calibration for a readout channel. The three segments showing different behaviours are separated by the vertical lines. The chosen working point is denoted by the red arrow.

Delay25 calibration

The Delay25 chip is responsible of fine phase adjustments among fast control signals, i.e. clock, trigger and fast commands. The calibration procedure aims at ensuring the correct programming of the TBM. It relies on two communication lines, one sending programming commands from the pxFEC to the TBM (SDa) and one returning its response (RDa).

The phase of both these signals can be adjusted with the Delay25. The calibration procedure consists in performing a double latency scan in SDa and RDa. For each pair of values, multiple commands of increasing complexity (length) are sent to the TBM, which repeats the command that was received on the RDa line. The fraction of communications in which the command received was identical to the one sent is computed for each complexity level.

Typically, longer commands such as the TrimBit configuration for all pixels have tighter latency requirements than short ones, e.g. TBM register programming (Fig. 5.21a). A combination of SDa and RDa delays such that all the commands sent are always detected is found (Fig. 5.21b).

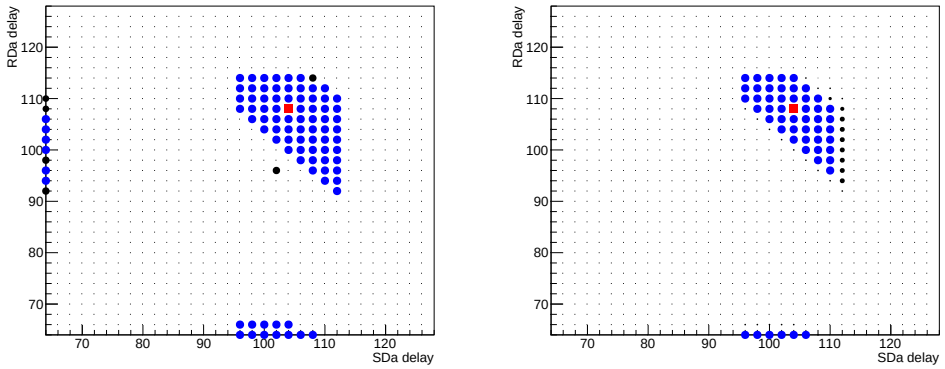

(a) **(b)**

Figure 5.21: Example of the Delay25 calibration output on one detector plane. (a) illustrates the working points found when sending a short command (TBM register setting). (b) shows the intersection between all the working regions for all commands. The red marker denotes the chosen working point.

Since the SDa and RDa latency is unique for all modules, an overlap among their working regions is essential. If no suitable SDa delay is found, it will not be possible to configure all the modules, making some unusable. On the other hand, if the RDa latency is not set correctly, detector modules will still be able to work. Some redundancy monitoring features (readback) will not be available, however this will not affect the data-taking performance. That is the case of CMS BPIX, where the RDa line is not read out by design. Because of latencies intrinsic to the electronic elements that propagate RDa signals from the modules to the Delay25 chip (LCDS drivers), it is not possible to find an RDa latency that works for all modules.

TBM delays calibration

The TBM delays calibration is a another key element in ensuring the proper communication between TBM, ROCs and back-end.

Two primary delays need to be tuned to proceed with further calibrations: the ones applied to 160 MHz ROC data output lines and to 400 MHz TBM data output lines. This is necessary to adjust the phases with

respect to the 40 MHz clock input, so that the TBM headers and trailers are correctly added to the ROC data, 160 MHz data are multiplexed and encoded, and finally sent out by the TBM *DataKeeper*. The two delays are regulated by a 6-bit register in the TBM (TBMPLL): the three least significant bits represent the 400 MHz phase adjustment, and the other three the 160 MHz one.

In order to find working values, a scan of the TBMPLL register is performed while sending charge injection commands to the ROCs. The data output is stored in a FIFO by the FED and analyzed. The calibration checks for the presence of the TBM headers and trailers, thus verifying the correct functionality of the TBM, and then finds ROC data headers. An example of the calibration result for a detector plane is presented in Figure 5.22.

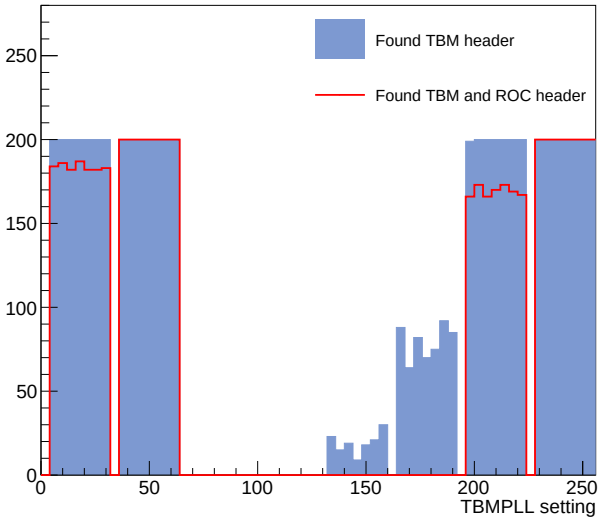

Figure 5.22: Output of the TBMPLL register scan, which regulates the phase adjustment of the 160 MHz and 400 MHz TBM data lines. The two histograms show the amount of successful readouts over 200 attempts, when requiring: only the TBM headers to be present in the data output (blue filled histogram), both the TBM and ROC headers to be present (red empty histogram).

In a fully working module, all headers and trailers should be found in the output when two appropriate delays are applied. However, ROC

headers might not be detected if, for instance, one of the ROCs is malfunctioning or an inappropriate setting of the ROC data input delays was set.

In this latter case, a further scan on the mentioned delays is performed (ROCDelayA and ROCDelayB) while looking for ROC headers in the data, until a correct setting is found.

After the proper tuning of the TBM delays, all the tests and calibrations performed with the DTB can be repeated.

5.3.3 Mechanics, vacuum and cooling tests

Once champignons are fully assembled, they are qualified for installation by performing a series of mechanical and service tests in the CERN North Area. Here a complete RP mock-up is present, identical to the one installed in the LHC tunnel. Detectors are inserted in the RP housing (Fig. 5.23), verifying that no mechanical interference is found and that the procedure can be safely carried out in the tunnel, where champignons must be inserted from the opposite side of the beam pipe (a very complex maneuver, even for skilled technicians).

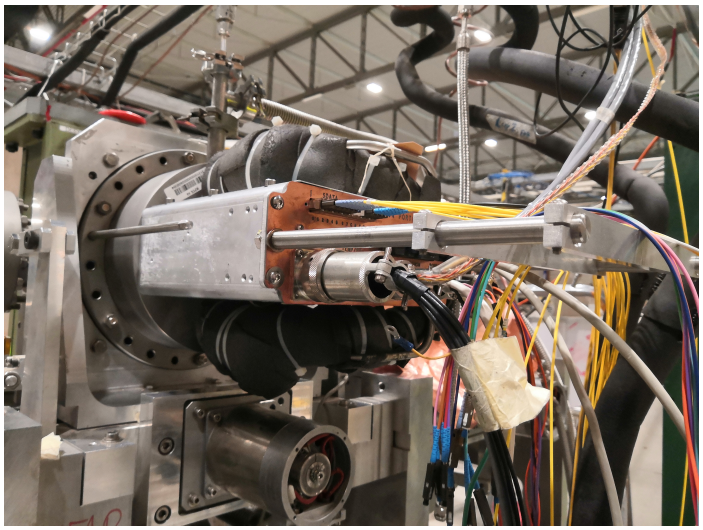

Figure 5.23: Picture of the pixel detector champignon inserted in the RP mock-up in the CERN North Area.

Vacuum tightness tests follow: the RP box is connected to a vacuum pump and a moderate vacuum is applied ($\sim$ 10 mbar). The pump automatically stops after reaching this desired value and the leak rate is monitored via a pressure gauge connected to a dedicated acquisition system. For nominally working champignons, leak rates of the order of $\sim$ 0.1 mbar/h were observed. This check ensures that the vacuum pumps located in the tunnel, which have to maintain under vacuum all the RP units of one sector, will not be stressed during operation and will activate only once every few hours or even days.

The last test concerns the cooling system. The capillaries in the champignon housing are moderately fragile and the assembly procedures, which involve tools being handled in their proximity, could in principle result in unexpected damage. The vacuum lines are thus checked for leaks by circulating nitrogen gas. Subsequently, the cooling lines are tested with a chlorofluorocarbons mixture (Freon), the same used for cooling in the LHC tunnel, and the detector temperatures are monitored with resistive sensors (PT100/PT1000) read out with the dedicated monitoring system (Fig. 5.24).

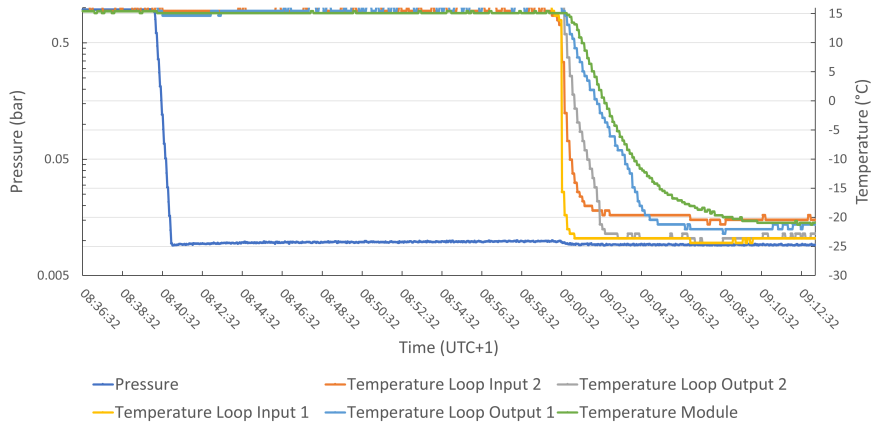

Figure 5.24: Pressure and temperature measurements as a function of time while performing the cooling test of a pixel champignon in the CERN North Area. Offset among temperature readings is mainly due to the sensors accuracy. Temperatures measured at the output of cooling loops or on modules decrease slowly because of the detector thermal capacitance.

Checks are made to assure that temperatures of about -25 °C are reached and that they do not drastically increase when detectors are running calibrations.

At the CERN North Area, with the champignon inserted in the RP mock-up, also movement system tests (Section 5.2.3) and detector module tests with the MicroTCA DAQ back-end are performed to fully qualify the detector before installation.

5.4 Rolling calibrations

In the LHC Long Shutdown 2, CMS dedicated a significant effort to automate calibration procedures. Run 2 detector calibrations required a good deal of person-power, and the experience gained in the process allowed to make many of the procedures automatic.

This approach will reduce the amount of work needed for calibration and provide accurately reconstructed data sooner. During Run 2 data-taking, it was customary to keep low data-tier data, i.e. data with low-level partially reconstructed information, available for a long time. Further reconstruction steps would be performed multiple times whenever new calibrations became available.

Intermediate data-tiers are very heavy in data storage, and re-reconstructions effectively represent a superfluous expense of processing time. In Run 3, this will not take place and, instead, automatic calibrations will allow a first complete reconstruction that already satisfies the analyses accuracy requirements. Intermediate data-tiers will not be saved, and only high-level information will be available, while raw detector outputs will be kept in long-term storage facilities, where the maintenance cost is low but accessibility is limited (e.g. tape storage).

The rolling calibrations are a tool developed in this context. They will automate PPS calibration procedures that would previously take a significant amount of time and person-power. Calibration results such as detector efficiencies will be quickly available for monitoring and analysis. Furthermore, calibration constants that can be used to improve the re-

construction will be directly used to process successive data-taking runs.

5.4.1 PPS Run 3 calibration data processing

As introduced in Section 2.1.7, CMS employs a two-level triggering system. The L1 performs the first reduction and divides the events into categories characterized by physics qualities, for example presence of muon or electron candidates. One of these categories is the so-called *ZeroBias*, which is activated randomly when two filled bunches intersect, with a frequency tuned to match a selected rate. This, by definition, does not require any specific activity in the detectors and is completely unbiased; thus, it is particularly useful for calibration procedures.

For Run 3, PPS implemented its HLT, which can perform a selection based on the proton tracks detected in the RPs. Two categories are defined for calibration. The former one, called *Express*, selects events with one track in both the near and far stations of one of the PPS sectors, while the latter, called *Prompt*, requires at least one track in any RP, with a maximum of four tracks. Raw information for events that pass either of the two PPS calibration triggers is saved in a dedicated *AlCaRaw* dataset that is further processed in subsequent steps.

Figure 5.25 illustrates the calibration data flow during data-taking. At the end of the run, the *Express* reconstruction takes place. It runs over calibration and monitoring datasets, which represent only a small fraction of the data collected by CMS, providing quick feedback about the ongoing data-taking. Here the PPS tracks of the AlCaRaw dataset are reconstructed, and the output is saved in the *Express AlCaReco* dataset, which is the Prompt Calibration Loop (PCL) input.

The PCL is a CMS software mechanism used by multiple CMS detectors that automates calibration procedures. For PPS, this step computes the alignments and calibrates the timing detector output. The parameters that are computed in PCL routines are saved in the *Conditions Database* (CondDB), which contains information for all CMS detectors, organized in run and lumisection intervals of validity.

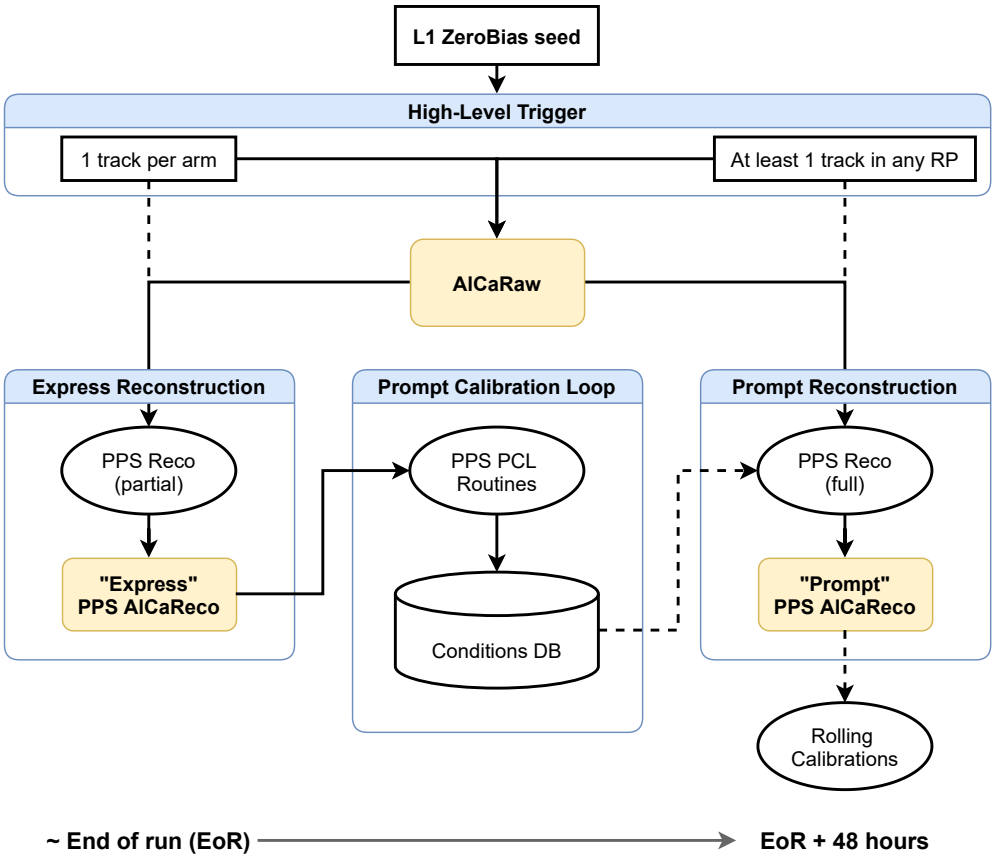

Figure 5.25: Flow chart illustrating the PPS calibration data processing. Yellow boxes represent datasets that are saved on disk. Light blue containers identify each processing step.

The above step is essential because it provides the calibration parameters needed for the *Prompt* reconstruction, which happens approximately two days after the end of a taken run. In this case, all the CMS collected data are processed with the complete reconstruction procedure, yielding datasets used in physics analysis. However, events marked with the PPS Prompt HLT trigger bit are, saved in a separate calibration dataset called *Prompt AlCaReco*, which is used for the rolling calibrations.

Rolling calibrations were developed for procedures that the PCL cannot perform. For example, calibrations that require data already calibrated by the PCL to work or iterative processing. That is only partially supported in the PCL, while no restriction is imposed in the rolling cali-

brations. Furthermore, the PCL is a time-constrained process since it has to finish before the Prompt reconstruction. Instead, rolling calibrations are not strictly necessary for further data processing and therefore the wall time requirement (usually 48 hours for the PCL) can be relaxed.

5.4.2 PPS automation tools

The PPS automation tools repository is the software framework that enables the execution of rolling calibrations. It governs the management and monitoring of the calibration execution, and it is the backbone of the rolling calibration system. This set of tools was developed as an extension of the ECAL automation software, which is used to speed up and monitor the execution of offline detector calibration steps.

The software is based on Jenkins [114], an open-source automation service widely used in the IT industry to implement Continuous Integration (CI) and Continuous Delivery (CD). Jenkins has a multitude of functionalities, but the most relevant for the rolling calibrations is the capability of monitoring one or more Git repositories and automatically acting based on user-defined triggers, so-called *webhooks*. For example, Jenkins can detect when a software update is pushed to the repository and, based on a configuration supplied by the user, build the software and recognise possible failures. Successively, it can perform custom testing routines and thus check that the software update does not disrupt any functionality that was working previously.

The PPS automation tools repository pairs with a Jenkins instance deployed on the CERN OpenShift platform. A user can define a rolling calibration as a set of operations structured in a Finite State Machine (FSM) fashion. The execution of a rolling calibration is denominated *task*, and each operation to be performed on the task, depending on its outcome, changes the task *status*. The user can customise the sequence of status. The user can freely act on each calibration step, defining the operation to be enacted, the list of status, and the conditions that must be satisfied to move from one status to the other.

The implementation is very general and does not impose strong constraints on the software structure, making it possible to implement virtually any calibration procedure. The automation repository not only defines the calibration framework but also provides useful tools to easily implement some of the most common operations that a user might want to perform. The most relevant one is the submission of parallel *jobs* on CERN distributed computing resources via HTCondor [115] or CRAB [116].

Jenkins is configured to execute a monitoring process at pre-defined time intervals. Such a process inspects the status of running tasks, which is persistent by saving it in a dedicated InfluxDB database. Depending on the user-defined calibration steps and the current status, the monitoring process takes action on the task, if needed, possibly advancing its progress. Finally, once all running tasks have been inspected, it exits.

This software structure, paired with the database persistence, allows for efficient execution of monitoring processes, which typically perform fast operations and spend most of their time waiting for parallel jobs to complete. Furthermore, the task progress is not lost if the monitoring process crashes and the action that should have been performed is done during the subsequent execution of the monitoring process.

The downside of this approach is that if a task completes one of its steps, it will not proceed until the monitoring process is executed again. However, such delays are expected to be much shorter than the time needed to run the full calibration, thus negligible. The execution robustness and the decrease of required computing power outweigh this drawback.

A by-product of the InfluxDB usage is the possibility of visually inspecting the execution progress of each task using the Chronograph tool, which provides essential feedback about the automated procedures.

The execution of rolling calibrations can be currently configured manually by specifying the input dataset to analyse. Data from different runs can easily be aggregated to increase statistics or further sub-divided following user-specific definitions.

During Run 3 data-taking, calibrations will be executed as soon as data becomes available. For example, in the case of calibrations on a per-run basis, a task analysing data from each run will be automatically submitted as soon as the Prompt reconstruction produces its output files.

5.4.3 Efficiency workflow

Multiple rolling calibrations procedures have been implemented using the PPS automation tools. The most notable for the Run 3 pixel tracker is the so-called efficiency workflow. It consists of multiple steps, ultimately computing the efficiencies illustrated in Sections 3.3.2 and 4.5.

The efficiency computation cannot be performed in the PCL because iteration on different datasets is needed; for example, computing the radiation efficiency requires running over a reference data sample, which is typically different from the one used for detector plane and multiRP efficiency calculation. Furthermore, input datasets need to be already calibrated (i.e. include alignments), which happens only at the Prompt reconstruction level.

The efficiency calculation is implemented using the software structure of CMSSW Data Quality Monitor (DQM) modules. In this format, the processing of a data sample is split into two steps: the former, called *worker*, defines the module output (ROOT histograms), analyses each event and fills the histograms according to the user definitions. This step can be submitted in parallel on multiple machines, processing different parts of the input sample.

When all parallel processes end, the latter step, denominated *harvester*, is launched. It collects the output and merges them, possibly performing operations between histograms.

The efficiency is computed via two DQM modules. The first runs on data collected in the period (physics fill) for which the efficiency is computed. The workers apply the logic needed to fill the numerator and denominator of plane and multiRP efficiency histograms (Figs. 3.18 and 4.15). The harvester adds all numerator and denominator histograms and

computes the division, saving the output to a file that can be visually inspected. The second DQM module computes the radiation efficiency with the same subdivision of tasks among workers and harvester, running on a reference dataset. For the analysed period, equivalent histograms to Figure 3.19 are saved in the output.

The execution of the DQM modules is managed by the Jenkins, which is configured following the flow chart illustrated in Figure 5.26. At each execution of the Jenkins monitoring process, the action described above the corresponding arrow is attempted depending on the task status. When successful, the task status changes to the one pointed by the arrow; otherwise, the status remains the same and the action is attempted a second time at the next iteration. In both cases, the execution of the monitoring process stops. This entire procedure is performed on each submitted task.

The primary use of the efficiency computation as part of rolling calibrations is detector performance monitoring. Frequent efficiency measurements will allow vertical movements (Section 5.2) to be performed in a timely fashion and keep the detector efficiency high despite radiation effects. Furthermore, efficiency results will be quickly available for physics analyses performed on the Prompt reconstruction dataset. Finally, if an efficiency re-computation is necessary, it will be possible to rerun the rolling calibrations with manually adjusted input. This approach will bring significant improvement with respect to the almost completely manual execution of the efficiency measurement done on Run 2 data.

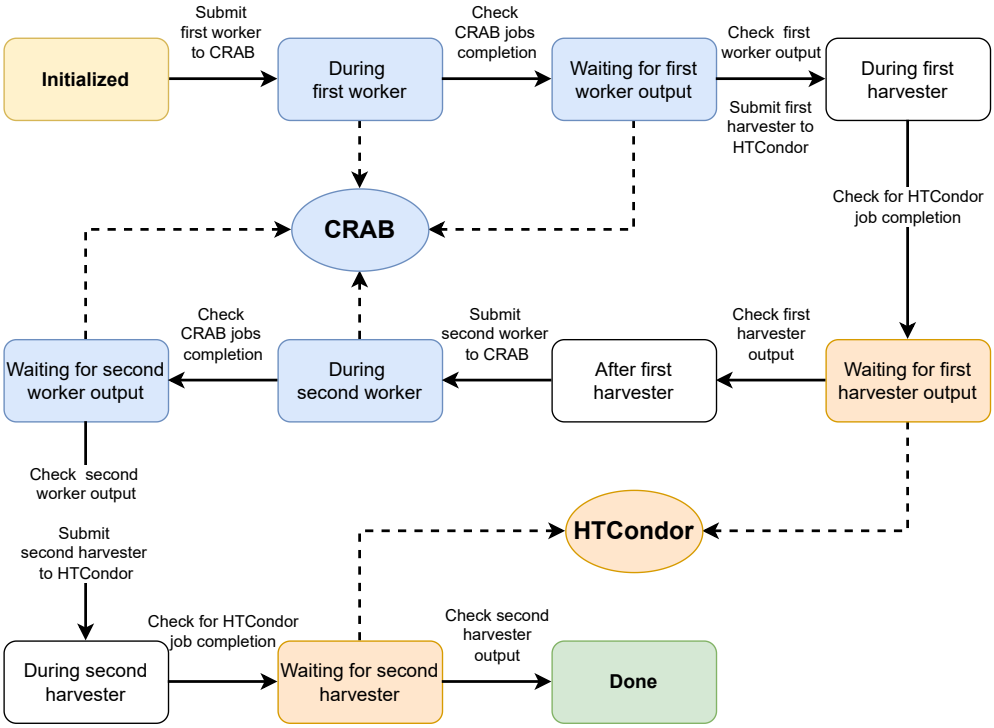

Figure 5.26: Flow chart illustrating the efficiency workflow. Rounded rectangles represent the execution status and the text above arrows that link them describes the actions performed by Jenkins to move from one to the other. Dashed arrows and colours emphasize the execution steps which interact with CERN distributed computing services.

Chapter 6

Search for AQGC in $pp \to pWWp$ and $pp \to pZZp$

This chapter describes the search for Anomalous Quartic Gauge Couplings (AQGC) in high-mass exclusive $pp \to pWWp$ and $pp \to pZZp$ with intact protons. The theoretical background and physics motivation for the present analysis is illustrated in Chapter 1.

The decay channel selected for the search has both bosons decaying to boosted and merged jets. Requiring the protons to be intact and within the PPS acceptance implies searching for events in which the proton fractional momentum losses are in the 0.02–0.15 range, which correspond to invariant masses of the central system from $\sim$ 300 GeV to 2 TeV. As selection criteria favour high masses, the typical energy of a boson pair is much greater than their mass, thus yielding decay products that are subject to a strong Lorentz boost. They are thus likely to be reconstructed as a single large-radius jet, instead of two small-radii ones. It has been shown that a better sensitivity to AQGC is expected for this hadronic channel with respect to the semi-leptonic counterpart [117].

6.1 Data samples and simulation

The data used for the present analysis were collected at $\sqrt{s} = 13$ TeV in the years 2016-2018.

Quality criteria are imposed on data for both PPS and other CMS sub-detectors. In the case of PPS, these criteria require the Roman Pots to be fully inserted in data-taking position, with the detectors in a condition to reconstruct proton tracks. This requirement removes a fraction of the data at the beginning of each LHC fill. During the first year of operation in 2016, a significant amount of time was dedicated to commission the PPS detectors and therefore the integrated luminosity used in the analysis from that year is only 9.9 fb^{-1}. In the 2017 and 2018 samples, the integrated luminosities of the data that satisfy the PPS quality criteria are 37.2 fb^{-1} and 52.9 fb^{-1}, respectively, corresponding to nearly 90% of the luminosity available for CMS analyses without forward protons. In total, the three years combined sum up to an integrated luminosity of 100.0 fb^{-1} [118–120].

Signal events are simulated at leading order with the FPMC [37] generator, for both the $\gamma\gamma \to WW$ and $\gamma\gamma \to ZZ$ production channels via AQGC. The FPMC event generator implements the dimension-6 quartic operators presented in Section 1.2.1. The same event generator is also used for SM exclusive WW events, which, however, yield negligible contributions in the kinematic region considered in this analysis.

The dominant backgrounds from QCD multi-jet production are simulated with versions 8.205 and 8.230 of the PYTHIA [121] generator, with the CUETP8M1 [122] or CP5 [123] tunes. Backgrounds arising from the production of a W or Z boson in association with jets are simulated with MGvATNLO [124]. The background from pair production of top quarks is simulated with POWHEG [125–127]. The parton shower and hadronization for the W+jets, Z+jets, and $t\bar{t}$ samples are carried out with PYTHIA.

A detailed GEANT4 [128] simulation of the central part of the CMS detector, extending to $|\eta| < 5$, is applied to all generated samples. The

same reconstruction procedure used on data is applied to the simulated events.

For the signal samples, the forward protons are passed through the "direct" simulation summarized in Section 4.4, which propagates the protons to the Roman Pot positions, simulates hits in the detector planes, and reconstructs the tracks and proton kinematics in the same way as done for the data. A realistic mix of beam crossing angles and aperture limitations along the beam line is used when simulating the protons.

The protons from pileup interactions are not simulated. Their effect is estimated using data events, as presented in Section 6.4.

6.2 Online selection and event reconstruction

A first selection, by means of a combination of triggers based on jets, is performed online and only events passing this combination are reconstructed.

Using the jet reconstruction performed at the HLT level, the highest transverse momentum (p_{T}) jet is identified and the scalar sum of the p_{T}values of all the jets (H_{T}) is computed. The chosen jet triggers select events based on these quantities, and, in some cases, additional requirements on the mass of the jets are imposed. A dedicated trigger study was not carried out for the present analysis, as the same trigger combination used in Ref. [129] is employed. A detailed study of the trigger efficiency is available in the reference, and in the selection region considered in this analysis, the trigger efficiency is above 99%.

Jets are reconstructed offline from the energy deposits in the calorimeter towers, clustered using the anti-kt algorithm [130, 131] with a distance parameter of 0.8. The jet momentum is determined as the vectorial sum of all particle momenta in the jet, and is found from simulation to be, on average, within 5 to 10% of the true momentum over the whole p_{T} spectrum and detector acceptance. Additional proton-proton interac-

tions from pileup can contribute additional tracks and calorimetric energy depositions to the jet momentum. To mitigate this effect, charged particles identified to be originating from pileup vertices are discarded and an offset correction is applied to correct for remaining contributions [132]. Jet energy corrections are derived from simulation to bring the measured response of jets to that of particle level jets on average. In situ measurements of the momentum balance in dijet, photon + jet, Z + jet, and multijet events are used to account for any residual differences in the jet energy scale between data and simulation [133]. The jet energy resolution amounts typically to 15-20% at 30 GeV, 10% at 100 GeV, and 5% at 1 TeV [133]. Standard selection criteria are applied to each jet to remove jets potentially dominated by anomalous contributions from various subdetector components or reconstruction failures.

Hadronic decays of W/Z bosons are identified by using the ratio between jet 2-subjettiness and 1-subjettiness [134], $\tau_{21} = \tau_2/\tau_1$, and the jet mass, after applying a "pruning" algorithm to remove soft gluon radiation and pileup [132].

The N-subjettiness (τ_N) quantifies to what degree a jet can be regarded as an object composed of N subjets. Jets with $\tau_N \approx 0$ have all their radiation aligned with the candidate subjet directions and therefore have N (or fewer) subjets. Jets with $\tau_N \gg 0$ have a large fraction of their energy distributed away from the candidate subjet directions and therefore have at least N + 1 subjets. For instance, a low τ_2 value is expected for a jet constituted by 2 subjets. In the case of this analysis, low τ_2 and high τ_1 values are expected for jets originating from W/Z boson decays and it has been shown that the ratio of these two quantities $\tau_2 1$ is the discriminating variable of choice to select them over jets from QCD processes [134]. The τ_{21} variable is further refined into a τ_{21}^{DDT} variable, in order to reduce the correlation with the jet p_{T} and mass, using the "Designed Decorrelated Taggers" (DDT) approach [129, 135].

Protons are reconstructed using the multi-RP approach, which combines tracks reconstructed in both tracking Roman Pots in each arm of the PPS detector (Sec. 4.2). Further details on the PPS detector calibration

and proton reconstruction are described in Chapter 4.

6.3 Event selection

An event selection based on the properties of the jets, the protons, and the correlation between protons and jets is applied to favour signal over background.

6.3.1 Jet selection

The jets are first required to have $p_{\mathrm{T}} > 200$ GeV, $|\eta| < 2.5$, and, if more than two pass these criteria, the two with the highest p_{T} are chosen. In the following, these are labeled $j1$ and $j2$, corresponding to the jet with the highest and second-highest p_{T}, respectively. In addition, the dijet system must have an invariant mass $m(jj) > 1126$ GeV, in order to be on the plateau of the aforementioned trigger efficiency. The two jets are further required to have $|\Delta\eta| < 1.3$. Figure 6.2 shows the dijet invariant mass distribution in data and simulation at this stage, in the range of interest for the current analysis, in each of the three years of data.

In exclusive production events the vector bosons are emitted back-to-back, thus the jets originating from their decay are expected to be balanced in azimuth and transverse momentum. This is implemented by requiring the acoplanarity ($a = |1 - \Delta(\phi)/\pi|$) to be lower than 0.01 and the p_{T} balance ($p_{\mathrm{T}}(j1)/p_{\mathrm{T}}(j2)$) to be less than 1.3. In the expression for the acoplanarity, $\Delta(\phi)$ refers to the difference in azimuthal angle between the two jets, defined on the interval $[0, 2\pi]$.

Finally, the selection enhances jets from boosted W or Z decays by exploiting the jet substructure properties. The pruned mass of the jets is required to be between 60 and 107 GeV, i.e. compatible with the W or Z masses. The above-mentioned τ_{21}^{DDT} discriminator is required to have a value less than 0.75, which is expected for two merged quark jets.

Figure 6.1 illustrate the selection variable distributions, comparing data with Monte Carlo, at pre-selection level. In general, the MC repro-

duces well the data in the selected regions. The only partial exception is the Data/MC discrepancy in the low acoplanarity region, however good agreement is reached when other selection criteria are applied.

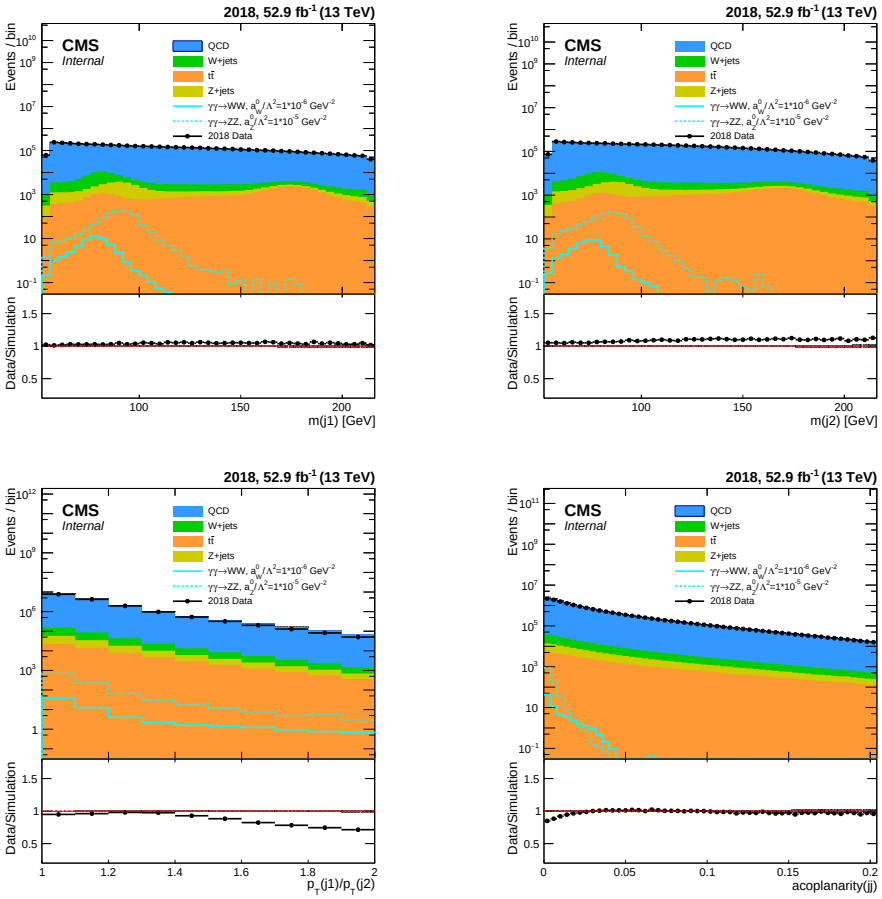

Figure 6.1: Dijet invariant mass spectrum in data and simulation, for the years 2016 (above left), 2017 (above right), and 2018 (below). Leading and sub-leading jet pruned mass (upper left and right, respectively), p_{T}balance (lower left) and acoplanarity (lower right) for the 2018 year. The upper framse show data compared to the stacked background predictions from simulation, the lower frames show the ratio of signal to the sum of simulated backgrounds. The plots are shown at the pre-selection level, with no requirements on the protons, jet substructure, or dijet balance. Examples of simulated signals are shown for protons generated in the range of $\xi = 0.01$–0.20. Only statistical uncertainties are shown.

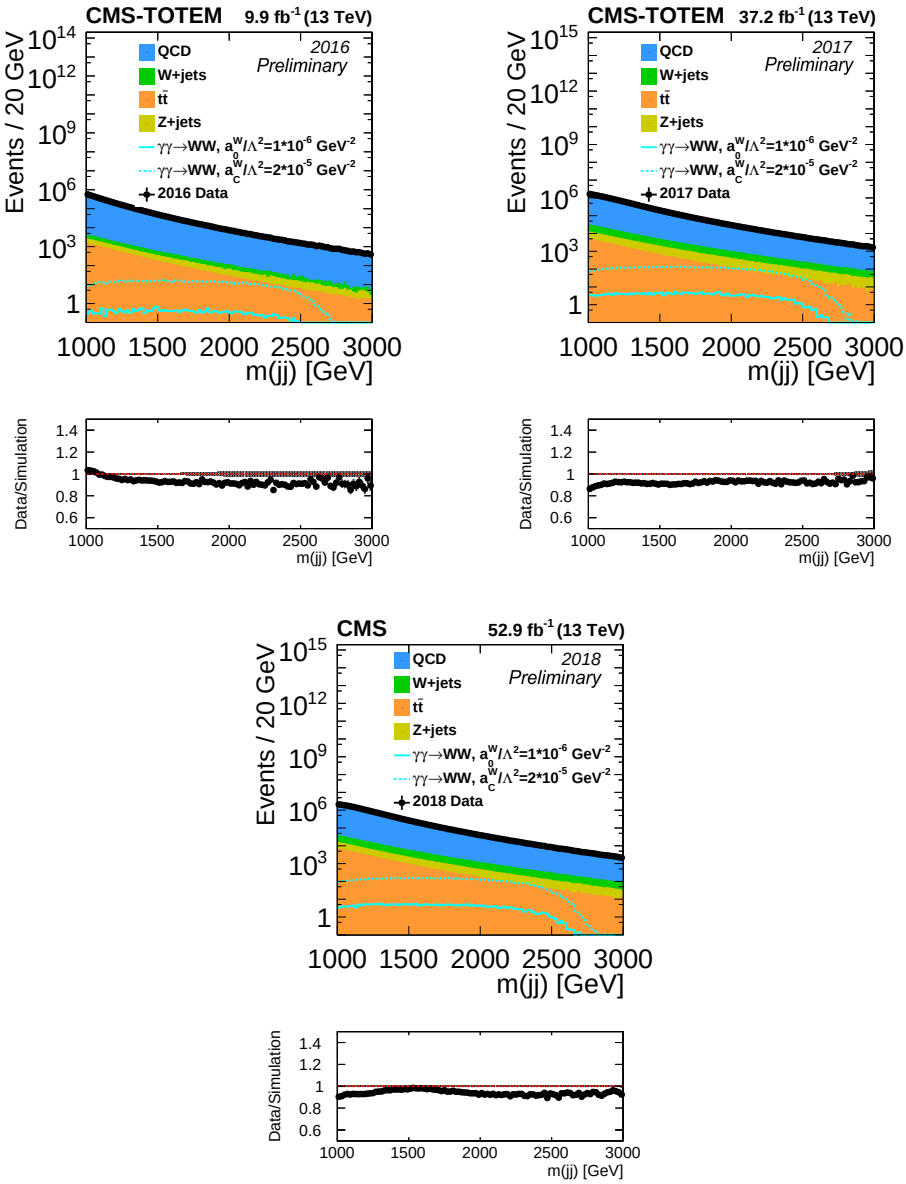

Figure 6.2: Dijet invariant mass spectrum in data and simulation, for the years 2016 (above left), 2017 (above right), and 2018 (below). The upper plots show data compared to the stacked background predictions from simulation, the lower plots show the ratio of signal to the sum of simulated backgrounds. The plots are shown at the pre-selection level, with no requirements on the protons, jet substructure, or dijet balance. Examples of simulated signals are shown for protons generated in the range of $\xi = 0.01$–0.20. Only statistical uncertainties are shown.

6.3.2 *WW* and *ZZ* selection

Multiple variables have been studied to discriminate WW events from ZZ ones. This included τ_{21}^{DDT}, charged/neutral energy fractions and multiplicities in the (sub-)leading jets. Among all these variables, no sizeable difference between WW and ZZ was found with the exception of the jet pruned mass, when comparing its value in the leading versus subleading jet. A discriminator is defined by projecting the two-dimensional distribution of pruned masses of the leading versus subleading jets in simulated signal events along the diagonal, using the variable $\cos(\pi/4)m(j1) + sin(\pi/4)m(j2)$. The resulting distribution contains events grouped into two gaussian distributions (Fig. 6.3), one corresponding to WW and the other to ZZ events.

The exact boundary used to separate the two distributions is optimised by studying signal over background ratios, in which the WW (ZZ) events are considered signal if the result of the $\cos(\pi/4)m(j1) + sin(\pi/4)m(j2)$ discriminator is below (above) a given value, and background otherwise.

The best value for separating the two processes is $\cos(\pi/4)m(j1) + sin(\pi/4)m(j2) = 118$ GeV. No significant dependence of this value on the anomalous couplings was observed, and therefore the single value of 118 GeV is used in the entire analysis.

6.3.3 Proton selection

The protons are required to have a minimum ξ of 0.05, in order to avoid the region of large radiation-induced inefficiencies near the beam (cf. Fig. 4.16), to be within the maximum ξ values imposed by the LHC collimators, and to have constituent tracks away from the edge of the sensors. The upper bounds imposed by the collimators are different for each of the two arms of the spectrometer, each data-taking period, and each beam crossing angle. Therefore, the exact upper ξ requirements vary with the data-taking period. The upper mass limit correspondingly varies

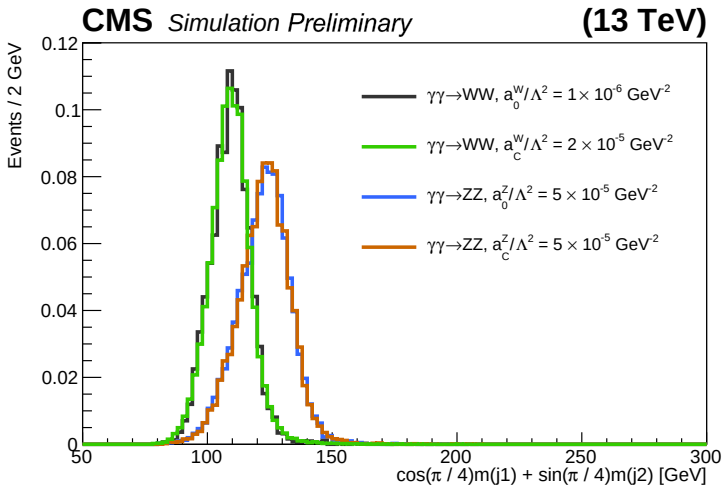

Figure 6.3: Projected distribution of pruned mass of the leading versus subleading jets along diagonal for signal Monte-Carlo events.

between 1.55 and 2.01 TeV (for a proton scattering angle of $\theta^* = 0$) over the course of the LHC Run 2 data.

In the 2016 and 2017 data samples, only one proton per event can be reconstructed in each arm of the spectrometer. With improved detectors in 2018, multiple protons can be reconstructed. The expected significance of the analysis, estimated as $S/\sqrt{B}$, improves by including events with more than one proton, up to a maximum of 3; above this, the effect of showers and non-collision backgrounds becomes significant. Therefore, events with up to three protons per arm are used, and the proton with the largest ξ is chosen for the analysis. The use of multiple-proton events leads to both a significantly larger signal efficiency and a larger combinatorial background in the 2018 data, compared to 2016 or 2017 data.

6.3.4 Proton-jet matching and signal region

The matching between the proton and jet kinematics is based on the mass match ratio, $1 - m(VV)/m(pp)$, and rapidity difference, $y(pp) - y(VV)$. Here $m(VV)$ and $y(VV)$ represent the invariant mass and rapidity of the

WW or ZZ, as reconstructed from the merged jets. The variables $m(pp)$ and $y(pp)$ are the expected invariant mass and rapidity of the central system, calculated from the protons as in Eq. 1.1:

$$m(VV) = \sqrt{s} \times \sqrt{(\xi_{p1} \times \xi_{p2})},$$

$$y(VV) = -\frac{1}{2} \times ln(\frac{\xi_{p1}}{\xi_{p2}}).$$

Two signal regions are defined in the mass match ratio versus rapidity difference plane. A diamond-shaped area, centered around zero, contains the bulk of the signal when both protons are correctly associated to the jets (region δ). In case one of the signal protons is missed and a pileup proton is used instead, the events tend to fall in one of the two diagonal bands of Fig. 6.4. A second signal region (region o) is therefore defined based on these bands. The signal regions were chosen by finding the best orientation for the two bands and diamond boundaries and tuning their widths to maximise the significance, estimated as $S/\sqrt{B}$.

The area with $|1 - m(VV)/m(pp)| < 1.0$ and $|y(pp) - y(VV)| < 0.5$, encompassing both signal regions, remains blinded and is not examined until the selection criteria and background estimation methods are fixed.

6.4 Background estimation

The background is mainly due to processes which mimic the signal final state, combined with unrelated protons from pileup interactions in the same bunch crossing. The largest source of jets is QCD multijet production, with smaller contributions from W or Z bosons in association with jets, and $t\bar{t}$ production. The protons predominantly arise from soft diffractive pileup interactions, which are typically not well-modelled by simulations. For this reason, the analysis mainly relied on data-driven background estimations.

The nominal background estimate in the signal region (region A) is derived by inverting the dijet acoplanarity requirements, and/or the

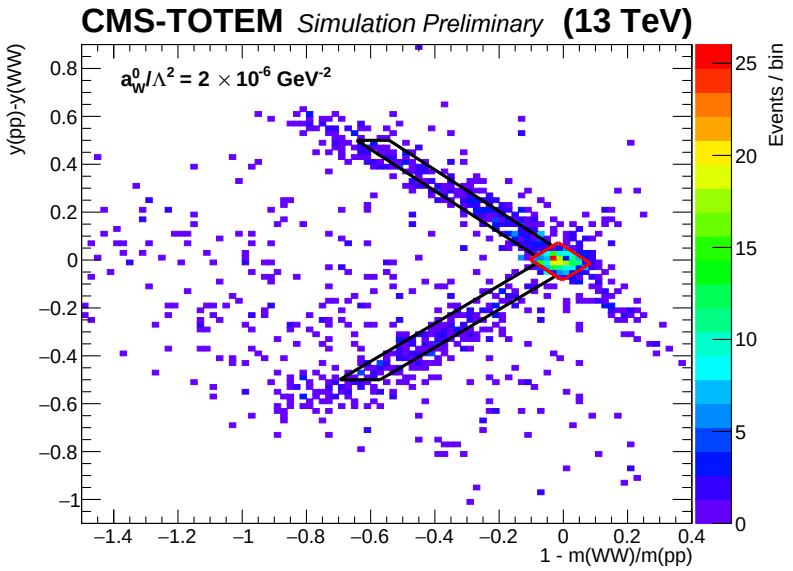

Figure 6.4: Matching between the jets and protons, in invariant mass and rapidity, for simulated signal events in the WW region of pruned masses. The diamond-shaped area near the axis origin (signal region δ) corresponds to the case where both protons are correctly matched to the jets. The diagonal bands (signal region o) correspond to the case where one proton is correctly matched, and the second proton originates from a pileup interaction.

dijet-proton matching requirements, to define 3 independent sideband regions. Region C has $a < 0.01$, and $|1 - m(WW)/m(pp)| > 1.0$ or $|y(pp) - y(WW)| > 0.5$. Region B is defined by $a > 0.01$, with the signal region selection applied in $|1 - m(WW)/m(pp)|$ and $|y(pp) - y(WW)|$. Region D is defined by $a > 0.01$, and $|1 - m(WW)/m(pp)| > 1.0$ or $|y(pp) - y(WW)| > 0.5$. If the numbers of events in each of these regions are N_{A}, N_{C}, N_{B}, and N_{D}, respectively, the number of events in the signal region is then estimated as $N_{\mathrm{A}} = N_{\mathrm{C}} \times N_{\mathrm{B}}/N_{\mathrm{D}}$. Here $N_{\mathrm{B}}/N_{\mathrm{D}}$ estimates the fraction of background events in the dijet-proton matching region. This number does not depend on the dijet acoplanarity requirement, therefore it is estimated in the anti-acoplanarity sideband, and N_{C} provides the normalization to determine the expected background when the acoplanarity cut is imposed.

The distribution of the data in these regions is illustrated for the

2018 sample with the WW selection in Fig. 6.5. A comparison between data selected with the acoplanarity requirement $a > 0.01$ (referred to as anti-acoplanarity region/method in the following) and the predicted background from simulation is shown in Fig. 6.6 for each of the years and in both the WW and ZZ mass regions. In general, data and simulation agree within uncertainty, apart from a small excess at low masses in the 2016 WW sample. Since the final background estimate is obtained entirely from the data, such minor discrepancies do not impact the results.

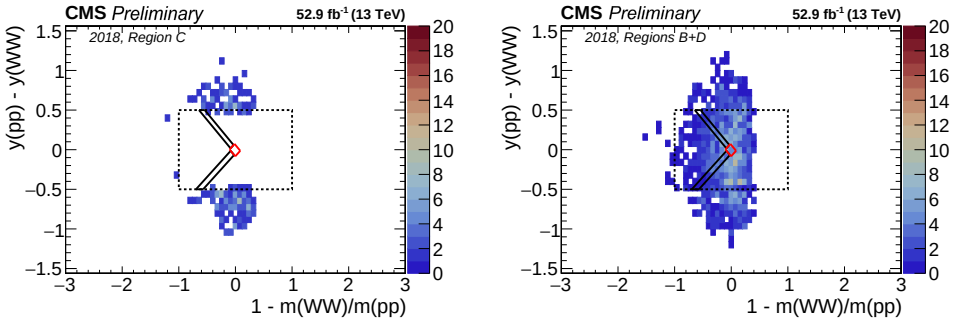

Figure 6.5: Distribution of the 2018 data in the $y(pp) - y(VV)$ vs. $1 - m(VV)/m(pp)$ plane in the WW mass region. On the left, the normalization sample is shown, where all selections are applied, except that the region inside the dashed lines remains blinded. On the right, the anti-acoplanarity region is shown, where the acoplanarity requirement is inverted to select a background-dominated sample. The solid lines indicate the same signal regions as shown in Fig. 6.4. In the right plot the area inside the solid lines corresponds to "Region B", while the area outside the dashed lines corresponds to "Region D".

As an alternative background model, the same procedure was applied inverting the selection on the pruned masses ($m < 60$ GeV or $m > 107$ GeV) of both jets, rather than that on the acoplanarity.

Finally, as a cross check, the background was also estimated using an event-mixing approach. In background events, the simulated output of the central detectors is mixed with protons from real data, randomly extracted from the jet-triggered data sample. In a toy Monte Carlo approach, this procedure is repeated 1000 times, and the event selection is applied. The mean and RMS of the distribution of events passing the selection in toy experiments are taken as the background estimate and its

uncertainty. This procedure has the drawback of relying on simulation for the central jet samples, and explicitly assumes that the protons always originate from different interactions than the jets. For these reasons, it is not used in the final background estimate, but only as an independent cross check.

The resulting background estimates and statistical uncertainties are shown in Tables 6.1 - 6.2, for all years and signal regions, for both the default anti-acoplanarity method and the alternative anti-pruned mass method. In these data-driven approaches, the main component of the statistical uncertainty is given by the limited number of events in data for the region failing the central detector selections ("Region B") but passing the dijet-proton matching. The results of the event mixing method are also shown, with statistical uncertainties driven by the limited number of simulated QCD events.

In general, the estimates of the different methods agree within the statistical uncertainties. All methods show that the background is dominated by QCD multijet production, with contributions from other backgrounds $\leq 8\%$ of the total. The background levels in 2018 are much larger than for the other years, as a consequence of the increased luminosity and the PPS capability of reconstructing multiple multi-RP protons per event thanks to the PPS pixel detectors. The latter, despite the increase in background tracks, significantly improves the signal efficiency as well.

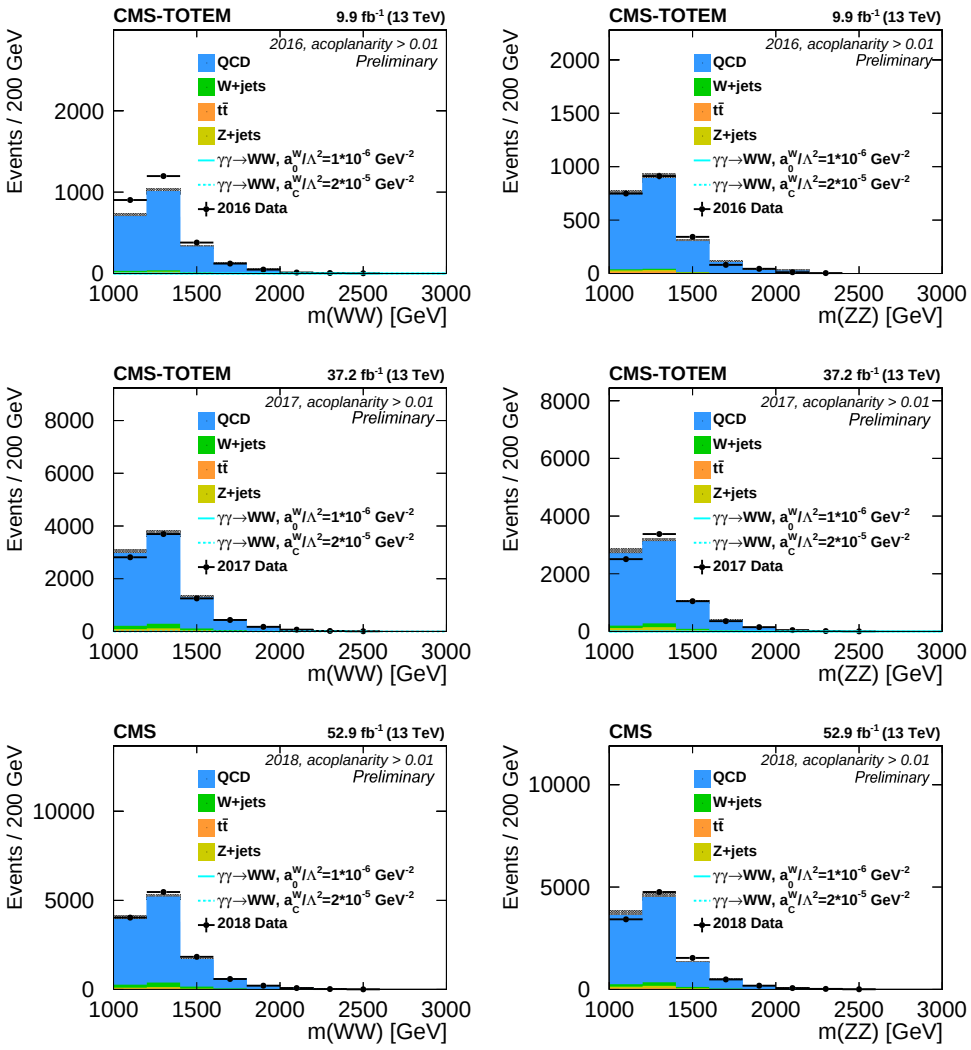

Figure 6.6: Diboson invariant mass distributions in data and simulation in the anti-acoplanarity region ($a > 0.01$), with no requirement on the proton matching. The plots from top to bottom are for the 2016, 2017, and 2018 data, respectively, with the WW region in the left column and the ZZ region in the right column. Only statistical uncertainties are shown.

Background method	Region	Bkg. ± stat. (2016)	Bkg. ± stat. (2017)	Bkg. ± stat. (2018)
Anti-acoplanarity sideband	δ	0.4 ± 0.4	1.6 ± 1.0	11.6 ± 2.6
Anti-pruned mass sideband	δ	0.5 ± 0.2	1.5 ± 0.3	11.3 ± 0.8
Event mixing	δ	0.5 ± 0.9	1.8 ± 3.2	14.3 ± 8.9
Expected signal ($a_0^W/\Lambda^2 = 5 \times 10^{-6}$ GeV^{-2})	δ	1.7	2.2	16.1
Anti-acoplanarity sideband	o	1.4 ± 0.9	10.0 ± 3.2	41.4 ± 5.7
Anti-pruned mass sideband	o	2.5 ± 0.8	7.1 ± 1.3	43.0 ± 3.0
Event mixing	o	2.4 ± 1.9	8.4 ± 6.3	49.3 ± 12.9
Expected signal ($a_0^W/\Lambda^2 = 5 \times 10^{-6}$ GeV^{-2})	o	1.5	1.7	16.8

Table 6.1: Background predictions from all methods, for the WW signal regions with fully ("region δ") and partially ("region o") reconstructed events. The mean value of the expected signal for one anomalous coupling point ($a_0^W/\Lambda^2 = 5\times10^{-6}$ GeV^{-2}) is also shown for comparison.

Background method	Region	Bkg. ± stat. (2016)	Bkg. ± stat. (2017)	Bkg. ± stat. (2018)
Anti-acoplanarity sideband	δ	1.5 ± 1.1	1.6 ± 0.8	14.2 ± 3.0
Anti-pruned mass sideband	δ	0.4 ± 0.2	0.9 ± 0.2	9.9 ± 0.9
Event mixing	δ	0.5 ± 0.9	1.5 ± 2.8	11.6 ± 9.4
Expected signal ($a_0^Z/\Lambda^2 = 1 \times 10^{-5}$ GeV^{-2})	δ	1.3	1.4	9.0
Anti-acoplanarity sideband	o	1.5 ± 1.1	3.7 ± 1.5	37.4 ± 5.6
Anti-pruned mass sideband	o	2.1 ± 0.8	5.4 ± 1.3	41.7 ± 3.1
Event mixing	o	2.0 ± 1.8	6.3 ± 5.1	42.0 ± 15.5
Expected signal ($a_0^Z/\Lambda^2 = 1 \times 10^{-5}$ GeV^{-2})	o	1.0	1.6	12.8

Table 6.2: Background predictions from all methods, for the ZZ signal regions with fully ("region δ") or partially ("region o") reconstructed events. The mean value of the expected signal for one anomalous coupling point ($a_0^Z/\Lambda^2 = 1 \times 10^{-5}$ GeV^{-2}) is also shown for comparison.

6.5 Systematic uncertainties

The experimental systematic uncertainties on the signal prediction take into account the jet energy scale, proton ξ reconstruction, proton reconstruction efficiency, and luminosity.

The effect of the jet energy scale is evaluated by shifting the energy of both jets in the event up or down by the uncertainty, and recomputing the expected signal yields. This uncertainty accounts for the effects of pileup, uniformity of the detector response, and further data/MC discrepancies, measured on well-known event topologies. The resulting uncertainties on event yields depend on the data-taking era and sample, but typically range from a few percent up to 10%.

The proton ξ reconstruction systematics are uncorrelated between the two arms. The effect of this uncertainty is evaluated by shifting the value of ξ of each simulated signal proton by an amount drawn from a gaussian distribution with width equal to the uncertainty, and recomputing the expected signal yield. Systematic uncertainties on the proton ξ account for effects induced by perturbations on the PPS detector alignment and optics. The details concerning the systematics treatment are discussed in Ref. [2]. The PPS direct simulation already accounts for ξ reconstruction bias (systematic difference from MC truth) and resolution. The alignment and optics are although determined with non-negligible uncertainties that propagate to ξ. Such effects are estimated by perturbating the alignments and optical functions (Eq. 4.3), and are combined in quadrature. Figure 6.7 shows the proton reconstruction uncertainties as a function of ξ. The "systematics" component corresponds to a relative uncertainty in the 7–9% range. Because of the tight matching requirements between protons and jets, the ξ uncertainty is one of the largest systematic uncertainties in the analysis, with values typically of the order of 30%.

The uncertainties related to the proton reconstruction efficiency are based on comparing results obtained with different control samples and efficiency estimation procedures. The total efficiency uncertainty per arm is 10.0% in 2016; in 2017 and 2018 the improved detectors and methods

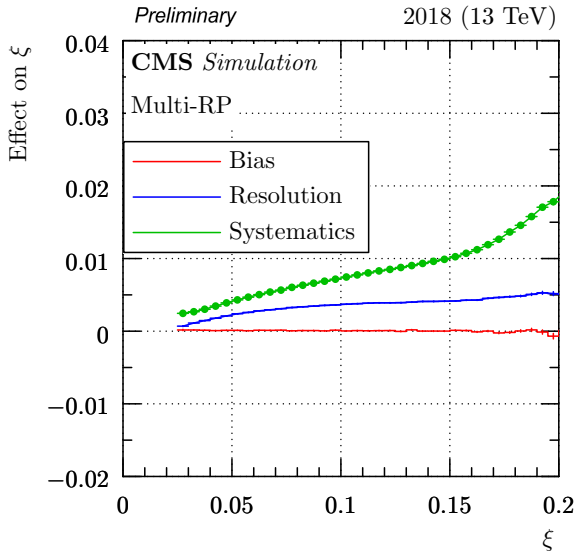

Figure 6.7: Multi-RP proton bias, resolution and systematics characteristics as a function of ξ (2018 pre-TS1, sector 56). The systematic uncertainty curve represents the combination of all contributions. Figure from Ref. [2].

led to uncertainties between 2.1% and 2.8% per arm. The efficiency uncertainties for the two arms are taken to be uncorrelated and are summed in quadrature to obtain the event uncertainty.

The luminosity uncertainties are taken as 1.2% [118], 2.3% [119], and 2.5% [120] for the 2016, 2017, and 2018 samples, respectively.

The theoretical uncertainty in the signal prediction includes contributions from the simulation statistics and from the rapidity gap survival probability, i.e. the probability that the rapidity gaps between the scattered protons and the jets are not filled by particles produced by soft interactions between the spectator partons of the colliding protons. The statistical uncertainty in the simulation is typically below 10%. The uncertainty in the survival probability is taken to be 10% [136].

The background systematic uncertainties consist of two parts. The first is the statistical uncertainty in the normalization, based on the nominal acoplanarity sideband method. The second is the dependence of the background estimate on the choice of the sideband region. This is conservatively taken as the full difference between the central values of the

acoplanarity sideband method and the pruned mass sideband method. The first uncertainty depends mainly on the statistics of the available sideband data; it is in the range $\sim$ 15–20% in the 2018 data, up to $>$ 100% in the 2016 data, where the integrated luminosity is low. The second uncertainty also has a significant statistical component, which ranges from a few percent in the 2018 data, to 80% in the 2016 data.

6.6 Signal extraction and results

The signal is extracted in twelve bins: one for each year of data, times two for the WW and ZZ regions, times two for the two signal regions (δ and o). Systematic uncertainties are in most cases accounted for as log-normal nuisance parameters. Systematic uncertainties related to statistics are treated as Poisson nuisances when the sample has less than 10 events. This applies to some of the background statistical uncertainties derived from sideband regions, and some of the simulation statistical errors for very small couplings. The signal is estimated for each of the anomalous couplings, with all other couplings fixed to zero.

Figure 6.8 shows the number of observed events compared to the expectation of background and a hypothetical signal, in each bin of the analysis. The backgrounds and observed data are compared to a signal with non-zero WW anomalous couplings, slightly above the expected sensitivity of the analysis. Small ($\leq 1\sigma$) excesses are seen in "region o" of the WW for all years, while small deficits are seen in the ZZ channel. None of these excesses or deficits in the data are significant.

6.6.1 AQGC limits on dimension-6 operators

The resulting expected and observed 95% CL upper limits on dimension-6 AQGC operators are shown in Figure 6.9 and are obtained with a binned fit to the above-mentioned twelve signal regions.

In order to account for unphysically growing cross section at high masses, which eventually causes a unitarity violation, the so-called *clip-*

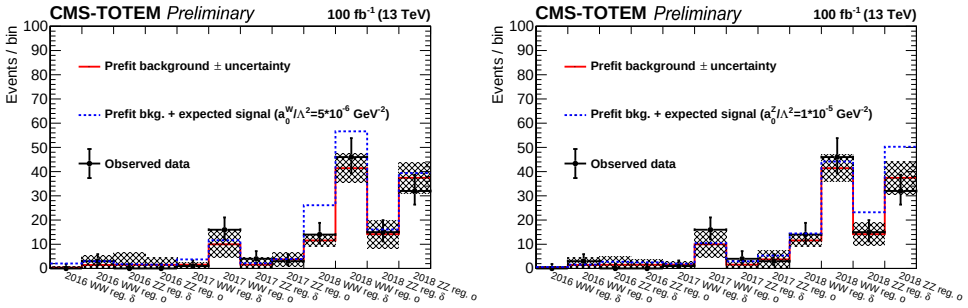

Figure 6.8: Observed data and expected number of background events in each signal region. Hypothetical AQGC signals are also shown. The histogram with solid lines indicates the number expected for only background, with uncertainties shown by the shaded band. The dashed-line histogram shows the number for background plus assumed signals with $a_0^W/\Lambda^2 = 5 \times 10^{-6}$ GeV^{-2} (left) or $a_0^Z/\Lambda^2 = 1 \times 10^{-5}$ GeV^{-2} (right).

ping procedure is applied [44]. It consists in calculating the energy at which unitarity is violated for the expected limits and removing the simulated anomalous signal events above that threshold. The limits are then re-derived, with the clipping applied.

In the WW channel, unitarity violation occurs at approximately 1.4 TeV for both of the couplings. By clipping the signal model at that value, new expected limits are obtained, that are approximately 40% higher than the unitarity violating limits. In the ZZ channel, unitarity violation occurs at approximately 1.1 TeV for both of the couplings. In this case, because of the invariant mass threshold imposed by the jet triggers, there is no value of clipping for which unitarity is preserved. The full list of 95% CL upper limits with and without clipping is shown in Table 6.3.

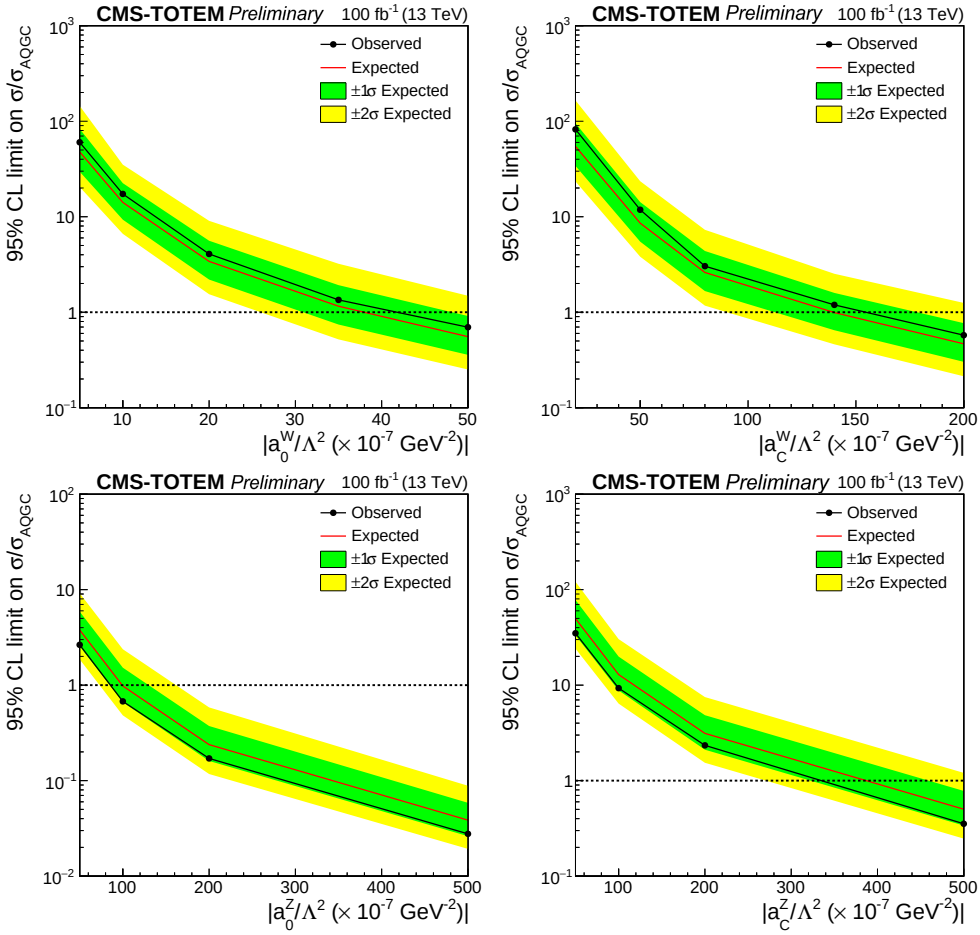

Figure 6.9: Expected and observed upper limits on the AQGC operators a_0^W/Λ^2 (upper left), a_C^W/Λ^2 (upper right), a_0^Z/Λ^2 (lower left), a_C^Z/Λ^2 (lower right), with no unitarization. The y axis shows the limit on the ratio of the observed cross section to the cross section predicted for each anomalous coupling value (σ_{AQGC}).

Coupling	Observed (expected) 95% CL upper limit No clipping	Observed (expected) 95% CL upper limit Clipping at 1.4 TeV
$\lvert a_0^W/\Lambda^2\rvert$	4.3 (3.9) $\times 10^{-6}$ GeV^{-2}	5.2 (5.1) $\times 10^{-6}$ GeV^{-2}
$\lvert a_C^W/\Lambda^2\rvert$	1.6 (1.4) $\times 10^{-5}$ GeV^{-2}	2.0 (2.0) $\times 10^{-5}$ GeV^{-2}
$\lvert a_0^Z/\Lambda^2\rvert$	0.9 (1.0) $\times 10^{-5}$ GeV^{-2}	-
$\lvert a_C^Z/\Lambda^2\rvert$	4.0 (4.5) $\times 10^{-5}$ GeV^{-2}	-

Table 6.3: Limits on dimension-6 anomalous quartic gauge coupling parameters, with and without unitarization via the clipping procedure.

The limits are also shown in the two-dimensional plane of a_C^W/Λ^2 vs. a_0^W/Λ^2 and a_C^Z/Λ^2 vs. a_0^Z/Λ^2, by fitting the signal strength limits to an analytical model for the dependence of the cross section on the AQGC values. The results are shown in Fig. 6.10. The a_C^W/Λ^2 vs. a_0^W/Λ^2 are shown with and without clipping the signal model at 1.4 TeV. Compared to the unitarized limits obtained for $|a_0^W/\Lambda^2|$ and $|a_C^W/\Lambda^2|$ with LHC Run 1 data [137, 138], the unitarized limits derived here present an improvement of a factor $\sim$ 15–20.

The unitarization procedure naturally makes the limits less stringent. It is worth noticing, however, that in the analysis with proton tagging the effect is inferior than that observed in the results of Run 1 analyses, which showed limit variations of about two orders of magnitude. This is explained by the fact that the proton acceptance requirement imposes an upper limit on the mass of the central system. This acts like a built-in clipping cut, while in analyses without protons the upper limit is only defined by the collision energy provided by the LHC. The dependence on high-mass events is thus limited when requiring protons in the PPS acceptance, and therefore limits are less affected by the clipping procedure.

6.6.2 Translation to linear dimension-8 AQGCs

As many recent anomalous coupling studies quote limits on dimension-8 linear operators only, a translation to that operator basis is hereby presented to generalise the results. In the case of processes involving photons, the $a_{0,C}^{W,Z}$ operators couplings can be translated into a linear combination of dimension-8 $f_{M,i}(i = 0 - 7)$ couplings [139]. In the case of the a_0^W coupling, the relationship reads [139]:

$$a_0^W = -\frac{M_W}{\pi\alpha_{\text{em}}}[s_w^2\frac{f_{M,0}}{\Lambda^2} + 2c_w^2\frac{f_{M,2}}{\Lambda^2} + s_w c_w\frac{f_{M,4}}{\Lambda^2}] \tag{6.1}$$

Here M_W is the W boson mass, α_{em} is the fine structure constant, and s_w and c_w represent the sine and cosine of the weak mixing angle (θ_W), respectively.

By further assuming that anomalous contributions to $WWZ\gamma$ vanish,

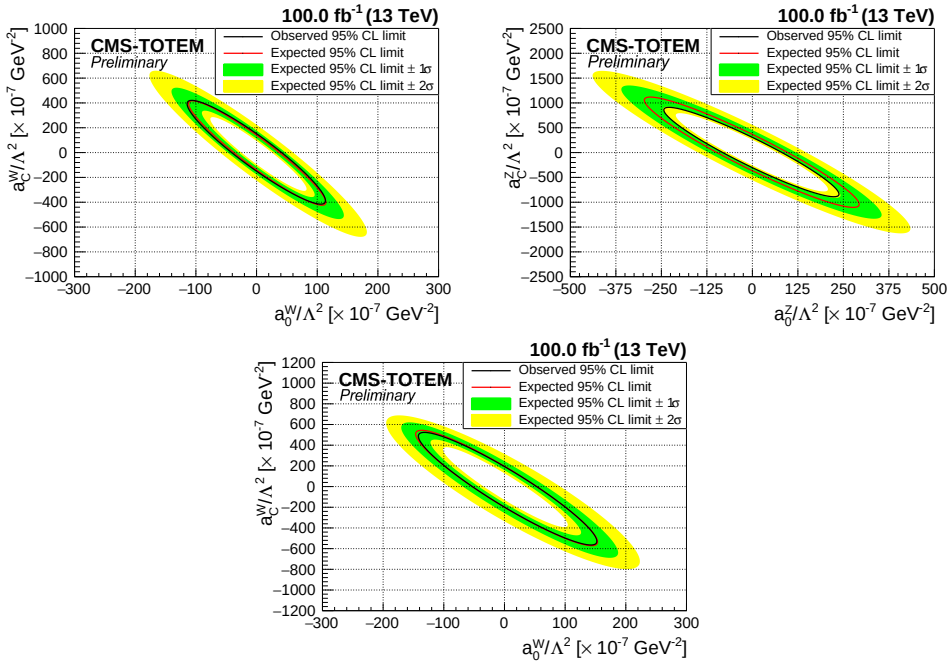

Figure 6.10: Expected and observed limits in the two-dimensional plane of a_C^W/Λ^2 vs. a_0^W/Λ^2 (above left), a_C^Z/Λ^2 vs. a_0^Z/Λ^2 (above right), and a_C^W/Λ^2 vs. a_0^W/Λ^2 with unitarization imposed by clipping the signal model at 1.4 TeV (below).

an additional constraint of $f_{M,0} + 2 \times f_{M,2}$ is obtained [140, 141], allowing a_0^W to be written in terms of only $f_{M,0}$ and $f_{M,4}$. In order to compare to other results, we scan the values of $f_{M,0}$ and $f_{M,4}$ for which the limit on a_0^W is satisfied. The results shown in Table 6.4 are thus found, evaluated at the point where the other coupling is zero.

Alternatively, all dimension-8 $f_{M,i}$ except one may be set equal to zero. This is another common procedure when presenting dimension-8 operator couplings. In this case, the results of the conversion are shown in Table 6.5.

Coupling	Observed (expected) 95% CL upper limit No clipping	Observed (expected) 95% CL upper limit Clipping at 1.4 TeV
$\lvert f_{M,0}/\Lambda^4\rvert$	16.2 (14.7) TeV^{-4}	19.5 (19.2) TeV^{-4}
$\lvert f_{M,4}/\Lambda^4\rvert$	90.9 (82.6) TeV^{-4}	110 (108) TeV^{-4}

Table 6.4: Conversion of limits on a_0^W to dimension-8 $f_{M,i}$ operators, using the assumption of vanishing $WWZ\gamma$ couplings to eliminate some parameters. When quoting limits on one of the operators, the other is fixed to zero. The results for $|f_{M,0}/\Lambda^4|$ and $|f_{M,4}/\Lambda^4|$ are shown with and without clipping of the signal model at 1.4 TeV, when the other parameter is fixed to the SM value of zero.

Coupling	Observed (expected) 95% CL upper limit No clipping	Observed (expected) 95% CL upper limit Clipping at 1.4 TeV
$\lvert f_{M,0}/\Lambda^4\rvert$	66.0 (60.0) TeV^{-4}	79.8 (78.2) TeV^{-4}
$\lvert f_{M,1}/\Lambda^4\rvert$	245.5 (214.8) TeV^{-4}	306.8 (306.8) TeV^{-4}
$\lvert f_{M,2}/\Lambda^4\rvert$	9.8 (9.0) TeV^{-4}	11.9 (11.8) TeV^{-4}
$\lvert f_{M,3}/\Lambda^4\rvert$	73.0 (64.6) TeV^{-4}	91.3 (92.3) TeV^{-4}
$\lvert f_{M,4}/\Lambda^4\rvert$	36.0 (32.9) TeV^{-4}	43.5 (42.9) TeV^{-4}
$\lvert f_{M,5}/\Lambda^4\rvert$	67.0 (58.9) TeV^{-4}	83.7 (84.1) TeV^{-4}
$\lvert f_{M,7}/\Lambda^4\rvert$	490.9 (429.6) TeV^{-4}	613.7 (613.7) TeV^{-4}

Table 6.5: Conversion of limits on a_0^W and a_C^W to dimension-8 $f_{M,i}$ operators, using the assumption that all $f_{M,i}$ except one are equal to zero. The results are shown with and without clipping of the signal model at 1.4 TeV.

These results may be compared to other vector boson scattering studies at 13 TeV, which are sensitive to the same operators [142]. When the conversion is performed assuming vanishing $WWZ\gamma$ couplings, the unitarity violating limits on $|f_{M,0}/\Lambda^4|$ and $|f_{M,4}/\Lambda^4|$ are several times looser than those quoted in other measurements. After the clipping, the results for $|f_{M,0}/\Lambda^4|$ are similar to the best limits obtained from vector boson scattering in the same sign $W^{\pm}W^{\pm}$ and WZ final states in CMS [44].

When the conversion is performed by setting all other couplings to zero, the limits on $|f_{M,0}/\Lambda^4|$ are significantly looser, the limits on $|f_{M,4}/\Lambda^4|$ are somewhat more restrictive, and tight constraints are obtained on $|f_{M,2}/\Lambda^4|$.

6.6.3 Fiducial cross sections

In addition to the limits on different anomalous coupling parameters, we derive upper limits on the cross section for an AQGC-like signal in the $pp \to pWWp$ and $pp \to pZZp$ channels. These limits provide an alternative input for theory studies in case of a signal similar to AQGC, but not mapped to EFT operators.

The limits are obtained for a fiducial region of $0.04 < \xi < 0.20$ and $m > 1$ TeV, and correspond to the diboson production cross section before the decay into hadrons. As with the AQGC limits, the cross section limits are obtained for each channel separately, assuming zero signal in the other. After verifying that the signal efficiency and acceptance do not depend strongly on the exact value of the AQGCs, we find at 95% CL:

$$\sigma(pp \to pWWp)_{0.04<\xi<0.20, m>1000\ \text{GeV}} < 67(53^{+34}_{-19})\ \text{fb},$$

$$\sigma(pp \to pZZp)_{0.04<\xi<0.20, m>1000\ \text{GeV}} < 43(62^{+33}_{-20})\ \text{fb},$$

where the expected limit and 1σ uncertainty is shown in parentheses.

Summary and conclusions

This thesis presents the research work I performed during the LHC Long Shutdown 2 in the context of the Precision Proton Spectrometer of the CMS experiment. Specifically, I studied the performance of the tracking detectors with Run 2 data and I worked on the preparation of the new tracker for Run 3. In parallel, I contributed to the analysis of WW/ZZ central exclusive production with protons measured in PPS.

Central exclusive production processes are events in which two protons scatter off each other, producing a central state and losing part of their energy in the collision. The PPS consists of tracking and timing detector stations installed in mechanical structures called Roman Pots. When the RPs are inserted, the detectors approach the LHC beam down to $\sim$ 1.3 mm and measure protons that, because of the energy they lost in the interaction, are deviated outside the beam envelope by the LHC magnets.

The detector successfully collected an integrated luminosity higher than 100 fb^{-1} during the Run 2 data-taking (2016-2018) and will take part to Run 3 (2022-2025).

This thesis focuses on the PPS tracking detectors. In Run 2, double-sided 3D silicon pixel sensors produced by CNM were used, and were read out with the PSI46dig ROC developed for the CMS pixel tracked Phase I upgrade. This radiation-hard technology was a key requirement for the data-taking success, as PPS detectors are exposed to extremely high and non-uniform irradiation ($\sim 5 \cdot 10^{15}$ p/cm^2 estimated for the whole Run 2 data-taking). While the sensors tolerated well the irradiation, efficiency loss in the readout chips due to non-uniform irradiation was observed.

The radiation damage throughout the Run 2 data-taking was studied and characterized, showing that tracking stations achieved an average efficiency higher than 98%, and the damage was largely contained in a small spot close to the beam.

It was proven that shifting vertically the detector stations, by installing calibrated shims during Technical Stops, was an effective strategy for improving the tracking station performance. This approach granted an almost complete recovery of the efficiency in the highest occupancy spot, greatly improving the detector performance in that region for some time.

Studying the proton reconstruction techniques developed in PPS, the effect of the tracking detector efficiency on the reconstruction performance was estimated. The reconstruction efficiency of multi-RP protons, i.e. protons measured in both stations of a LHC sector, was studied, showing that the usage of a tracker fully based on pixel detectors is beneficial for the PPS physics case. This is because the fraction of events with multiple proton tracks, which cannot be reconstructed with the legacy TOTEM strip detectors, is large and thus generates a sizeable efficiency loss that ranges from 20% to 60% (depending on pileup).

A new tracker for the forthcoming Run 3 has been prepared, with new 3D silicon pixel detectors produced by FBK. The new sensors, produced with single-sided processing, have the same pixel pitch as their Run 2 counterpart and lower thickness (150 μm vs. 230 μm). They were bump-bonded to PROC600v4 chips, the same used in the innermost layer of the CMS pixel tracker barrel, and the PPS DAQ system has been updated to comply with the new readout. An extensive set of integration tests has been performed to ensure the detector readiness for installation.

The pixel detector mechanics were also upgraded for Run 3, now including a stepper motor that allows for vertical movements in the RP box to take place. A dedicated remote control system was designed to fit the already available infrastructures in the LHC tunnel. The system was tested at the CERN North Area facilities and later installed in the tunnel. This innovative solution will be used to spread the irradiation

across the pixel detectors, effectively improving their performance and extending their lifetime.

A new framework for the real-time calibration of PPS detectors during data-taking was developed. The system, based on CI/CD commercial tools, extends the functionality of the framework designed for the ECAL detector, improving its flexibility and automation capabilities. This framework will allow for automatic calibrations to be executed and will provide adequate tools for their monitoring during data-taking.

The Run 3 pixel detector has been installed recently. It is currently under commissioning, and will soon be integrated in the CMS central DAQ.

Finally, using data samples collected in the CMS Run 2, corresponding to 100 fb^{-1} integrated luminosity, a search for Anomalous Quartic Gauge Couplings (AQGC) has been carried out. The search focuses on the central exclusive production of high-mass vector boson pairs and uses the proton information to identify event candidates. The studied decay channel requires both vector bosons to decay in a pair of quarks, which are reconstructed in the CMS central detectors as a single large-radius jet.

The search found no excess with respect to the Standard Model prediction, and upper limits on AQGC effective field theory operators have been set. Limits are presented both in terms of dimension-6 and dimension-8 operators. Upper limits on the $pp \to pWWp$ and $pp \to pZZp$ production cross sections, in a fiducial region within the detector acceptance, have also been determined.

The dimension-6 unitarized AQGC limits improve by a factor $\sim$ 15–20 the ones obtained in the LHC $pp \to pWWp$ search at $\sqrt{s} = 8$ TeV. The converted dimension-8 limits are, for some operators, close to those obtained from same-sign WW and WZ scattering at $\sqrt{s} = 13$ TeV.

Acknowledgements

First of all, I wish to thank my tutor and co-tutor, Prof. A. M. Solano and Prof. M. Obertino, for guiding me through these years. I thank the Università degli Studi di Torino and the INFN Sezione di Torino for the financial support during my PhD and the time spent at CERN.

I want to warmly thank all my PPS colleagues, and in particular N. Minafra, V. Avati, E. Bossini, N. Turini, D. Figueiredo, J. Kaspar, not only for being great work partners, also for being there as friends, always ready with a word of advice when needed. We have known each other for a long time now and I hope to keep working with you in the future!

I am grateful to the whole PPS Tracker Group. E. Robutti, F. Ferro, M. Arneodo, and my tutors, thanks for putting up with my long detailed (and probably boring) presentations. Seeing the preparation of the new tracker for Run 3 converge, even through many difficulties, feels satisfying and rewarding for the hard work that we all put into it. I also want to thank A. Modak, D. Kotlinski and F. Ravera for the extremely useful exchanges we had concerning our pixel detector.

I wish to say thank you to my VV analysis friends and colleagues, K. Shchelina and J. J. Hollar, I learnt a lot about analysis from you and, even if we did not find our dark penta-quark in the end, it was a fun journey and an great learning opportunity. Thanks for allowing me to join the analysis team, for the fun online and (finally!) real-life meetings, and for all the help you gave me throughout this work. I will keep bringing food to CERN to bring good luck on us!

I want to thank L. Grzanka and the AGH University summer students,

in particular L. Kita, C. Misan and A. Wolk. I will not forget the fun we had, hiking together and having fruitful conversations about IT and physics together. I hope to keep learning tricks from Leszek and to see the great work that we did on the PPS calibration tools come to life in Run 3! Working with and coordinating Lukasz and Arek has been a really fun experience, which I hope was pleasurable for them too. It is indeed proof that exchanges between different fields can be beneficial, not only for the students, but also for tutors.

I am grateful to my Kansas University colleagues Prof. C. Royon and C. Baldenegro, for your guidance in the phenomenology study we did on anomalous exclusive $t\bar{t}$ production, and especially for all the inspiring conversations that we had. They always gave me food for thought for future studies which I hope to pursue sometime in the future.

I am also grateful to my colleague/buddies: Oriol, Marta, Federico, Luca, Jacopo, Alessandra, Gaia. We had a great time together, unfortunately much less than what it could have been without Covid, and I hope to make up for it in the future!

Finally, I wish to thank my closest friends, Andrea, Carlo, Edoardo, Fede and Mery, Lollo and Vale, Romeo and Chiara. I could not desire a better group of friends than you guys. I know that putting up with all my unexpected trips, absences and random schedules must have been at times nerve-wracking, and I really appreciate that you did. I wish the future will be a bit more relaxed and easy to foresee, and hope to keep spending my time with you having fun (and adventures).

I want to deeply thank my parents and "la nonna": throughout these years you have supported me, helped me, and tolerated everything about me. It still amazes me seeing how you manage to juggle all the work you do with all the rest, still having time for everybody else. I definitely have a lot to learn from you, probably I always will. I cannot say thank you enough for always being there for me.

Even if it might be a hard concept for them to grasp, I am really grateful to Lea and Allis, the two ferocious beasts (adorable irish setters) that kept me company during these years. Saying goodbye to the first

has not been easy as saying welcome to the second, but I will never forget the time spent with you during these years. The ways you always had to make me laugh and get my head off of work were endless, and I am thankful for that.

It would take a whole other document of this length to express why I am thankful to Giulia, my sweetheart. I cannot help but admire you for staying beside me in this journey, with all its ups and downs, and the long time spent apart. You always managed, somehow, to help me look at the bright side of things and push forward, something that often I am not that good at doing. I cannot say thank you enough for that.
I will forever keep with me the memory of our unexpected journey through the Alps to get to St. Genis, when you came visiting me and I picked you up at the Montgenèvre border to comply with the crazy Covid rules.
I hope to have you by my side through every adventure the future will put us through. I would not dare thinking of a better companion than you. I will keep striving to be better for you, to save more time for us, and I promise that I will be there for you, as you did for me.

I really hope not to have forgotten anybody in these acknowledgments and if I did, please know that it was not on purpose. I have not met a single person during these years who is not worth saying thank you.

Coming to things I do not thank, without making a dedicated chapter: Covid, you piece of garbage (not to say worse). Not only you are the reason why mango tastes like water now, thanks to you the world turned upside down. You made travelling impossible, human contact scary, and working much harder. All of this would have been easier without you, but I guess that there was not a lot of choice. I will do my best not to remember about you!

Anyway, thanks everybody (except Covid) and that's all folks!

Bibliography

[1] CMS Collaboration, "Efficiency of the Pixel sensors used in the Precision Proton Spectrometer: radiation damage", CMS Detector Performance Summary CERN-CMS-DP-2019-036, CERN, 2019.

[2] CMS and TOTEM Collaborations, "Proton reconstruction with the CMS Precision Proton Spectrometer in Run 2", CMS Physics Analysis Summary CMS-PAS-PRO-21-001, TOTEM-NOTE-2022-001, Geneva: CERN, 2022.

[3] CMS and TOTEM Collaborations, "Search for exclusive $\gamma\gamma \to$ WW and $\gamma\gamma \to$ ZZ production in final states with jets and forward protons", Geneva: CERN, 2022.

[4] CMS Collaboration, "Exclusive photon-photon production of muon pairs in proton-proton collisions at $\sqrt{s} = 7$ TeV", *JHEP* **01** (2012) 052.

[5] CMS Collaboration, "Study of Exclusive Two-Photon Production of W^+W^- in pp Collisions at $\sqrt{s} = 7$ TeV and Constraints on Anomalous Quartic Gauge Couplings", *JHEP* **07** (2013) 116.

[6] CMS Collaboration, "Evidence for exclusive $\gamma\gamma \to W^+W^-$ production and constraints on anomalous quartic gauge couplings in pp collisions at $\sqrt{s} = 7$ and 8 TeV", *JHEP* **08** (2016) 119.

[7] CMS Collaboration, "Study of central exclusive $\pi^+\pi^-$ production in proton-proton collisions at $\sqrt{s} = 5.02$ and 13 TeV", *Eur. Phys. J. C* **80** (2020) 718.

[8] U. Amaldi et al., "40th Anniversary of the First Proton-Proton Collisions in the CERN Intersecting Storage Rings (ISR)", *CERN Yellow Reports: Conference Proceedings* (2012).

[9] L. Baksay et al., "Measurement of the Proton Proton Total Cross-Section and Small Angle Elastic Scattering at ISR Energies", *Nucl. Phys. B* **141** (1978) 1–28, erratum: *Nucl.Phys.B* 148 (1979) 538–539.

[10] A. Brandt et al., "The Small angle spectrometer of experiment UA8 at the S$p\bar{p}$S collider", *Nucl. Instrum. Meth. A* **327** (1993) 412–426.

[11] ZEUS Collaboration, "The ZEUS Leading Proton Spectrometer and its use in the measurement of elastic ρ^0 photoproduction at HERA", *Z. Phys. C* **73** (1997) 253–268.

[12] P. van Esch et al., "The H1 forward proton spectrometer at HERA", *Nucl. Instrum. Meth. A* **446** (2000) 409–425.

[13] A. Santoro, "Forward proton detector on D0 experiment", *Braz. J. Phys.* **30** (2000) 362–369.

[14] M. Gallinaro, "CDF Forward Detectors and diffractive structure functions at the Fermilab Tevatron", *arXiv:hep-ph/0407255* (2004).

[15] S. Bultmann et al., "The PP2PP experiment at RHIC: Silicon detectors installed in Roman Pots for forward proton detection close to the beam", *Nucl. Instrum. Meth. A* **535** (2004) 415–420.

[16] CMS and TOTEM Collaborations, "CMS-TOTEM Precision Proton Spectrometer", Technical Design Report CERN-LHCC-2014-021, TOTEM-TDR-003, CMS-TDR-13, CERN, 2014.

[17] ATLAS Collaboration, "Technical Design Report for the ATLAS Forward Proton Detector", ATLAS Physics Analysis Summary, Geneva: CERN, 2015.

[18] CMS Collaboration, "The CMS Precision Proton Spectrometer at the HL-LHC – Expression of Interest", CMS Note CERN-CMS-NOTE-2020-008, Geneva: CERN, 2020.

[19] V. Khoze, A. Martin, and M. Ryskin, "Prospects for new physics observations in diffractive processes at the LHC and Tevatron", *Eur. Phys. J. C* **23** (2002) 311–327.

[20] CMS and TOTEM Collaborations, "Observation of proton-tagged, central (semi)exclusive production of high-mass lepton pairs in pp collisions at 13 TeV with the CMS-TOTEM Precision Proton Spectrometer", *JHEP* **2018** (2018) 153.

[21] CMS and TOTEM Collaborations, "Search for central exclusive production of top quark pairs in proton-proton collisions at $\sqrt{s} =$ 13 TeV with tagged protons", CMS Physics Analysis Summary CMS-PAS-TOP-21-007, TOTEM-NOTE-2022-002, Geneva: CERN, 2022.

[22] CMS Collaboration, "Identification of heavy-flavour jets with the CMS detector in pp collisions at 13 TeV", *JINST* **13** (2018) P05011.

[23] CMS Collaboration, "Measurements of $\mathrm{t\bar{t}}$ differential cross sections in proton-proton collisions at $\sqrt{s} = 13$ TeV using events containing two leptons", *JHEP* **02** (2019) 149.

[24] CMS and TOTEM Collaborations, "First search for exclusive diphoton production at high mass with intact protons in proton-proton collisions at $\sqrt{s} = 13$ TeV at the LHC", CMS Physics Analysis Summary CMS-PAS-EXO-18-014, TOTEM-NOTE-2020-003, Geneva: CERN, 2020.

[25] ATLAS Collaboration, "Observation of light-by-light scattering in ultraperipheral Pb+Pb collisions with the ATLAS detector", *Phys. Rev. Lett.* **123** (2019) 052001.

[26] CMS Collaboration, "Evidence for light-by-light scattering and searches for axion-like particles in ultraperipheral PbPb collisions at $\sqrt{s_{\mathrm{NN}}} = 5.02$ TeV", *Phys. Lett. B* **797** (2019) 134826.

[27] ATLAS Collaboration, "Evidence for light-by-light scattering in heavy-ion collisions with the ATLAS detector at the LHC", *Nature Phys.* **13** (2017) 852–858.

[28] D. d'Enterria and G. G. da Silveira, "Observing light-by-light scattering at the Large Hadron Collider", *Phys. Rev. Lett.* **111** (2013) 080405, erratum: *Phys. Rev. Lett.* 116 (2016) 129901.

[29] E. Chapon, C. Royon, and O. Kepka, "Anomalous quartic WW$\gamma\gamma$, ZZ$\gamma\gamma$, and trilinear WWγ couplings in two-photon processes at high luminosity at the LHC", *Phys. Rev. D* **81** (2010) 074003.

[30] I. Sahin and S. C. Inan, "Probe of unparticles at the LHC in exclusive two lepton and two photon production via photon-photon fusion", *JHEP* **09** (2009) 069.

[31] R. S. Gupta, "Probing quartic neutral gauge boson couplings using diffractive photon fusion at the LHC", *Phys. Rev. D* **85** (2012) 014006.

[32] L. N. Epele et al., "Looking for magnetic monopoles at LHC with diphoton events", *Eur. Phys. J. Plus* **127** (2012) 60.

[33] S. Fichet et al., "Probing new physics in diphoton production with proton tagging at the Large Hadron Collider", *Phys. Rev. D* **89** (2014) 114004.

[34] H. Sun, "Large extra dimension effects through light-by-light scattering at the CERN LHC", *Eur. Phys. J. C* **74** (2014) 2977.

[35] S. Fichet, "Shining light on polarizable dark particles", *JHEP* **04** (2017) 088.

[36] CMS and TOTEM Collaborations, "A search for new physics in central exclusive production using the missing mass technique with the CMS-TOTEM precision proton spectrometer", CMS Physics Analysis Summary CMS-PAS-EXO-19-009, TOTEM-NOTE-2022-003, Geneva: CERN, 2022.

[37] M. Boonekamp et al., "FPMC: A Generator for forward physics", *arXiv:1102.2531* (2011).

[38] CMS Collaboration, "Evidence for exclusive $\gamma\gamma \to \mathrm{W}^+\mathrm{W}^-$ production and constraints on anomalous quartic gauge couplings in pp collisions at $\sqrt{s} = 7$ and 8 TeV. ", *JHEP* **08** (2016) 119.

[39] ATLAS Collaboration, "Measurement of exclusive $\gamma\gamma \to W^+W^-$ production and search for exclusive Higgs boson production in pp collisions at $\sqrt{s} = 8$ TeV using the ATLAS detector.", *Phys. Rev. D* **94** (2016) 032011.

[40] ATLAS Collaboration, "Observation of photon-induced W^+W^- production in pp collisions at $\sqrt{s} = 13$ TeV using the ATLAS detector", *Phys. Lett. B* **816** (2020) 136190.

[41] D. R. Green, P. Meade, and M.-A. Pleier, "Multiboson interactions at the LHC", *Rev. Mod. Phys.* **89** (2017) 035008.

[42] E. Chapon, C. Royon, and O. Kepka, "Anomalous quartic $WW\gamma\gamma$, $ZZ\gamma\gamma$, and trilinear $WW\gamma$ couplings in two-photon processes at high luminosity at the LHC", *Phys. Rev. D* **81** (2010) 074003.

[43] G. Belanger and F. Boudjema, "Probing quartic couplings of weak bosons through three vectors production at a 500-GeV NLC", *Phys. Lett. B* **288** (1992) 201–209.

[44] CMS Collaboration, "Measurements of production cross sections of WZ and same-sign WW boson pairs in association with two jets in proton-proton collisions at $\sqrt{s} = 13$ TeV", *Phys. Lett. B* **809** (2020) 135710.

[45] CMS Collaboration, "Measurement of the electroweak production of $\mathrm{Z}\gamma$ and two jets in proton-proton collisions at $\sqrt{s} = 13$ TeV and constraints on anomalous quartic gauge couplings", *Phys. Rev. D* **104** (2021) 072001.

[46] CMS Collaboration, "Observation of electroweak production of $\mathrm{W}\gamma$ with two jets in proton-proton collisions at $\sqrt{s} = 13$ TeV", *Phys. Lett. B* **811** (2020) 135988.

[47] CMS Collaboration, "Measurement of vector boson scattering and constraints on anomalous quartic couplings from events with four leptons and two jets in proton-proton collisions at sqrt(s) = 13 TeV. Measurement of vector boson scattering and constraints on anomalous quartic couplings from events with four leptons and two jets in proton-proton collisions at sqrt(s) = 13 TeV", *Phys. Lett. B* **774** (2017) 682–705.

[48] CMS Collaboration, "Measurements of the pp $\to$ $W^{\pm}\gamma\gamma$ and pp $\to$ $Z\gamma\gamma$ cross sections at $\sqrt{s} = 13$ TeV and limits on anomalous quartic gauge couplings", *JHEP* **2110** (2021) 174.

[49] R. L. Delgado et al., "One-loop $\gamma\gamma \to W_L^+ W_L^-$ and $\gamma\gamma \to Z_L Z_L$ from the Electroweak Chiral Lagrangian with a light Higgs-like scalar", *JHEP* **07** (2014) 149.

[50] S. Fichet and G. von Gersdorff, "Anomalous gauge couplings from composite Higgs and warped extra dimensions", *JHEP* **03** (2014) 102.

[51] M. Maniatis, A. von Manteuffel, and O. Nachtmann, "Anomalous couplings in $\gamma\gamma \to W^+W^-$ at LHC and ILC", *Nucl. Phys. Proc. Suppl.* **179-180** (2008) 104–108, Proceedings of the PHOTON-LHC 2008 workshop.

[52] "Search for anomalous triple gauge couplings in WW and WZ production in lepton + jet events in proton-proton collisions at $\sqrt{s} = 13$ TeV", *JHEP* **12** (2019) 062.

[53] OPAL Collaboration, "Constraints on anomalous quartic gauge boson couplings from $\nu\overline{\nu}\gamma\gamma$ and $q\overline{q}\gamma\gamma$ events at CERN LEP2", *Phys. Rev. D* **70** (2004) 032005.

[54] D0 Collaboration, "Search for anomalous quartic $WW\gamma\gamma$ couplings in dielectron and missing energy final states in $p\overline{p}$ collisions at $\sqrt{s}$=1.96 TeV", *Phys. Rev. D* **88** (2013) 012005.

[55] S. Goy López and CMS Collaboration, "CMS Detector Performance during LHC Run 1 and projections for Run 2", *Nucl. Part. Phys. Proc.* **273-275** (2016) 1048–1054, Proceeding of the ICHEP2014 conference.

[56] M. Ressegotti and CMS Collaboration, "Overview of the CMS detector performance at LHC Run 2", *Universe* **5** (2019) 18, Proceeding of the ICNFP2018 conference.

[57] CMS Collaboration, "The CMS Experiment at the CERN LHC", *JINST* **3** (2008) S08004.

[58] CMS Collaboration, "The CMS tracker system project: Technical Design Report", Technical Design Report CERN-LHCC-98-006, CMS-TDR-5, CERN, 1997.

[59] A. Saha and CMS Collaboration, "Phase 1 upgrade of the CMS pixel detector", *JINST* **12** (2017) C02033, Proceeding of the IPRD16 conference.

[60] CMS Collaboration, "The CMS electromagnetic calorimeter project: Technical Design Report", Technical Design Report CERN-LHCC-97-033, CMS-TDR-4, Geneva: CERN, 1997.

[61] CMS Collaboration, "CMS: The hadron calorimeter technical design report", Technical Design Report CERN-LHCC-97-031, CMS-TDR-2, CERN, 1997.

[62] CMS Collaboration, "The CMS muon project: Technical Design Report", Technical Design Report CERN-LHCC-97-032, CMS-TDR-3, Geneva: CERN, 1997.

[63] CMS Collaboration, "CMS Technical Design Report for the Level-1 Trigger Upgrade", Technical Design Report CERN-LHCC-2013-011, CMS-TDR-12, CERN, 2013.

[64] CMS Collaboration, "Search for Resonant Production of High-Mass Photon Pairs in Proton-Proton Collisions at $\sqrt{s} = 8$ and 13 TeV", *Phys. Rev. Lett.* **117** (2016) 051802.

[65] ATLAS Collaboration, "Search for resonances in diphoton events at $\sqrt{s} = 13$ TeV with the ATLAS detector", *JHEP* **09** (2016) 001.

[66] H. F.-W. Sadrozinski, A. Seiden, and N. Cartiglia, "4D tracking with ultra-fast silicon detectors", *Rep. Prog. Phys.* **81** (2017) 026101.

[67] E. Bossini and CMS and TOTEM Collaborations, "The CMS Precision Proton Spectrometer timing system: performance in Run 2, future upgrades and sensor radiation hardness studies", *JINST* **15** (2020) C05054, Proceedings of the IPRD19 conference.

[68] G. Kramberger et al., "Effective trapping time of electrons and holes in different silicon materials irradiated with neutrons, protons and pions", *Nucl. Instrum. Meth. A* **481** (2002) 297–305.

[69] M. Moll, "Radiation damage in silicon particle detectors: Microscopic defects and macroscopic properties", PhD Thesis, 1999.

[70] G. Lindström, M. Moll, and E. Fretwurst, "Radiation hardness of silicon detectors – a challenge from high-energy physics", *Nucl. Instrum. Meth. A* **426** (1999) 1–15.

[71] C. Da Via and S. Watts, "The geometrical dependence of radiation hardness in planar and 3D silicon detectors", *Nucl. Instrum. Meth. A* **603** (2009) 319–324.

[72] S. Parker, C. Kenney, and J. Segal, "3D — A proposed new architecture for solid-state radiation detectors", *Nuclear Instruments and Methods in Physics Research Section A: Accelerators, Spectrometers, Detectors and Associated Equipment* **395** (1997) 328–343, Proceeding of the PIXEL1996 workshop.

[73] A. A. Ayón, R. L. Bayt, and K. S. Breuer, "Deep reactive ion etching: a promising technology for micro- and nanosatellites", *Smart Materials and Structures* **10** (2001) 1135–1144.

[74] The ATLAS IBL Collaboration, "Prototype ATLAS IBL modules using the FE-I4A front-end readout chip", *JINST* **7** (2012) P11010–P11010.

[75] G.-F. Dalla Betta et al., "Development of active and slim edge terminations for 3D and planar detectors", *2011 IEEE Nuclear Science Symposium Conference Record* (2011) 1334–1340.

[76] F. Ravera, "The CT-PPS tracking system with 3D pixel detectors", *JINST* **11** (2016) C11027, Proceeding of the PIXEL2016 workshop.

[77] F. Ravera, "3D silicon pixel detectors for the CT-PPS tracking system", PhD Thesis, Università degli Studi di Torino Scuola di Dottorato in Scienza ed Alta Tecnologia, 2016.

[78] G. Pellegrini et al., "First double-sided 3-D detectors fabricated at CNM-IMB", *Nucl. Instrum. Meth. A* **592** (2008) 38–43.

[79] G.-F. Dalla Betta et al., "Small pitch 3D devices", *PoS* **287** (2017) 028, Proceeding of the Vertex2016 conference.

[80] C. Da Via et al., "3D active edge silicon sensors with different electrode configurations: Radiation hardness and noise performance", *Nucl. Instrum. Meth. A* **604** (2009) 505–511.

[81] H. C. Kästli, "Frontend electronics development for the CMS pixel detector upgrade", *Nucl. Instrum. Meth. A* **731** (2013) 88–91, Proceeding of the PIXEL2012 workshop.

[82] H. C. Kästli et al., "Design and performance of the CMS pixel detector readout chip", *Nucl. Instrum. Meth. A* **565** (2006) 188–194, Proceeding of the PIXEL2005 workshop.

[83] A. Dominguez et al., "CMS technical design report for the pixel detector upgrade", Technical Design Report CERN-LHCC-2012-016, CMS-TDR-11, CERN, 2012.

[84] F. Meier, "PSI46dig pixel chip External Specification Manual", 2013.

[85] C. L. Phillips, "High Density Interconnect for the CMS Phase 1 Pixel Upgrade: Electrical Test and Visual Inspection", Students Note CERN-STUDENTS-Note-2015-136, CERN, 2015.

[86] E. Bartz, "Token Bit Manager 08C Chip Documentation", Manual, 2015.

[87] CMS Tracker Collaboration, "CMS Tracker control link specification. Part 2: front-end digital opto Hybrid", CMS Technical Report CMS-TK-ES-0019, CERN, 2002.

[88] C. Paillard, C. Ljuslin, and A. Marchioro, "The CCU25: a network oriented communication and control unit integrated circuit in a 0.25 μm CMOS technology", *CERN Yellow Reports: Conference Proceedings* (2002) 174–178, Proceeding of the 8th Workshop on Electronics for LHC Experiments.

[89] E. Hazen et al., "The AMC13XG: a new generation clock/timing/DAQ module for CMS MicroTCA", *JINST* **8** (2013) C12036.

[90] M. Pesaresi et al., *JINST* **10** (2015) C03036, Proceeding of the TWEPP2014 workshop.

[91] W. Adam et al., "The DAQ and control system for the CMS Phase-1 pixel detector upgrade", *JINST* **14** (2019) P10017.

[92] S. Fartoukh, "Experience with the ATS optics", *Proceedings of the 7th Evian Workshop on LHC beam operation* (2017) 93–104.

[93] TOTEM Collaboration, "LHC Optics Measurement with Proton Tracks Detected by the Roman Pots of the TOTEM Experiment", *New J. Phys.* **16** (2014) 103041.

[94] F. J. Nemes, "Elastic scattering of protons at the TOTEM experiment at the LHC", PhD Thesis, 2015.

[95] TOTEM Collaboration, "Evidence for non-exponential elastic proton–proton differential cross-section at low $|t|$ and $\sqrt{s}$=8 TeV by TOTEM", *Nucl. Phys. B* **899** (2015) 527.

[96] CMS and TOTEM Collaborations, "Efficiency of Si-strips sensors used in Precision Proton Spectrometer", CMS Detector Performance Summary CERN-CMS-DP-2018-056, CERN, 2018.

[97] CMS and TOTEM Collaborations, "Efficiency of the Si-strips sensors used in the Precision Proton Spectrometer: radiation damage", CMS Detector Performance Summary CERN-CMS-DP-2019-035, CERN, 2019.

[98] TOTEM Collaboration, "Total cross-section, elastic scattering and diffraction dissociation at the Large Hadron Collider at CERN: TOTEM Technical Design Report", Technical Design Report CERN-LHCC-2004-002, TOTEM-TDR-001, Geneva: CERN, 2004.

[99] H. Niewiadomski, "Reconstruction of protons in the TOTEM roman pot detectors at the LHC", PhD Thesis, Manchester University, 2008.

[100] C. J. Clopper and E. S. Pearson, "The use of confidence or fiducial limits illustrated in the case of the binomial", *Biometrika* **26** (1934) 404.

[101] G.-F. Dalla Betta et al., "The INFN–FBK "Phase-2" R&D program", *Nucl. Instrum. Meth. A* **824** (2016) 388–391, Proceeding of the FDFP 2015 conference.

[102] A. Starodumov, P. Berger, and M. Meinhard, "High rate capability and radiation tolerance of the PROC600 readout chip for the CMS pixel detector", *JINST* **12** (2017) C01078, Proceeding of the PIXEL2016 workshop.

[103] CMS Tracker Group of the CMS Collaboration, "The CMS Phase-1 pixel detector upgrade", *JINST* **16** (2021) P02027.

[104] E. Bartz, "Token Bit Manager 10d Chip Documentation", Manual, 2018.

[105] Zaber, "LAC10A-T4A Datasheet", Manual.

[106] Bourns, "3048 Linear Motion Potentiometer", Manual.

[107] Zaber, "X-MCC2 Datasheet", Manual.

[108] R. P. Foundation, "Raspberry Pi 3 Model B+", Manual.

[109] R. G. Aparicio, D. Gomez, and I. Coterillo Coz, "DataBase on demand", *J. Phys.: Conf. Ser.* **396** (2012) 052034, Proceeding of the CHEP2012 conference.

[110] Zaber, "Zaber Bridge Documentation", Software documentation.

[111] A. Lossent, A. R. Peon, and A. Wagner, "PaaS for web applications with OpenShift Origin", *J. Phys.: Conf. Ser.* **898** (2017) 082037, Proceeding of the CHEP2016 conference.

[112] Zaber, "Zaber Motion Library Documentation", Software documentation.

[113] GNR, "GNR-Ital Structures website", Website.

[114] Jenkins, "Jenkins Documentation", Software documentation.

[115] D. Thain, T. Tannenbaum, and M. Livny, "Distributed computing in practice: the Condor experience.", *Concurr. Comp. Pract. Exp.* **17** (2005) 323–356.

[116] D. Spiga et al., "The CMS Remote Analysis Builder (CRAB)", *Lect. Notes Comput. Sci.* **4873** (2007) 580–586, Proceeding of the HiPC2007 conference.

[117] C. Baldenegro et al., "Central exclusive production of W boson pairs in pp collisions at the LHC in hadronic and semi-leptonic final states", *JHEP* **12** (2020) 165.

[118] CMS Collaboration, "Precision luminosity measurement in proton-proton collisions at $\sqrt{s} = 13$ TeV in 2015 and 2016 at CMS", *Eur. Phys. J. C* **81** (2021) 800.

[119] CMS Collaboration, "CMS luminosity measurement for the 2017 data-taking period at $\sqrt{s} = 13$ TeV", Geneva: CERN, 2018.

[120] CMS Collaboration, "CMS luminosity measurement for the 2018 data-taking period at $\sqrt{s} = 13$ TeV", Geneva: CERN, 2019.

[121] T. Sjöstrand et al., "An Introduction to PYTHIA 8.2", *Comput. Phys. Commun.* **191** (2015) 159–177.

[122] V. Khachatryan et al., "Event generator tunes obtained from underlying event and multiparton scattering measurements", *Eur. Phys. J. C* **76** (2016) 155.

[123] CMS Collaboration, "Extraction and validation of a new set of CMS PYTHIA8 tunes from underlying-event measurements", *The European Physical Journal C* **80** (2019).

[124] J. Alwall et al., "The automated computation of tree-level and next-to-leading order differential cross sections, and their matching to parton shower simulations", *JHEP* **2014** (2014).

[125] S. Alioli et al., "Jet pair production in POWHEG", *JHEP* **04** (2011) 081.

[126] S. Frixione, P. Nason, and C. Oleari, "Matching NLO QCD computations with Parton Shower simulations: the POWHEG method", *JHEP* **11** (2007) 070.

[127] P. Nason, "A New method for combining NLO QCD with shower Monte Carlo algorithms", *JHEP* **11** (2004) 040.

[128] S. Agostinelli et al., "GEANT4–a simulation toolkit", *Nucl. Instrum. Meth. A* **506** (2003) 250–303.

[129] CMS Collaboration, "A multi-dimensional search for new heavy resonances decaying to boosted WW, WZ, or ZZ boson pairs in the dijet final state at 13 TeV", *Eur. Phys. J. C* **80** (2020) 237.

[130] M. Cacciari, G. P. Salam, and G. Soyez, "The anti-k_t jet clustering algorithm", *JHEP* **04** (2008) 063.

[131] M. Cacciari, G. P. Salam, and G. Soyez, "FastJet user manual", *Eur. Phys. J. C* **72** (2012) 1896.

[132] CMS Collaboration, "Pileup Removal Algorithms", Geneva: CERN, 2014.

[133] CMS Collaboration, "Jet energy scale and resolution in the CMS experiment in pp collisions at 8 TeV", *JINST* **12** (2017) P02014.

[134] J. Thaler and K. Van Tilburg, "Identifying Boosted Objects with N-subjettiness", *JHEP* **03** (2011) 015.

[135] J. Dolen et al., "Thinking outside the ROCs: Designing Decorrelated Taggers (DDT) for jet substructure", *JHEP* **05** (2016) 156.

[136] L. Harland-Lang, V. Khoze, and M. G. Ryskin, "Elastic photon-initiated production at the LHC: the role of hadron-hadron interactions", *SciPost Physics* **11** (2021).

[137] M. Aaboud et al., "Measurement of exclusive $\gamma\gamma \to W^+W^-$ production and search for exclusive Higgs boson production in pp collisions at $\sqrt{s} = 8$ TeV using the ATLAS detector", *Phys. Rev. D* **94** (2016) 032011.

[138] CMS Collaboration, "Evidence for exclusive $\gamma\gamma \to W^+W^-$ production and constraints on anomalous quartic gauge couplings in pp collisions at $\sqrt{s} = 7$ and 8 TeV", *JHEP* **08** (2016) 119.

[139] O. J. P. Éboli and M. C. Gonzalez-Garcia, "Classifying the bosonic quartic couplings", *Phys. Rev. D* **93** (2016) 093013.

[140] G. Belanger et al., "Bosonic quartic couplings at LEP-2", *Eur. Phys. J. C* **13** (2000) 283–293.

[141] S. Chatrchyan et al., "Search for $WW\gamma$ and $WZ\gamma$ production and constraints on anomalous quartic gauge couplings in pp collisions at $\sqrt{s} = 8$ TeV", *Phys. Rev. D* **90** (2014) 032008.

[142] CMS Collaboration, "Measurement of the electroweak production of Zγ and two jets in proton-proton collisions at $\sqrt{s} = 13$ TeV and constraints on anomalous quartic gauge couplings", *Phys. Rev. D* **104** (2021) 072001.